Electrochemical Studies of Water Splitting in Organic Media

THÈSE Nᴼ 7252 (2016)

ÉCOLE POLYTECHNIQUE FÉDÉRALE DE LAUSANNE

POUR L'OBTENTION DU GRADE DE DOCTEUR ÈS SCIENCES

PAR

Jonnathan Cesar HIDALGO ACOSTA

acceptée sur proposition du jury:

Prof. L. Helm, président du jury
Prof. H. Girault, directeur de thèse
Prof. A. Bond, rapporteur
Prof. D. Fermin, rapporteur
Prof. R. Buonsanti, rapporteuse

EPFL

ÉCOLE POLYTECHNIQUE
FÉDÉRALE DE LAUSANNE

Suisse
2016

A mi mamá

Acknowledgments

First of all, I would like to thank Professor Girault not only for the opportunity to join his group but also for his guidance, encouragement and constant support. I also thank him for providing an always-friendly working environment and for making of LEPA a second family.

Second, I would like to acknowledge to Professor Alan Bond, Professor David Fermín and Professor Raffaella Buonsanti for accepting to be part of the jury committee of my dissertation and for all the valuable comments and remarks. I also thank Professor Lothar Helm for being the president of the Jury.

I would like to express my gratitude to my main collaborators in LEPA (second bosses): Manuel Méndez, Micheál Scanlon and Astrid Olaya. They have greatly contributed not only to these pages but also to my formation as a scientist.

This work would have not been possible without the collaboration of many other people: Milica Jovic, Andreas Lesch, Véronique Amstutz, Heron Vrubel, Pekka Peljo. Natalia Gasilova. I also thank to Christopher Dennison, for reading the first draft of this thesis and to Patrick Voyame for the translation of the abstract into French.

I am very grateful to all my other colleagues and friends in LEPA: Alberto Battistel, Xiaojun Bian, Alejandro Colli, Alina Sekretaryova, Peiyu Ge, Tzu-En Lin, Desire Abro, Sunny Maye, Victor Costa, Haiqiang Deng, Fangting Zhang, Xiaoqin Zhong, Yingdi Zhu, Shiwei Zhou, Gérladine Stauffer, Ping-Ping Fang, Yu Lu, Tong Wu, Lucie Rivier, Olga Melchaeva, Elena Zanzola, Elena Vladimirovna, Hualan, Kathryn Toghill, Jane Stockmann, Liang Qiao, Mikaël Frossard, Frédéric Gumy, Grégoire Gschwend, Dmitry Momotenko, Alexandra Bondarenko, Evgeny Smirnov and Elena Tobolkina.

Many thanks to the Colombian community in LEPA: Manuel Méndez, Astrid Olaya and Andres Molina. A big thanks to Fernando Cortés, who took the risk to recommend me to Hubert and also for his invaluable friendship.

I have to thank to all those people who do not appear in the publications but are essential parts of the LEPA and in general the EPFL machinery. I am indebted to Patricia Byron and Anne Lene Odegaard, for making our lives easier, taking care of all the administrative affairs. I also have to thank Patricia for her kindness, extraordinary sense of humor, and also for picking me up in the train station when I first arrived to Lausanne. I also appreciate the kind support given by the technical staff from the ISIC in Lausanne and Sion: André Fattet, Christophe Clément, Stéphane Voeffray, Robin Délèze, Yoann Dind, Cédric Passerini, Jacques Gremaud, Laurent Seydoux, Annabelle Coquoz and others.

I want to specially thank to all my friends from the other side of the "pond" for listening when I need them the most, and also for all the great time we have spent together: Dorian Acevedo, Alirio Mendoza, Juan Camilo Aguacía, Paola Gonzales, Yinna Hernandez, Daniel Aguilera, William Chamorro, Luis Sandoval, Vida de la Paz, Olga Angarita, Amira Garnica and others.

I convey special acknowledgment to Małgorzata (I still have problems to pronounce her last name) for her love, patience and constant support. I am completely aware how difficult and challenging can be dealing with a person like me. I also thank to her father for always treating me as part of his family and for his "special" sense of humor.

Por último, mis mas sinceros agradecimientos a mi familia: mis padres, tío, hermanos y sobrinas. Todo mi amor y gratitud está con ellos. Asimismo, me llena de orgullo y satisfacción poder dedicar este trabajo (mucho o poco) a mi mamá. Su fortaleza, amor y entrega incondicional nos ha permitido a mí y a mis hermanos alcanzar gran parte de las metas que nos hemos propuesto. Este doctorado no es solo mío sino también de ella.

Abstract

The development of new routes towards the generation of environmentally friendly solar fuels, such as molecular hydrogen (H_2) for use in fuel cells, is a grand challenge facing the scientific community. Water splitting, viewed as the sum of the hydrogen evolution reaction (HER) and water oxidation reaction (WOR), represents one of the most promising, yet challenging, options in this regard.

In nature, water splitting occurs under primarily non-aqueous conditions, as the oxygen-evolving complex of Photosystem (II) and the Ferrodoxin-NADP$^+$ reductase enzyme are embedded in the lipid environment of thylakoid membranes. This provides a blue print for the development of efficient systems for WOR and HER, profiting from the changes structure-reactivity in those complex environments. Herein, we investigate the two processes involved in the overall water splitting, WOR and HER, ocurring in mainly non-aqueous environment (*i.e.,* water/acetonitrile mitures). Another aspect addressed in this work, is the inmobilization of catalitycally active nanoparticles towards WOR, at the surface of an electrode.

In first instance, a layer-by-layer methodology was used to prepare thin films consisting of bilayers of negatively charged citrate-stabilized IrO_x nanoparticles (NPs) and the positively charged poly(diallyldimethylammonium chloride) (PDDA) polymer. The IrO_x films obtained were amorphous, with the NPs therein being well dispersed and retaining their as-synthesized shape and sizes. UV/vis spectroscopic and spectro-electrochemical studies confirmed that the total surface coverage and electrochemically addressable surface coverage of IrO_x NPs increased linearly with the number of bilayers up to 10 bilayers. Moreover, the use of stabilized particles allowed us to obtain an electrochemical response, which resembles the highly reversible waves observed in hydrous iridium oxide films (HIROFs).

Taking one step further, the concept of layer-by-layer inkjet printing was implemented for the fabrication of pH sensing electrodes based on IrO_x. Those electrodes exhibited good performance, with a linear and near-Nernstian pH response of 58 - 59 mV/pH, close to the theoretical sensitivity (59 mV/pH).

Water oxidation catalyzed by iridium oxide nanoparticles (IrO_x NPs) in water/acetonitrile mixtures using $[Ru^{III}(bpy)_3]^{3+}$ as oxidant was studied as a function of the water content, the acidity of the reaction media and the catalyst concentration. It was observed that under acidic conditions ($HClO_4$) and at high water contents (80 % (v/v)) the reaction is slow, but its rate increases as the water content decreases, reaching a maximum at approximately equimolar proportions ($\approx$ 25 % H_2O (v/v)). The results were rationalized based on the structure of water in water/acetonitrile mixtures. At high water fractions, water is present in highly hydrogen-bonded arrangements and is less reactive. As the water content decreases, water-clustering gives rise to the formation of water-rich micro-domains, which are considerably more reactive towards oxygen production.

Further analysis *via* electrochemical measurements at PDDA-IrO_X modified electrodes, demonstrated that those changes in reactivity are correlated with decrease in the overpotential for WOR. Based on a straightforward thermodynamic analysis, those changes in reactivity were associated with favourable kinetics rather than a lowering in the thermodynamic barriers.

Finally, the light-driven HER catalyzed by Pt in acidified acetonitrile solutions and using tetrathiafulvalene (TTF) as both, sensitizer and electron donor, was studied. Kinetic studies indicated that the reaction starts by strong and fast adsorption of TTF-H^+ on the catalyst surface, followed by slow photoreduction of protons. On the other hand, the addition of water to the mixture of reaction leads to evolution of O_2 by water oxidation, inhibiting HER. In both cases, no decomposition of the electron donor/acceptor was observed, indicating that both reactions are reversible and therefore the donor/acceptor potentially recyclable.

Resumé

Le développement de nouvelles routes envers la génération de combustibles solaires respectueux de l'environnement, tel que l'hydrogène moléculaire (H_2) pour son utilisation dans les piles à combustibles, est un important défi pour la communauté scientifique. Le craquage de l'eau, consistant en la somme de la réaction d'évolution d'hydrogène (HER) et de la réaction d'oxydation de l'eau (WOR), représente l'une des options les plus prometteuse, mais difficile, dans ce domaine.

Dans la nature le craquage de l'eau se produit dans des conditions essentiellement non-aqueuses, avec comme exemple le Photosystème (II) dans lequel l'enzyme Ferrédoxine-NADP$^+$ réductase est intégrée à l'environnement lipidique des membranes des thylakoides. Ceci fournit les bases du développement de systèmes efficaces pour les réactions WOR et HER, en profitant des changements de structure-réactivité dans ces environnements complexes. Ici, nous étudions les deux processus impliqués dans le craquage de l'eau, WOR et HER, survenant principalement en environnement non-aqueux (*i.e.*, mélanges eau/acétonitrile). Un autre aspect abordé dans ce travail, est l'immobilisation de particules catalytiquement actives pour la WOR à la surface d'une électrode.

Dans un premier temps, une méthode de déposition couche par couche à été utilisée pour préparer des couches minces comprenant des doubles couches de nanoparticules (NPs) négativement chargées d'IrO_x stabilisées par du citrate et de polymère de chlorure de poly(diallyméthylammonium) (PDDA) positivement chargé. Les filmes de IrO_x obtenus étaient amorphes, les NPs y étant bien dispersées et conservaient leur forme et taille originelle. Des études spéctroscopiques UV/vis et spéctro-électrochimiques ont confirmé que la couverture de surface totale et la couverture de surface adressable par électrochimie des NPs de IrO_x augmentaient linéairement avec le nombre de doubles couches jusqu'à 10 doubles couches. De plus, l'utilisation de particules stabilisées nous a permis d'obtenir une réponse électrochimique qui ressemble aux vagues hautement réversibles obtenues dans des films d'oxyde d'iridium hydratés (HIROFs).

En allant plus loin, le concept d'impression couche par couche par jet d'encre a été implémenté pour la fabrication d'électrodes à pH basées sur l'IrO_x. Ces électrodes ont montré de bonnes performances, avec une réponse linéaire et une réponse au pH quasi-nernstienne de 58 – 59 mV/pH, proche de la sensibilité théorique (59 mV/pH).

L'oxydation de l'eau, catalysée par des nanoparticules d'oxyde d'iridium (IrO_x NPs) dans des mélanges eau/acétonitrile en utilisant $[Ru^{III}(bpy)_3]^{3+}$ comme oxydant, a été étudiée en fonction de la teneur en eau, de l'acidité du milieu réactionel et de la concentration de catalyseur. Il a été observé que sous des conditions acide ($HClO_4$) et à des teneurs élevée en eau (80 % (v/v)) la réaction est lente, mais la vitesse de la réaction augmente alors que la teneur en eau diminue, atteignant un maximum en proportions approximativement équimolaires ($\approx$ 25 % H_2O (v/v)). Les résultats ont été rationalisés par rapport à la structure de l'eau dans des mélanges eau/acétonitrile. A teneures élévées en eau, l'eau est présente en arrangements à fortes liaison hydrogène et est moins réactive. A mesure que la teneur en eau diminue, le regroupement des molécules d'eau donne lieu à la formation de micro-domaines riche en eau, qui sont nettement plus réactifs envers la production d'oxygène.

Une analyse plus poussée *via* des mesures électrochimiques sur des électrodes PDDA-IrO_x modifiées, a demontré que ces changements de réactivités sont corrélés avec la diminution de l'overpotentiel pour la WOR. Basé sur une analyse thermodynamique simple, ces changements de réactivité ont été associés à une cinétique favorable plutôt qu'à une diminution des barrières thermodynamiques.

Finalement, la HER assistée par la lumière et catalysée par Pt dans des solution d'acétonitrile acidifiées et en utilisant tetrathiafulvalène (TTF) à la fois comme sensibilisateur et donneur d'électrons a été étudiée. Les études cinétiques ont indiqué que la réaction commence par une adsorption forte et rapide de TTF-H^+ à la surface du catalyseur, suivie par une lente photoréduction de protons. D'un autre côté, l'addition d'eau au mélange réactionel conduit à la formation d'O_2 par oxydation de l'eau, inhibant la HER. Dans les deux cas, aucune décomposition du donneur/accépteur d'électrons n'a été observée, indiquant que les deux réactions sont réversibles, et donc le donneur/accepteur est potentiellement recyclable.

Mots-clés : Craquage de l'Eau, Oxydation de l'Eau, Évolution d'Hydrogène, Oxyde d'Iridium, Déposition Couche par Couche, Jet d'Encre, mélanges Eau/Acétonitrile, Tetrathiafulvalène.

Table of Contents

Chapter 1. Introduction

Chapter 2. Layer-by-Layer Deposition of Iridium Oxide on FTO

Chapter 3. Layer-by-Layer Inkjet Printing of IrOx-Based pH Sensors

Chapter 4. Catalysis of Water Oxidation in Acetonitrile by Iridium Oxide Nanoparticles

Chapter 5. Enhanced Reactivity of Water in Water/Acetonitrile Mixtures Studied by Cyclic Voltammetry

Chapter 6. Water Splitting by Tetrathiafulvalene

Chapter 1

Introduction

_____

1.1   Overview

Society's ever-increasing demand for energy has been primarily satisfied by the combustion of fossil fuels, causing deleterious effects of global warming due to the release of vast quantities of carbon dioxide (CO_2). Moreover, the advent of more aggressive extraction technologies (*e.g.,* horizontal drilling and hydraulic fracturing) have seen the appearance of new associated environmental risks, like the contamination of ground water and the leakage of powerful greenhouse gasses (*e.g.,* methane), at the same time that larger extensions of land are required. All of these factors make the development of a clean energy supply one of the main challenges facing our generation.

Triggered by the development of new technologies and the consequent decrease cost of the photovoltaic devices, the use of renewable energies, solar and wind power, has rapidly evolved during the last years. Nevertheless, both technologies suffer from the disadvantage of the intermittency, which limits their usage as primary feed for the grid, requiring the use of mediating systems to buffer their output. Several alternatives

for storage are proposed[1,2], hydroelectric, compressed air, thermal energy and batteries. Of course, the energy that can be stored in the chemical bonds of small molecules represent a very attractive approach. This has been well understood by nature, which during billions of years of evolution has developed the complex machinery of the photosynthesis, where the energy obtained from the sun is stored in the form of small molecules (*i.e.,* ATP, NADPH or H_2), to be subsequently used to convert CO_2 into carbohydrates. Inspired by this process, much effort is currently being devoted to the production of environmentally friendly solar fuels (such as molecular hydrogen (H_2)), *via* water splitting, ideally solely using sunlight as the energy source and water as the sacrificial electron donor. [3-7]

The water splitting reaction is best viewed as the sum of two half-reactions, the hydrogen evolution reaction (HER) (Eq. 1.1) and the water oxidation reaction (WOR) (Eq 1.2):

$$2H^+ + 2e^- \rightarrow H_2 \tag{1.1}$$

$$2H_2O \rightarrow 4H^+ + 4e^- + O_2 \tag{1.2}$$

In spite of the vast literature related to water splitting, the use of organic solvents as a media for WOR and HER is relatively new, with only few reports appearing in recent years. With this in mind, the main objective of the project described herein is the study of both processes occurring in acetonitrile media as an effective way to improve the kinetics of the WOR and HER. A second part (appearing before in the structure of the text) is devoted to the immobilization of catalyst for WOR.

In the following sections, the nature of the WOR and HER will be discussed as well as some of the main catalytic systems reported in literature. Specific examples of WOR in organic solvents will be directly presented in Chapter 4. A brief introduction to the work on HER by metallocenes will be presented in section 1.11. Finally, the layer-by-layer methodology and some selected examples for the immobilization of nanoparticles in multilayered films will be described in section 1.8.

1.2 Photosynthesis: The Model

Photosynthesis plays a major role in the history of earth. The first organisms capable of producing oxygen as waste during the metabolic processes were the oceanic cyanobacteria. The early oxygen produced by these microbes was captured by minerals *e.g.*, Fe, and readily-oxidizable organic matter. Then, once those oxygen sinks were exhausted, the concentrations of oxygen rose, causing the extinction of most of the anaerobic forms of life. This event, commonly refereed as the "great oxygenation event" or the "oxygen holocaust", was the responsible for the present constitution of earth's atmosphere and thereafter the life as we know it.

During photosynthesis, algae and plants use light to extract electrons from water, which is oxidized to dioxygen (O_2). Then, these electrons are used to produce reduced equivalents of NAPDH and ATP (under some specific condition some microorganisms such as cyanobacteria and microalgae are able to synthetize H_2 as well [8]), acting as fuel for various biological processes, including the reduction of carbon dioxide (CO_2) into proteins, lipids or carbohydrates.
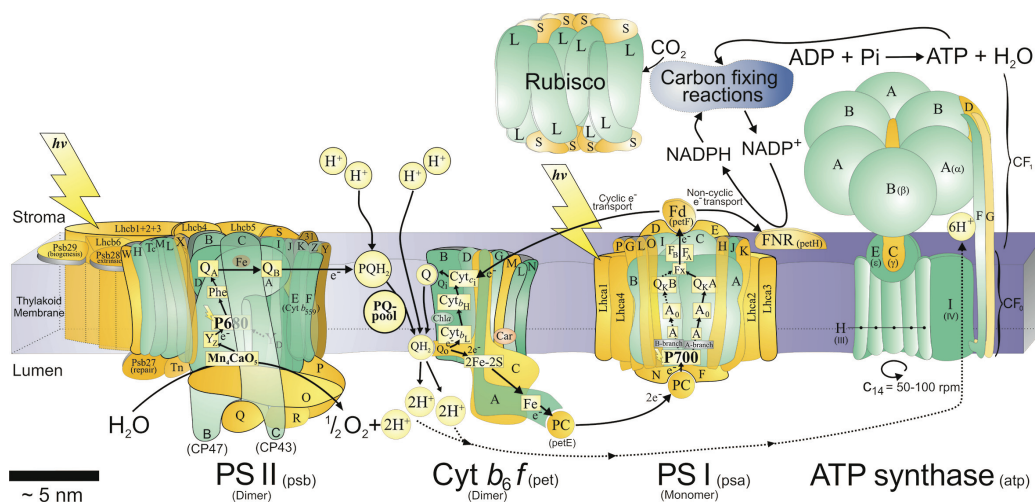

Figure 1.1 Major proteins and protein complexes of the chloroplast photosynthetic apparatus of a higher plant exemplified by Arabidopsis thaliana. The picture has been taken and adapted from reference [9].

The process can by divided in three different steps: (i) the harvesting of light in the so-called photosystems I and II (PSI and PSII) by an array of pigments denominated antenna system, (ii) proton-coupled electron transfer reactions between redox cofactors, allowing spatial charge separation, and (iii) catalysis of water oxidation and $NADP^+$ reduction at the oxygen evolving complex (OEC), and the ferredoxin-$NADP^+$ reductase enzyme (FNR). In addition, the overall process creates proton gradient across the chloroplast membrane, which is used by the ATP synthase in the synthesis of ATP.[9,10] Noteworthy, all those processes occur under mainly non-aqueous conditions as the Photosynthetic systems are embedded in membrane pigment−protein complexes and no bulk water present. Consequently, the pH as well as p*K* values are unknown.

The unmatched efficiency with which the overall photosynthetic process takes place, is determined by the balance of thermodynamics and kinetics of these three processes. In this regard, intensive studies have been focused on investigating the mechanisms involved in natural photosynthesis, especially those at OEC and FNR, providing the inspiration for the design of systems for water splitting.

A key breakthrough in the present understanding of the mechanism of the WOR at the OEC was reported by Kok *et al.,* working dark-adapted chloroplasts from spinach.[11] From their study, they concluded that water oxidation takes place through the formation of 5 intermediates designated as S_0-S_4, which upon illumination are sequentially oxidized in monoelectronic steps (known as the Kok cycle). Then, the generation of the S_4, the most oxidizing intermediate is followed by a rapid release of oxygen and the regeneration of S_0. All this process is facilitated by the ability of the OEC, an oxo-bridged structure with four Mn atoms and one Ca, to easily access to several oxidation states. The presence of a nanostructured protein environment also plays a role, providing the sites for the stabilization of the intermediates and a proton exit. Figure 1.2 shows schematically the different steps in the Kok cycle and the structure of the oxygen evolving complex.

The core of the oxygen evolving complex has been subjected to intense study mostly by X-ray diffraction, electronic paramagnetic resonance (EPR) and X-ray crystallography. Early results showed the presence of at least two di-μ-oxo bridges with a Mn-Mn distance of 2.7Å[12,13], followed by the finding of a mono-μ-oxo Mn−Mn

distance of 3.3 Å [14,15]. Further evidence led to the conclusion that a Calcium atom is present in the structure leading to the idea of the $CaMn_4O_4$ cluster.[16]

The most reliable structure of the native-dark S_1 complex with a resolution of 1.9 Å shows chair-like structural arrangement, where a distorted cubane Mn_3CaO_4 core is linked *via* oxo bridges to a fourth ''dangling'' Mn center[17] (Figure 1.2). Notably all those structural features of the OEC are preserved in essentially all species of photosynthetic organisms. This lack of natural diversity reflects the importance of this special configuration in order to carry out WOR at high efficiencies
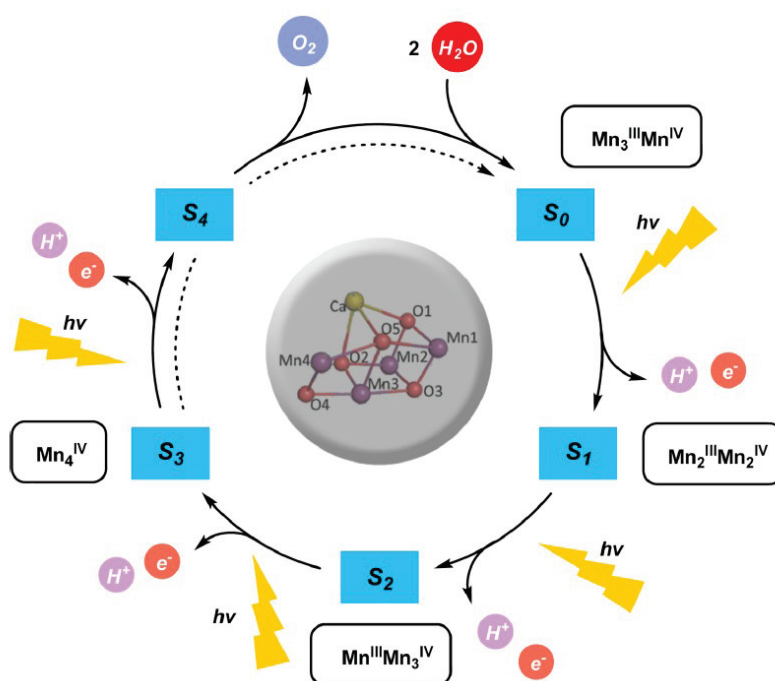
Figure 1.2 Kok Cycle in which the OEC Cycles through Five Redox States, S_0-S_4, via Consecutive Photo-oxidation. Take from ref [5].

Structural changes during the catalytic cycles in the OEC have been studied mainly by X-ray absorption fine structure (EXAFS) techniques using native samples of PSII and also Sr-substituted complexes. From those studies, several structures have been proposed based in the fluctuations of the Mn-Mn distances, which have been interpreted as changes in the oxidation states, protonation, coordination of species and geometry. Comprehensive reviews detailing the proposed structures for the intermediaries in the Kok cycle can be found in literature. [18-20]

1.3 Catalytic water oxidation reaction

As briefly outlined in section 1.1, WOR involves the transfer of 4 electrons and 4 protons with a thermodynamic potential of 1.23 V. The intrinsic large thermodynamic requirement jointly with the formation of high-energy intermediates (see table 1.1), makes this process both thermodynamically and kinetically restricted. Therefore, the use of a catalyst is required in order to stabilize the high-energy intermediates, offering paths of lower thermodynamic barriers and faster kinetics.

Table 1.1 Standard potential for several reactions associated to the oxidation of water.

Reaction	E^0 *vs. SHE* / V
Four-electron reactions	
$2H_2O \rightarrow 4H^+ + 4e^- + O_2$	1.229
$4OH^- \rightarrow O_2 + 2H_2O + 4e^-$	0.401
Two electron reactions	
$2H_2O \rightarrow H_2O_2 + 2H^+ + 2e^-$	1.776
$2OH^- \rightarrow H_2O_2 + 2e^-$	0.948
$H_2O_2 \rightarrow O_2 + 2H^+ + 2e^-$	0.682
$H_2O_2 + 2OH^- \rightarrow O_2 + 2H_2O + 2e^-$	-0.146
One-electron reactions	
$H_2O \rightarrow OH + H^+ + e^-$	2.848
$OH^- \rightarrow OH + e^-$	2.020
$H_2O_2 \rightarrow HO_2 + H^+ + e^-$	1.495
$H_2O_2 + OH^- \rightarrow HO_2 + H_2O + e^-$	0.667
$HO_2 \rightarrow O_2 + H^+ + e^-$	-0.130
$HO_2 + OH^- \rightarrow O_2 + H_2O + e^-$	-0.198

Typical water oxidation catalysts (WOCs) comprise a metallic center (*e.g.*, Ir, Ru, Mn), which is present either in organometallic complexes or oxides. In those catalysts, the interaction with water occurs *via* formation of coordinating bonds, where the multivalent center acts as a relay during the sequential proton and electron transfer reactions. The simultaneous transfer of electrons and protons (Proton Coupled Electron Transfer, PCET) is crucial as it prevents the charge buildup in the metal center, enabling the presence of multiple redox states in a narrow potential window, and therefore the possibility to access to high oxidation states in the metal[21].

Most of the mechanistic details about of the catalytic water oxidation come from the work on Ru molecular catalysts[22,23]. From those studies, two general catalytic paths have then been proposed: *(i)* water nucleophilic attack (WNA) and *(ii)* radical oxo coupling (ROC) (see Figure 1.3). For WNA, the mechanistic proposal postulates the formation of M=O followed by water nucleophile attack, leading to O-O bond formation. The high oxidation state of the metal makes the oxygen electrophilic enough to be attacked by a water molecule. A second pathway is the ROC: in this mechanism two metal oxyl species are required to couple together to form the O-O bond. This mechanism is usually associated with organometallic complexes comprising more than one metallic center or bulk metal oxides. Figure 1.3 depicts the formation of the critical O-O intermedate in the WNA and ROC mechanisms.
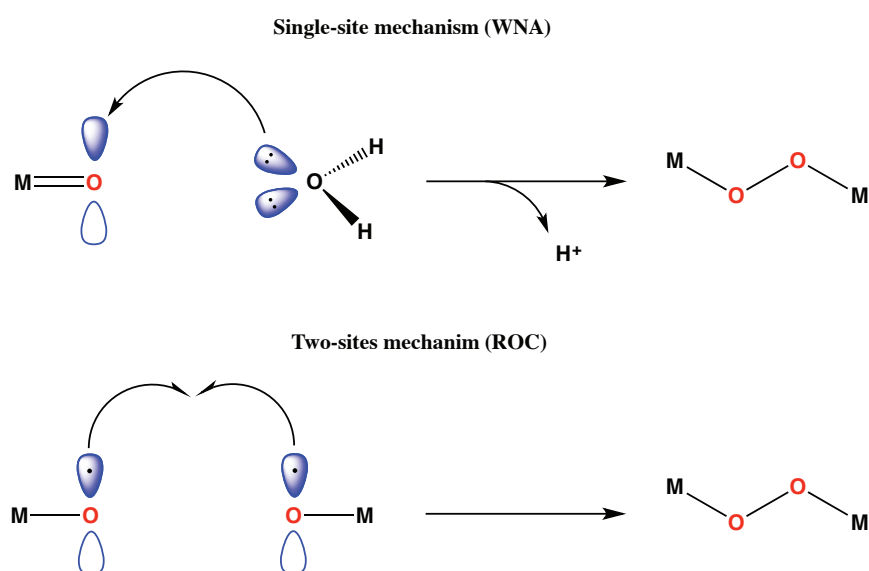
Figure 1.3 Schematics of the O-O formation in WNA and ROC mechanism.

In the following section, a brief review of three families of WOCs will be given. The catalysts will be separated according to the metal involved in the catalysis in: *(i)* Mn, due to its relevance as archetype of the OEC; *(ii)* Ru, due to its importance in the mechanistic understanding of WOR; and *(iii)* Ir, as being IrO$_x$ the catalysts used in the present thesis, and one of the most efficient for WOR. Systems based on other metals such as Fe and Co will not be discussed.

1.4   Water oxidation catalysts

1.4.1 Manganese-based WOCs

1.4.1.1   Manganese oxides

Inspired by the Mn$_4$Ca core of the OEC, much effort have been devoted to the synthesis of Mn-based catalyst for WOR. The rich redox chemistry, the abundance and the ultimate choice of nature for this element, make it attractive at fundamental and practical levels.

Anhydrous Mn$_x$O$_y$ solids exhibit poor or no catalytic activity for water oxidation, being necessary their use as highly hydrated solids as in colloids.[6] Shilov and coworkers demonstrated in 1968 that MnO$_2$ colloids catalyze the oxidation of water by typical oxidants like Ce(IV), Ru(bpy)$_3^{3+}$ and Fe(bpy)$_3^{3+}$.[24] Additionally, they showed that the incorporation of Mn into phospholipid membranes leads to higher catalytic activities.[25] The catalysts were prepared by ultrasonic dispersion of dipalmitoylphosphatidylcholine in the presence of MnCl$_2$. Then, the addition of an oxidant promotes the formation of Mn$_x$O$_y$ species which are catalytic for WOR.

One important drawback of the MnO$_2$ colloids is their propensity to aggregate. The flocculation of small particles upon cycling leads to a substantial decrease of the activity and necessitates the incorporation of stabilizers or the use of a support.[26] Jiao *et al.* reported an interesting approach consisting in the encapsulation of MnO$_x$ nanoparticles in mesoporous matrixes such as KIT-6 silica[27]. This procedure led to the

formation of manganese oxide aggregates along the silica channels with mean diameters in the 70-90 nm range.

Recently, Kurz *et al.* reported the synthesis of Mn compounds with higher activities than previously reported.[28] Interestingly, the incorporation of Ca during the synthesis results in a more efficient catalyst for WOR identified as Marokite ($CaMnO_4$). However, it is difficult to ascribe the enhanced kinetic to higher specific activity, due to the substantial changes in the morphology promoted by the incorporation of Ca during the synthesis.

1.4.1.2   Molecular Mn-based WOCs

In the OEC, the $CaMn_4$ cluster is kept together by the presence of several *µ*-oxo groups, and is further stabilized by neighboring carboxylate and imidazole functionalities. This additional stabilization allows the OEC to operate 10^6 times between the oxidation states in the Kok cycle, even at the harsh conditions needed for WOR. Following a bio-inspired approach, much of the work in molecular Mn catalysts has been focused in the construction of simplified systems containing features similar to those in OEC. These systems, often polymetallic, involve the use of ligands, mimicking the stabilizing effects provided by the protein environment in the OEC.

Oxygen evolution mediated by the terpyridine dimer of manganese $[(bpy)_2Mn^{III}(\mu\text{-}O)_2 Mn^{IV}(bpy)_2]^{3+}$ (terpy dimer, Figure 1.4), and using oxygen transferring oxidants *e.g.,* oxone, (HSO_5^-), hypochlorite($HClO^-$), was discovered by Crabtree and co-workers[29]. The initial step in the catalytic cycle is the binding of the oxidant to the Mn(III) centers in the Mn (III, IV) dimer[30]. The binding to Mn(IV, IV) is thought to be irrelevant for the overall   oxygen evolution as the formation of Mn(VI) from Mn(IV) is unlikely to happen under the experimental conditions. The release of SO^{4-} results in the formation of the intermediate responsible for the formation of the O-O bond. Despite the presence of large amounts of inactive Mn(IV, IV) and the consequent underestimation of specific activity, high turnover frequencies have been observed (0.67 s^{-1}) with this catalytic system. [31,32]
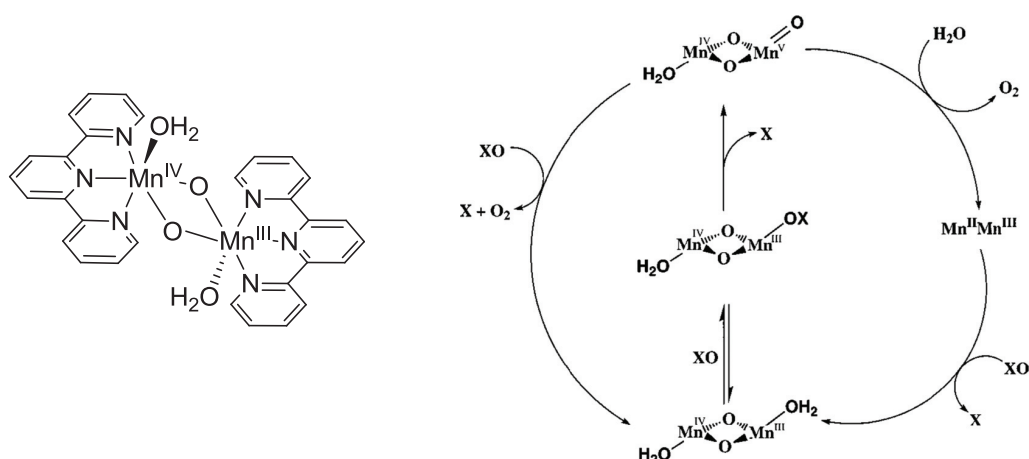
Figure 1.4 Left) Structure of the terpy dimer [Mn(terpy)-(H$_2$O)O]$_2$$^{3+}$. Right) Mechanism proposed by Crabtree *et al* for the reaction between the terpy dimer and a two-electron, oxo-donating reagents, XO. (Leftpathway) Attack of XO on the terminal oxo ligand gives rise to oxone−oxone coupling (no incorporation of oxygen atoms from oxidation of water). (Right pathway) Attack of solvent water on oxidant-deposited oxo ligand gives rise to water oxidation and consequent incorporation of atoms from substrate water into product dioxygen. Taken from the reference [33].

Mechanistic details about water oxidation catalyzed by the terpy dimer have been explored by using H$_2$^{18}O.[30,32] From those ^{18}O-labeling studies, it has been found that at moderate concentration of oxone, up to 50% of O in the O$_2$ comes from water molecules. However, at high oxone loadings, the oxone-oxone coupling becomes the main pathway, giving rise to molecular O$_2$ where the two atoms proceed from the oxidant. A detailed structure of the catalytic cycle is shown in the Figure 1.4 as well as the mechanism reported by Crabtree and coworkers.

Several difficulties have resulted when attempting WOR driven by one-electron oxidizers and mediated by terpy dimer and analogues. For instance, Ce(IV) a typical one electron oxidizer used in catalysis, is stable only in very acidic conditions where the dimer is protonated with the formation of the non-reactive "dimer of dimers"[34]. This tendency to aggregation has driven the use of heterogeneization strategies in order to keep the activity. Yagi and co-workers reported that the terpy dimer adsorbed on Kaolin, mica or montmorillonite K10 could mediate Ce(IV)-driven water oxidation with moderate TONs of up to 17 [35]. The Mn-dimer/mica catalyst was later successfully applied in a photochemical system containing [Ru(bpy)$_3$]$^{2+}$ and S$_2$O$_8$$^{2-}$ as sensitizer and sacrificial electron acceptor respectively[36]

10

1.4.2 Ruthenium-based WOCs

1.4.2.1   Ruthenium oxide

Colloidal ruthenium oxide has been reported since the 70s as an effective catalyst for WOR.[37] This catalyst can mediate WOR by typical one-electron oxidants like Ce(IV), and also in photosystems involving the use of $Ru(bpy)_3^{2+}$ and sacrificial electron acceptors.[38,39] Nevertheless, despite the high activity of RuO_2, it undergoes corrosion under typical operation conditions, leading to the formation of RuO_4 soluble-species with the consequent loss of activity[40]. This problem has been partially solved by the use of admixtures containing Ir[41]. The presence of Ir, even at relatively small percentages (20%) has shown to have a dramatic effect on the stability, reducing the corrosion to 4% of its value in pure RuO_2. This increase in stability, which is accompanied by a decrease in reactivity, was initially attributed to electronic effects[41]. However, recent evidence has pointed to stabilization governed by the protection of the buried, less-noble Ru atoms by the Ir skeleton.[42]

Recently, Markovic *et al* reported a novel strategy based on tuning the surface composition of bimetallic $Ir_{0.5}Ru_{0.5}$ large solids and nanoparticles.[42] The annealing (Ar/H_2) of as-prepared alloys promotes the enrichment of the surface by Ir. Thus, upon chemical or electrochemical oxidation, the Ru centers are quickly dissolved leaving behind a stable Ir skeleton. The catalysts obtained under those conditions were found to be four times more stable, but equally active as commercial IrRu catalysts used in PEM.

1.4.2.2   Molecular Ru-based WOCs

Since Meyer *et al*. reported the first molecular WOC, the dinuclear oxo-bridged ruthenium complex $[(bpy)_2(H_2O)Ru^{III}(\mu\text{-}O)Ru^{III}(H_2O)(bpy)_2]^{4+}$ (Figure 1.5)[43], several new families of Ru-based WOCs have been designed and reported[44-46]. This compound also called the "blue dimer" was a major breakthrough as the catalyst surpassed the poor performance of synthetic Mn-based catalysts known at that time. Additionally, this complex represented the first proof-of-concept that binuclear molecular compounds could store two electrons and two protons per metal center to achieve four electron/four proton reduction. The catalysis in the blue dimer proceeds by several PCET steps, avoiding the charge buildup and reaching the high oxidation

state $([(bpy)_2(O)Ru^V(\mu\text{-}O)Ru^V(O)(bpy)_2]^{4+}$.[22,33,47] Then, this intermediate undergoes rapid O transfer *via* WNA mechanisms (section 1.3). Finally, the peroxido species formed are oxidized intramolecularly by the second $Ru^V=O$ group, thus releasing O_2. The structure of the blue dimer and the last mechanistic proposal are shown in the Figure 1.5
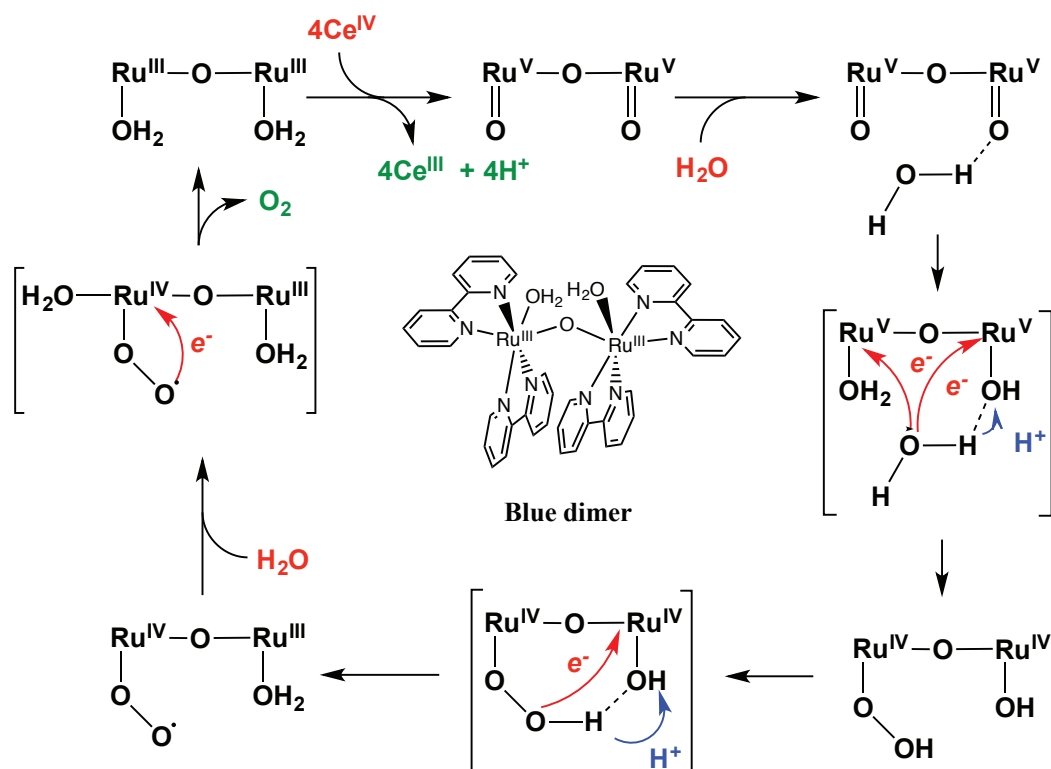
Figure 1.5 Mechanism for WOR mediated by the blue dimer. Adapted from the reference [22].

Despite the great importance of the blue dimer as a model, its practical application as a catalyst for WOR has been limited due to progressive loss of activity. The coordination of supposedly innocent anions (anation) leads to a progressive deactivation by preventing the formation of the crucial intermediate Ru^V-O-Ru^V.[22] On the other hand, the arguably reductive cleavage of the oxo bridge, with consequent loos of dimeric structure has also been proposed in literature.[33]

Meyer's findings strongly motivated the study of multinuclear molecules, and for several years, such complexes were generally believed to be a necessity in order to divide the proton coupled electron transfer process across several metal centers. This idea remained until Yong and Thummel clearly demonstrated that one metallic center

was enough[48]. Mononuclear ruthenium complexes appear to be able to assemble in a manner that allows the four PCET steps necessary to oxidize water. The first demonstration of catalytic water oxidation by a mononuclear ruthenium complex was achieved using trans-$[Ru(pbn)(4-R-py)_2(OH_2)]^{2+}$ (pbn = 2,2'-(4-(tert-butyl)pyridine-2,6-diyl)bis(1,8-naphthyridine); py = pyridine; R = Me) (Figure 1.6A).[48] Later, Meyer *et al*. reported the water oxidation by Ru(tpy)-(bpm)$(H_2O)^{2+}$ and Ru(tpy)(bpz)$(H_2O)^{2+}$ (tpy=2,20:60,200-terpyridine; bpm=2,20-bipyrimidine; bpz = 2,20-bipyrazine)[49].
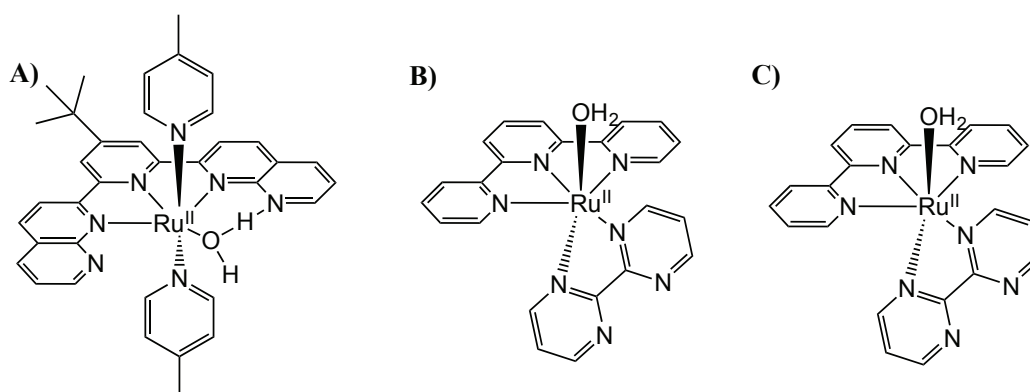
Figure 1.6 Structure of a) trans-$[Ru(pbn)(4-R-py)_2(OH_2)]^{2+}$.b) Ru(tpy)-(bpm)$(H_2O)^{2+}$ and c) Ru(tpy)(bpz)$(H_2O)^{2+}$

The mechanism for WOR mediated by Ru(tpy)-(bpm)$(H_2O)^{2+}$ and Ru(tpy)(bpz)$(H_2O)^{2+}$ has been carefully elucidated by a detailed kinetic analysis, including DFT calculation of the intermediates[49,50]. The oxidation on those catalyst occurs by sequential PCET oxidation of $[Ru^{II}-(OH)_2]^{2+}$ to $[Ru^{IV}=O]^{2+}$. Further oxidation is followed by nucleophilic attack by water to give $[Ru^{III}OOH]^{2+}$. The oxidation of the peroxidic intermediate gives $R^{IV}(OO)$. At this step two different pathways can be envisioned depending on the acidity of the media. The first, involves the displacement of oxygen by water at low acid contents (HNO$_3$ 0.1M). The second one comprises an additional oxidation step previous oxygen displacement. Figure 1.7 depicts the mechanism proposed in literature for the two mentioned complexes.

Figure 1.7 Mechanism proposed for a single-site WOR. Take from the reference [51]

Further evidence has highlighted the role of the proton accepting species in the mechanism shown in Figure 1.7 [52] For instance, the addition of HPO^{2-} promotes an enhancement of 3 orders of magnitude in the rate of oxygen evolution. This enhancement has been attributed to the oxygen transfer step occurring simultaneously with the abstraction of one proton by a base (B) (Equation 1.3). DFT calculations have revealed that this proton abstraction can take place even with a water molecule, which is also consistent with a significant Kinetic Isotopic Effect (KIE=6.6). The appearance of the so-called atom proton transfer (APT) step offers a low energy pathway by avoiding the high energetic intermediate $[Ru^{III}\text{-}OOH_2]^{3+}$.

$$(1.3)$$

In general terms, the mechanism shown in Figure 1.7 seems to be applicable to several mononuclear Ru WOCs. This has allowed the careful modification of the reactivity by varying the ligands attached to the active center.[49,51]

14

1.4.3 Iridium-based WOCs

1.4.3.1   Iridium oxide

IrO_x is one of the most efficient catalysts for WOR, usually recognized as the state of the art catalyst for Proton Exchange Membrane (PEM) electrolyzers. It can operate at low overpotentials and unlike RuO_2, exhibits remarkable robustness against corrosion in the presence of strong oxidants.

Typically IrO_x is used in the form of colloids, providing a high surface catalyst, which can be used even at very low concentrations. Also, kinetic measurements are more easily performed by standard transmission UV-spectroscopy, because the size of the particles is much smaller than the wavelength of light. Moreover, these nanoparticles can be easily incorporated into solid systems such as zeolites [53], SiO_2 [54,55] layer-by-layer assemblies [56,57] *etc.*

The classic method to prepare IrO_x colloids involve the hydrolysis of hexachloroiridate ($IrCl_6^{2-}$) salts in the presence of a stabilizer *e.g.,* citrate. In the case of citrate, this gives citrate-stabilized nanoparticles that appear as large aggregates (>100nm) of 15 nm particles[58]. Hoertz and co-workers reported a systematic study of the influence of the stabilizer on the size distribution and aggregation degree of such nanoparticles. Colloids obtained from bidentate stabilizers such as succinate, malonate and butyl malonate are composed of rather small 2 nm nanoparticles, in contrast to the large networks obtained with citrate. The formation of large aggregates in the case of citrate is due to the presence of a third carboxylate group oriented away for the IrO_x surface. The remaining two carboxylate groups bind the citrate to the IrO_x surface[59].

IrO_x colloids have been extensively used as an efficient catalyst in the photo-oxidation of water by $[Ru(bpy)_3]^{2+}$ [55,58,59]. A photocatalytic cycle for such a system is shown in Figure 1.8. In this scheme, light is absorbed by $[Ru(bpy)_3]^{2+}$ and the excited state of the sensitizer is formed. The latter is oxidized to $[Ru(bpy)_3]^{3+}$ by an appropriate sacrificial acceptor such as persulfate ($S_2O_8^{2-}$). Without a catalyst, no O_2 is formed and the sensitizer decomposes rapidly. In the presence of the catalyst the photosensitizer is recycled and O_2 is detected as a product.
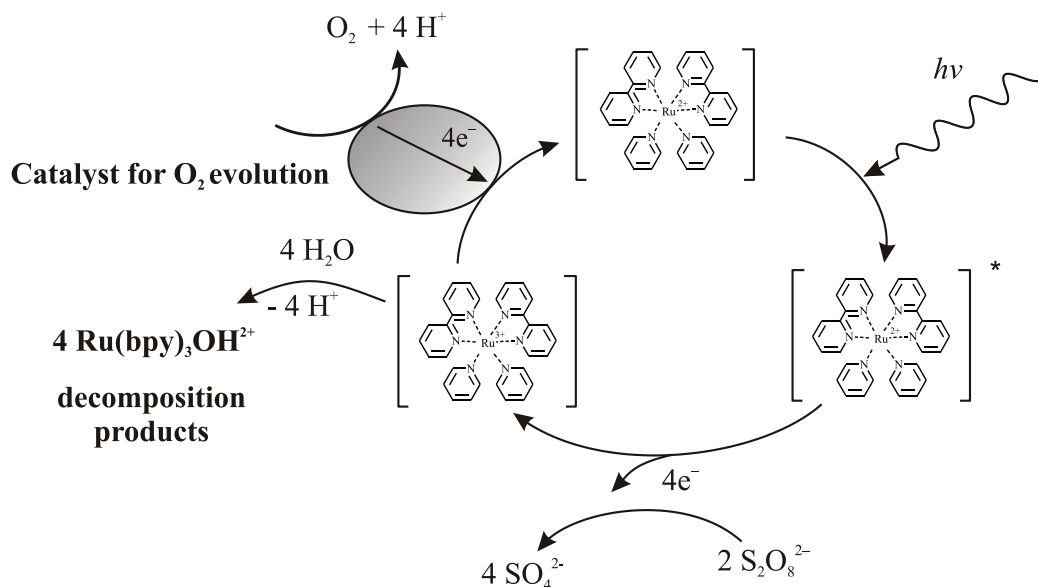
Figure 1.8 Schematic of the photocatalytic oxidation of water by the single phase $[Ru(bpy)_3]^{2+}$-catalyst system. Modified from the reference [58].

Morris and co-workers[60] reported that under conditions typically used during steady-state photolysis experiments, the rate-determining step is electron transfer between $[Ru(bpy)_3]^{3+}$ and the surface of IrO_x. This process occurs with a second-order rate constant of $1.3 \times 10^6 \text{ M}^{-1}\text{s}^{-1}$. Thus, it may be possible to design more efficient systems for photochemical oxygen evolution, and possibly non-sacrificial systems for overall water splitting, by using high local concentrations of sensitizer molecules (*e.g.*, by directly coupling the sensitizer to the colloid) or by increasing the driving force for electron transfer between the oxidized sensitizer and the colloidal catalyst.

More recently, Youngblood *et al.* reported water splitting in a photoelectrochemical cell incorporating the concept of a sensitized solar cell. The photoelectrochemical cell was constructed in a 2-compartment system, where the working electrode, composed of a porous nanocrystalline film on fluorinated tin oxide (F-SnO$_2$) and sensitized with a dye-IrO$_x$.nH$_2$O colloid, was placed in the first compartment. The ruthenium complex was designed to serve as both a sensitizer component and a molecular bridge to connect the IrO$_x$ catalyst to the TiO$_2$ surface. The second compartment contained both a reference electrode and a Pt counter electrode. Irradiation of this cell with visible light ($\lambda > 410$ nm) at bias potentials positive of –0.325 V *vs.* Ag/AgCl produced measurable anodic photocurrents with both O$_2$ and H$_2$ evolution. Although the efficiency of this system is low, achieving a

maximum quantum yield of 1%, it represents a proof-of-concept experiment for overall water splitting in a sensitizer–based photosystem [61].

In order to use IrO_x as a catalyst for solar or PEM applications, it is necessary to deposit it on the surface of an electrode. In this regard, several heterogeneization methodologies can be found in literature: physisorption[62], chemisorption[63], electrostatic attachment,[64] electrofloculation.[65-67] A brief introduction to those methodologies will be given in the introduction of Chapter 2.
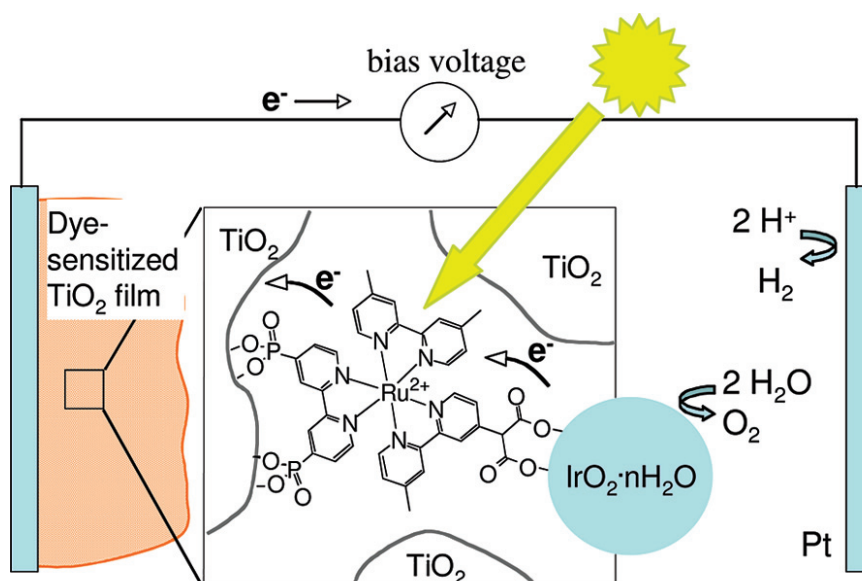
Figure 1.9 Scheme of the water splitting dye sensitized solar cell described by Youngblood[61].

1.4.3.2   Molecular Ir-based WOCs

Seminal work by Bernhard and co-workers showed that certain Ir complexes including unsubstituted or substituted 2-phenylpiridine ligands (ppy) (Figure 1.10 A) were catalytically active for WOR[68] Those complexes exhibited higher catalytic activities than the Ru analogues, working over much longer periods of time. The synthesis of those compounds held promise to isolate active intermediates and provide mechanistic insights, which are difficult to obtain in heterogeneous systems. However, the results have shown that those systems are as mechanistically problematic as their metal oxide counterparts, involving complex degradation pathways, often resulting in the formation of IrO_x.[69-71]

17

In 2009, Crabtree *et al* reported a new family of WOCs of the form Cp*Ir^{III}(chelate)X (Cp= Pentamethylcyclopentadienyl), improving the oxidation rate exhibited by Bernhard's catalysts[72]. The commercial availability of the precursor [CpIrCl$_2$]$_2$ and its ease of modification led to a quick increase in the number of reports dealing with those complexes and nowadays a large library of those compounds have been investigated.[69,71-81] Nevertheless, most of those catalysts exhibit lower performance than those firstly reported in 2009. Specially, the simplest catalyst of the family: the Cp*Ir monomer and the dimer containing only aqua and hydroxide ligands (Figure 1.10 D and E respectively) has shown the highest catalytic activities.
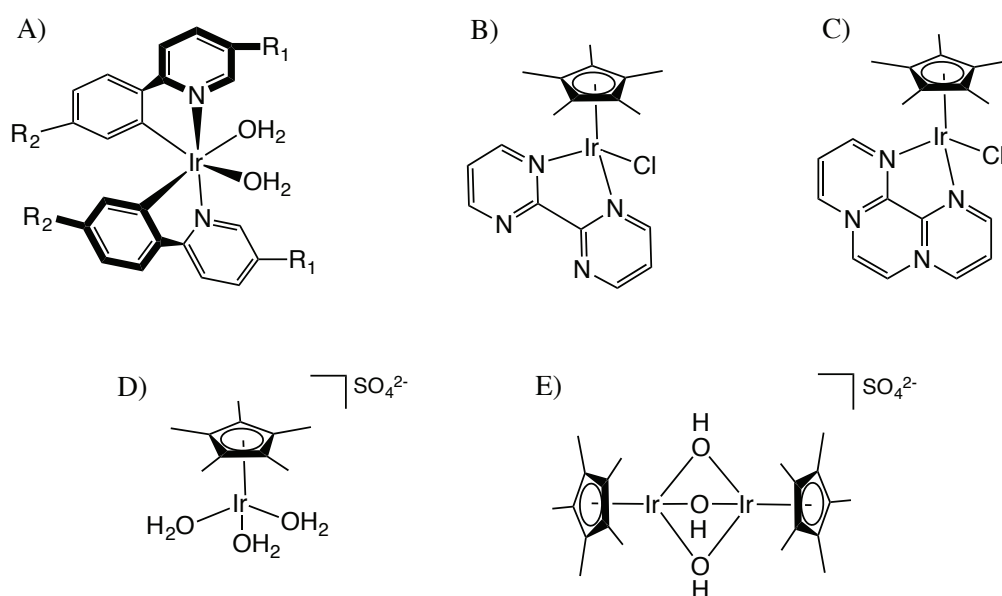
Figure 1.10 A) Structure of the family of catalysts reported by Bernhard and *et al*[68].(R1 and R2 are substituents in the form –H, -CH$_3$, -Ph, -Cl, -F); B-C) Typical Cp*Ir(chelate)X precatalysts for homogeneous regime; D-E) Typical precatalyst without chelate ligand for heterogeneous regime.

During WOR mediated by Cp-Ir catalysts, the Cp* moieties are lost by degradation in an activation step, while some of the ligands including O and N donor are retained[82]. Thus, in the case of the catalyst with chelating ligands (see Figure 1.10), the pre-activation step produces a new molecular catalyst (homogeneous regime) and various organic degradation products including acetic acid, formic acid and CO$_2$.[82] On the other hand, complexes with no chelate ligands give rise to IrO$_x$ clusters or nanoparticles, which are catalytic but no longer molecular species (heterogeneous regime)[70,74,77].

One important characteristic of the Ir-based molecular catalysts is their facile incorporation into solid matrixes. In the case of the aquo-complexes (catalysts of heterogeneous regime), the application of an anodic potential on an electrode leads to the formation of a blue layer of heterogeneous iridium material, which is very active catalyst for WOR[69,74,75]. These deposits, have been characterized as $[IrO_x]n$ nanoclusters, (with n in the range of 4-6) embedded in an organic matrix, product of Cp* degradation[75]. On the other hand, the catalysts obtained by mixing complexes of the form Cp*Ir(chelate)X (see Figure 1.10) with Ce(IV) or IO_4^-, adsorb spontaneously on nearly all oxide surfaces including the popular solar cell substrates such as TiO_2 and α-Fe_3O_4 (hematite)[83] The stable attachment formed is a clear advantage over the synthesis of complexes including ligands with anchoring groups.

A full mechanism for WOR mediated by molecular Ir-based catalysts is not yet available. The fast turnover and consequent poorly resolved nature of the intermediary species, has greatly hindered obtaining mechanistic details. However, it is assumed that the Cp* moiety is sequentially oxidized by oxo-Ir and peroxo-Ir species through O insertion steps. Figure 1.11 shows the spectrum of oxidized Cp*Ir complexes during Cp* degradation as reported by Macchione and Crabtree[71,82]. All those complexes are catalytic for WOR, being dimeric di-oxo bridged complex, reminiscent to the Ru blue dimer (Figure 1.5), the most active.
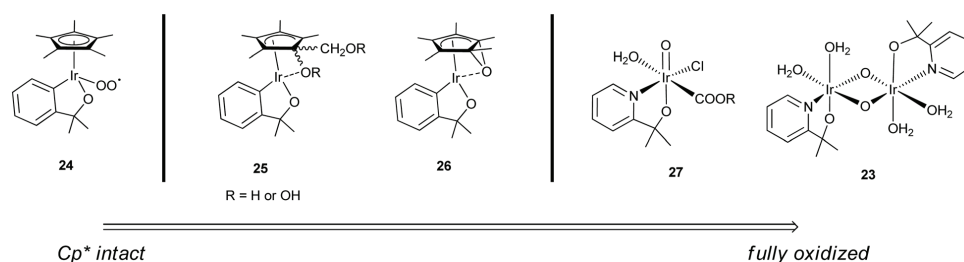
Figure 1.11 Spectrum of oxidized Cp*Ir complexes according to the intermediaries detected by Macchioni and Crabtree[71,81,82]. Figure taken from the reference [81].

Based on the studies of Ru analogues, two different mechanisms for WOR mediated by Ir-based complexes are proposed: WNA and ROC.[23] In both cases, the formation of the Ir(V)=O intermediate with a radical character seems to be crucial in the formation of the O-O bond as described in the section 1.3.

1.5   Catalytic hydrogen evolution reaction.

The hydrogen evolution reaction is the cathodic part of the overall water splitting (Eq. 1.1), involving the transfer of 2 electrons at a thermodynamic potential of 0V *vs.* SHE. Despite the simplicity of this process, it requires a catalyst due to the high-energy barriers associated with the formation of the partially reduced hydrogen radical (2.8V *vs.* SHE)[84]

The catalysts for HER can be classified in two main groups: homogenous and heterogeneous, depending whether they are or not in the same phase than the reactant. Examples of homogenous catalysts are water-soluble molecular or enzymatic catalysts. [85] On the other hand, heterogeneous catalysts comprise insoluble solids *e.g.,* metals, metallic oxides.[86,87] Herein, we will focus in the latter group as being Pt the HEC used in this thesis. Homogeneous HECs are not discussed.

The mechanism of HER at a solid surface, and in acidic solutions can be described as follows:

(Volmer step) $\quad\quad M + H^+ + e^- \rightarrow M - H_{ads}$ $\quad\quad\quad\quad\quad$ (1.4)

(Tafel step) $\quad\quad\quad M - H_{ads} + M - H_{ads} \rightarrow 2M + H_2$ $\quad\quad\quad$ (1.5)

(Heyrovsky step) $\quad\quad M - H_{ads} + H^+ + e^- \rightarrow M + H_2$ $\quad\quad\quad$ (1.6)
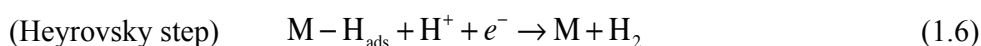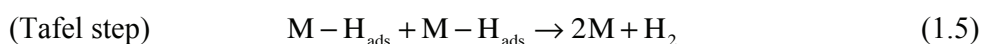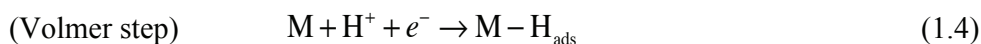
The first step (Eq. 1.4) is the reductive adsorption of a proton yielding M-H$_{ad.}$ (Volmer step). Then, hydrogen evolution can occur *via* chemical or electrochemical steps according to the equations 1.5 and 1.6, respectively. In the chemical step (Tafel step), the release of hydrogen takes place by the coupling of two adsorbed M-H$_{ad}$ units. Alternatively, in the electrochemical step (Heyrovsky step, Eq. 1.5), the reduction of one additional proton is required. The presence of one or another mechanism for H$_2$ release will depend on the particular system, and can be experimentally determined by the use of Tafel plots.[88]

The pre-adsorption step represented by equation 1.4, makes HER a highly surface-dependent reaction, with reaction rates spanning over several orders of magnitude[89]. The surface-dependence of this reaction is better seen if the standard electrochemical rate constant k^0 (or the exchange current density in logarithmic scale as seen in Figure 1.12), is plotted as a function of the strength of the M-H bond (or the free energy for H^+ adsorption). The result is a "volcano curve" as shown in Figure 1.12. At low M-H strength where formation of the adsorbed intermediate is the rate-determining step (RDS), the plot rises as the M-H bond becomes stronger. Then, a maximum is attained, to finally observe a steady decrease in k^0. In the later region of the curve, the Volmer step is fast and the release of hydrogen *via* Tafel or Heyrovsky steps become RDS. Thus, the decrease in the rate can be interpreted as an over-stabilization of the absorbed intermediate, favoring reactants in the reactions 1.5 and 1.6.
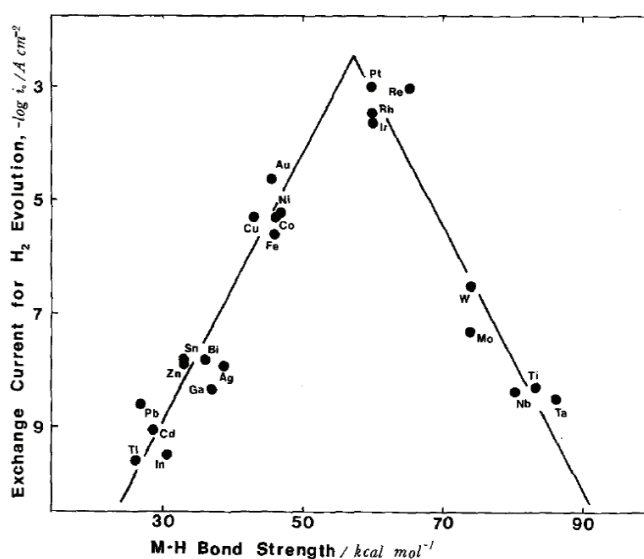
Figure 1.12 Exchange currents for electrolytic hydrogen evolution *vs.* strength of intermediate metal-hydrogen bond as reported by Trasatti. Taken from the reference [89].

One important consideration when analyzing the surface-dependence of the HER is the pH to which the reaction is assessed. In the previous analysis, we considered the HER taking place in acidic medium, hence assuming that the M-H$_{ads}$ intermediate is formed from the hydronium cation (Eq.1.4). However, in alkaline media the main source of protons is water, and then the formation of M-H$_{ads}$ requires the cleavage of

the O-H bond. Under those conditions, the strength of the M-H bond fails as a descriptor for HER, and the trends observed in Figure 1.12 are drastically modified. For instance, in acidic media the reaction rates for Ag, Cu and Au, are in the order Ag<Cu<Au, as shown in Figure 1.12. However, this trend is reversed in basic media, signaling that the rate of HER may be controlled by the dissociation energy of water rather than by the adsorption energy of hydrogen[90]

The reliability of the volcano plots has been matter of controversy due to the uncertain nature of some of the metallic surfaces used to assess HER.[90,91] Whereas the ascending branch in the Trasatti's plot is rather convincing, the descending branch is composed mainly by metals which are covered by an oxide film (*e.g.*, W, Mo, Ti, Ta), thus obscuring their real activity towards HER. Consequently, a direct correlation between M-H energetics and activity is occasionally misleading. Despite this, the volcano plots remain useful for the qualitative analysis of catalysts for HER, not only in pure metals but also in alloys and enzymes. [92,93]

In the following section two groups of heterogeneous systems for HER will be briefly presented: as based on *(i)* precious metals; and *(ii)* non-precious metals and alloys. Other catalytic systems such as chalcogenides, borides, carbides, *etc…* will not be discussed.

1.6 Hydrogen evolution catalysts

1.6.1 Precious metals

The presence of the Pt-group metals (Pt, Ru, Ir, Rh, Pd) at the top of the "volcano plot" (Figure 1.12) makes them the best performing catalysts for HER, forming M-H with an ideal strength to allow fast adsorption but also ease releasing of molecular H_2. However, the scarcity of those metals and consequent high prices remain as an issue for practical applications. Alternatives to decrease the loading of Pt have been the use of nanostructured materials, increasing the specific surface and therefore number of active centers [94-96] *Chen et al.* reported the formation of a monolayer of Pt on WC.[97]

This approach allowed a reduced loading of Pt by an order of magnitude without compromising the activity. The formation of alloys with less expensive metals has also been reported as a useful strategy. Based on DFT calculations, Norskov *et al.* found that the alloy formed between Pt and Bi was a good candidate with high activity towards HER[93]. The alloyed material obtained by underpotential deposition of Bi on Pt, followed by annealing, exhibited 50% higher HER current density than the initial Pt, in good agreement with computational predictions.

1.6.2 Non-precious metals and alloys

Non-noble metals are typically used in basic media due to their tendency to corrode in the presence of acids. In this group, Ni-based catalysts are the most representative example, being used for decades as electrode for HER in alkaline electrolyzers[98]. However, Ni-based catalysts suffer from an insufficient activity and more importantly a progressive deactivation due to the formation of Ni-hydrides[98-100]. Efforts to provide stabilization have resulted in the use of catalysts of the type Raney-Ni, an Ni-Al alloy, which in basic media leaches Al from the surface, providing a high-surface Ni-catalyst.[101] In those catalysts, the Al skeleton acts as matrix, stabilizing the highly dispersed Ni.

Besides Raney-Ni, other alloys have also been explored as effective catalysts for HER. Vasu and coworkers studied several binary Ni alloys and assessed their activity towards HER in basic solution[102]. From their work, the best HEC was the Ni-Mo alloy exhibiting an outstanding catalytic performance, working at high currents (300mA cm^{-2}) and moderate overpotentials (180 mV). The mechanism by which Ni-Mo alloys exhibit an enhanced catalytic activity is not clear. Some authors argued that the enhancement is strictly due to an increase in the active surface area, consistent with the increase of the activity after some minutes of reaction, when some Mo has leached from the surface[103,104]. On the other hand, some researchers have suggested electronic synergy, in which the Ni–Mo alloy or intermetallic phase offers more favorable energetics for HER than the two independent metals.[105-107]

One inherent disadvantage to carry out HER in basic media is the requirement for the dissociation of the water molecule. This is usually revealed by catalytic activities of about two or three orders of magnitudes lower than in acid. This recognition started

the development of bifunctional or pseudomonofunctional catalysts of the form $Ni(OH)_2/M$. In those systems, the $Ni(OH)_2$ sites promote the water cleavage step. Then, the recombination of the as-formed intermediates takes place at the M sites. Following this strategy, Danilovic *et al* reported that the pseudomonofunctional catalysts $Ni(OH)_2/Ni$ can operate at rates four times higher than the bare Ni.[90] Remarkably, the reactivity trends established in acidic media (according to Figure 1.12) are re-established in alkaline solution (see section 1.5) by the modification of those metals with $Ni(OH)_2$ (*i.e.,* $Ni(OH)_2/Ag > Ni(OH)_2/Cu > Ni(OH)_2/Au$), implying that the rates are dependent again on the M-H energetics.

.

1.7 HER at soft interfaces in LEPA

Processes occurring at the interface between two immiscible electrolyte solutions (ITIES) have attracted considerable attention over the past three decades, mainly due to their similarities with biological processes, where specialized membranes are responsible for the synthesis of many chemical species (*e.g.,* ATP, oxygen, NADPH, etc.). In these systems, the driving force is the potential difference established across the membrane, which also provides one effective route for the separation of chemical species according to their hydrophobicity. A biological membrane can be viewed as a water-oil-water three-phase system, encompassing two water-oil liquid-liquid interfaces. Hence, the ITIES may be used as a simple model to describe one-half of a biological membrane.

With this in mind, over the last few years our laboratory has devoted many efforts to conceive bio-inspired systems for energy conversion based in ITIES. In particular, HER has been of great interest in the frame of a long-term project involving the concept of *batch water splitting in biphasic systems*, where the electrons needed for the hydrogen evolution reaction are provided from WOR occurring at other liquid-liquid interphase. (Figure 1.13).
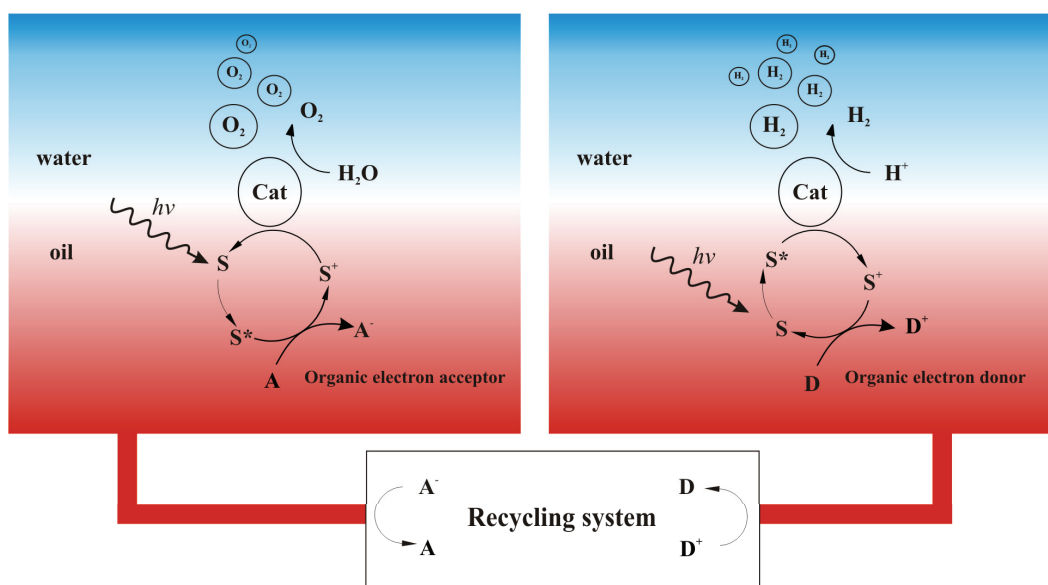
Figure 1.13 General scheme of batch water splitting in biphasic systems.

In a series of publications our group has demonstrated that under anaerobic conditions, protons pumped from the aqueous solution into the organic phase of biphasic systems (Figure 1.14), may be reduced using lipophilic weak electron donors, such as decamethylferrocene (DMFc), that are thermodynamically incapable of reducing aqueous protons[108-111].
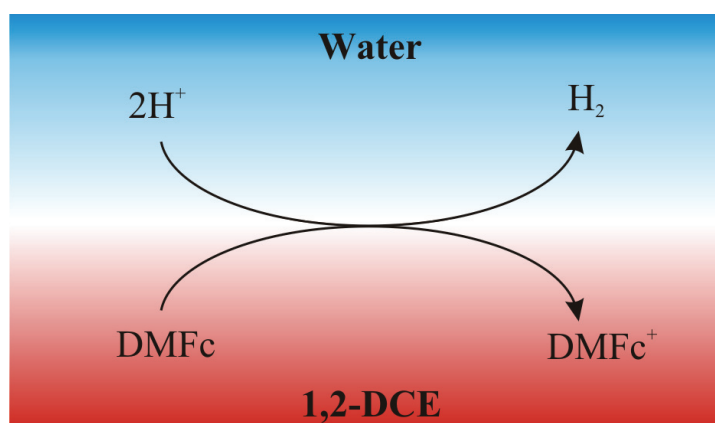
Figure 1.14 Hydrogen evolution at ITIES using an organic electron donor, here decamethylferrocene (DMFc).

This enhanced reactivity of protons has been rationalized based on the variations on thermodynamic barriers that occur when chemical species are transferred into a media with different physicochemical properties.

Figure 1.15 illustrates the redox scales at the water|1,2-DCE interface for various reactions. These values have been calculated by using the thermodynamic potentials in water, and the different Gibbs energy transfer for reactants and products into the organic phase[112]. Notably, the reduction of protons was shifted positively over half a volt in the organic solvent, accounting for its facile reduction by DMFc ($\left[E^0_{DMFc^+/DMFc} \right]^{DCE}_{SHE} = 0.44$). Conversely, processes involving the appearance of charged species, such as WOR, occur at a higher potential. In this case, kinetic effects might play an important role, as it will be discussed in detail in Chapters 4-5.
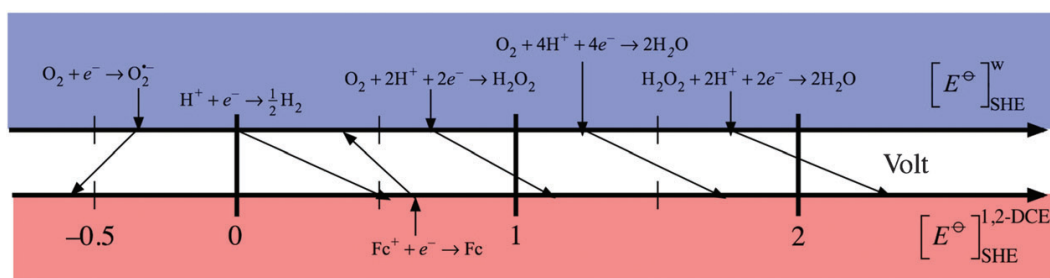
Figure 1.15 (Top) (Bottom) Redox potential scale for oxygen in water (top scale) and in 1,2-dichloroethane (bottom scale) *vs.* the Standard Hydrogen Electrode (SHE). Figure taken form the reference 112

The mechanism by which metallocenes produce H_2 is not fully understood. However, it seems to proceed by an initial protonation of DMFc with the formation of $[DMFc\text{-}H]^+$. Then, two protonated $[DMFc\text{-}H]^+$ can react to form two $2DMFc^+$ and H_2. Alternatively, the hydride form of the protonated complex $[DMFc^{IV}\text{–}H]^+$ can be attacked to yield $[DMFc^{IV}]^{2+}$ and H_2, followed by a reduction of $[DMFc^{IV}]^{2+}$ by DMFc. A third possibility involves the reduction of $[DMFc\text{-}H]^+$ into $[DMFc\text{-}H]$ followed by a proton attack. The full mechanism involving the adsorption step and the three different possibilities for hydrogen evolution is shown in the equations 1.7-1.11

Protonation:

$$DMFc + H \rightarrow [DMFc - H]^+ \qquad\qquad (1.7)$$

Bimolecular reaction:

$$2[DMFc - H]^+ \rightarrow [DMFc^{III}]^+ + H_2 \qquad\qquad (1.8)$$

Proton attack pathway:

$$[DMFc - H]^+ + H^+ \rightarrow [DMFc^{IV}]^{2+} + H_2 \qquad\qquad (1.9)$$

$$[DMFc^{IV}]^{2+} + DMFc \rightarrow 2[DMFc^{III}]^+ \qquad\qquad (1.10)$$

Reduction Pathway:

$$[DMFc - H]^+ + DMFc \rightarrow [DMFc - H] + [DMFc^{III}]^+ \qquad\qquad (1.11)$$

$$[DMFc - H] + H^+ \rightarrow [DMFc^{III}]^+ + H_2 \qquad\qquad (1.12)$$
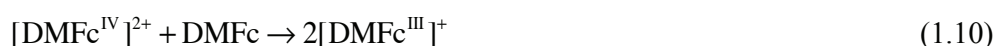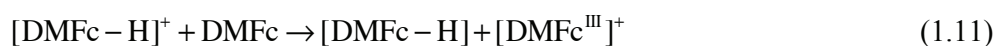
It should be noted that the protonation (Eq.1.7) and the hydrogen evolution reactions (Eq.1.8-1.10), resemble the Volmer, Tafel and Heyrovsky steps previously described in the section 1.5 for HER at solid catalysts.

Further studies have shown that the biphasic HER by DMFC can be easily catalyzed by Pt and other more earth-abundant "floating catalytic rafts" such as molybdenum disulfide (MoS_2) and molybdenum carbide (Mo_2C) nanoparticles grown on carbon supports such as carbon nanotubes or reduced graphene oxide.[110,111,113-115]

Besides DMFc, other metallocenes such as Osmocene (Oc)[116], decamethylosmocene (DMOc)[117] and decamethylruthenocene (DMRu)[118] , have also been proven to evolve H_2 in biphasic systems. In such systems, the reaction takes place by mechanisms involving the photoactivation of the metalocene, which acts as both, electron donor and sensitizer.

1.8 Layer-by-layer deposition

1.8.1 Generalities

Multilayered materials have attracted much attention for decades due to their application in many areas such as: nanoelectronics,[119] sensors,[120,121] electrocatalysis.[122-124] They can be prepared by several methods including: Langmuir Blodgett, chemisorption, electrostatic layer-by-layer deposition (*E*LbL). Among them, *E*LbL deposition offers some crucial advantages. For instance, the formation of the *E*LbL assemblies is achieved by the sequential adsorption of oppositely charged species, removing any special requirement for chemical affinity. On the other hand, as compared to the other methods, *E*LbL is considerably easier to implement, requiring almost no equipment and eliminating the restriction in the substrate size and topology. In the present work the electrostatic layer-by-layer (*E*LbL) will be referred simply as LbL unless otherwise stated. Other types of LbL assemblies will be briefly mentioned at the end of this section.
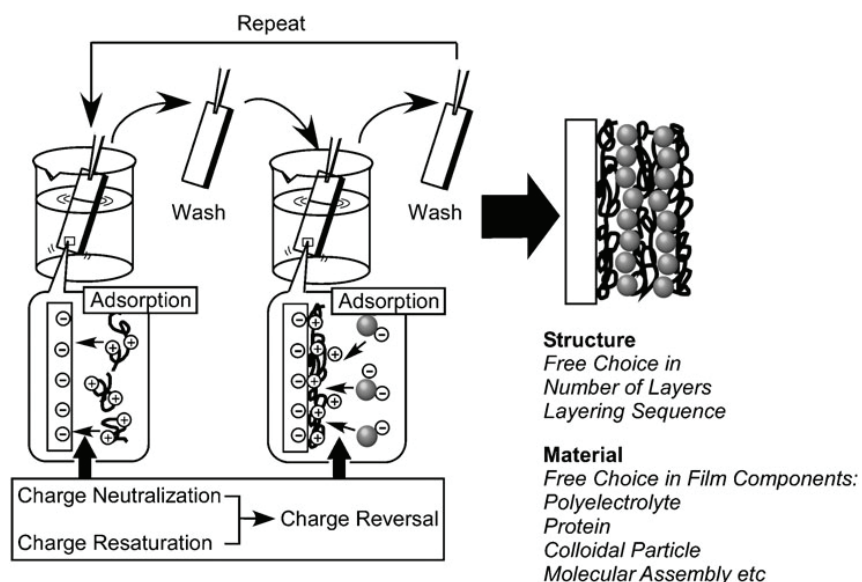
Figure 1.16 Outline of LbL assembly through electrostatic interaction. Taken from the reference [125]

The LbL method consists in the alternate exposure of a substrate to solutions containing charged species (Figure 1.16). An intermediate rinsing step is also included in order to remove the loosely adsorbed species and to prevent contamination of the next adsorption solution. The adsorption of species carrying more than one charge *e.g.,* polyiones or nanoparticles, leads to charge reversal on the surface, allowing the next species with opposite charge to be adsorbed. The charge excess is also advantageous for the self-regulation of the film, which repels equally charged species, thus restricting the adsorption to a monolayer.

The LbL method was first described by Iler in 1966 for the co-deposition of positively charged bohemite (alumina) and negatively charged silica particles.[126] However, the field remained relatively undeveloped until the early 90s, when Decher and coworkers reported the formation of assemblies composed of positively and negatively charged amphiphiles[127]. This was followed in 1992, by the first report of LbL buildup films based exclusively on polyelectrolytes[128]. The study investigated the LBL films formed from: sodium poly(styrenesulfonate) (PSS) and potassium poly(vinylsulfate) (PVS) as polyanions; and poly-[diethylmethyl(4-vinylbenzyl)ammonium iodide] and poly(allyl-amine hydrochloride) (PAH) as polycations. The finding of a linear correlation between the number of layers deposited and the thickness of the material opened new avenues for the precise control over thickness in those materials at nanoscale level. Since then, the field of LbL has rapidly grown, and to date a wide range of species have been deposited: clay particles[129,130], nanoparticles[131-135] and biologic material such as DNA and proteins [136-140] etc. Consequently, LbL assemblies have been used for many applications in coatings, optics, biomedical, electronics, sensors, and photonics.[119,121,125,141,142]

The properties of the LbL assemblies depend on many factors, such as the concentrations of the two charged species, temperature, adsorption times, ionic strength, and quality of the surface. In general, concentrations of few milligrams per milliliters are enough to reach the plateau of the adsorption isotherm. On the other hand, typical adsorption times are in the range of few minutes for polyelectrolytes. If those parameters are carefully controlled, the LbL leads to highly reproducible deposits.

One important property of the layer-by-layer assemblies is the high degree of interpenetration between the adjacent layers[119,143,144]. Notheworthy, in the case of LbL

films containing redox active species, the "fuzzy character" of the assemblies facilitates the charge transfer between neighboring sites. Schlenoff and coworkers studied the electrochemical properties of LbL made from of poly(styrenesulfonate) and poly(butanylviologen)[145]. Their results suggested that due to the high interpenetration of the bilayers, at least four layer pairs are required to fully insulate one redox active layer from another, thus allowing all the centers in the films to be electrochemically addressable.

The use of the electrostatic approach remains the most used due to the intrinsic versatility as discussed *vide supra*. However, other interactions have been also included in order to trigger a special architecture, or to provide the assemblies with specific properties. For instance, Stockton *et al.* demonstrated the pH-triggered dissolution in assemblies based on hydrogen-bonding interactions[146,147] On the other hand, the use of covalent interactions has been reported as an effective way to increase the robustness of the multilayers.[148]

1.8.2 Immobilization of NPs in LbL films: Selected applications

The use of colloidal NPs as building blocks for LbL films was soon introduced after the seminal work by Decher on polyelectrolytes. In, 1994 Ferguson *et al.* reported the formation of assemblies of Hectorite, a mica-type layered silicate, and PDDA.[129] When stirred in water, Hectorite exfoliates into crystalline sheets that are ≈1 nm thick and 25-35 nm in diameter. The sheets bear a negative charge, which is balanced by Na cations, and exchanged with PDDA upon deposition. The eplipsometry data showed a linear increase in the thickness, with the adsorption of polymer and silica contributing in 1.1 nm and 2.1 nm respectively. Moreover, the X-ray data of the films provided evidence of structural order, which was preserved even in films as thick as 0.2 micrometer.

Another report providing evidence of highly ordered LbL materials was described by Decher *et al.*[149], where multilayer films composed of polymeric bilayers (PE) and Au NPs, deposited on a silicon substrate were studied. The formation of the Au/PE material starts by the alternate deposition of PSS and PAH on an imine-modified silicon substrate. Then, the uppermost layer of PAH provides a positively charged surface for self-assembly of a monolayer of Au NPs. By repeating the overall process,

a multilayer of the form [(PSS/PAH)$_m$Au/PAH]$_n$ is obtained. They demonstrated by UV-Vis spectroscopy and X-ray reflectivity studies, that Au/PE super lattices can be formed with either a layered or disordered structure by manipulating the thickness of the PE interlayer (m), relative to the size of the metal NPs. Particularly, for films composed of 4 multilayers (*i.e.,* n=4), they found that when only one pair bilayer of PE (m=1) is placed between two consecutive AuNPs layers, only broad oscillations due to X-ray scattering are observed. However, for m > 3, the presence of multiple Bragg reflections seen in X-ray reflectivity data, provided evidence of highly stratified Au layers.

A similar concept was later applied by Ferreyra and coworkers, who described the electrostatic LbL assemblies of Au NPs with a viologen-based cationic redox polyelectrolyte (PV).[150] The stepwise growing of the layers was followed by UV-Vis absorption, elipsometry, electrochemical quartz microbalance, and by the electrochemical processes in viologen moieties. The measurements of the thickness *via* elipsometry measurements showed that while the PV adsorption does not contribute significantly to the thickness, an increase of 4.4 ± 0.5 nm is observed upon deposition of each Au PP layer. This thickness is smaller than the 6.4 nm diameter of the NPs nanoparticles, implying a substantial overlap between adjacent Au layers.

The methods previously described have been extrapolated by the incorporation of specific receptors into the assembly. Thus, while Au NPS provide a conductive matrix, the receptor gives specific sensing properties to the multilayered material. For instance, Stoddart *et al.* reported the LbL deposition of charged Au NPs with two positively charged receptors: cyclobis(paraquat-p-phenylene) cyclophane (1 in Figure 1.17), cyclobis(paraquat-p-biphenylene) cyclophane (2 in Figure 1.17). The receptor units exhibit electron acceptor properties, thus electron-donating analytes exhibiting redox properties could be analyzed by the receptor-crosslinked Au NPs. The selectivity is then be governed by the specific binding affinity of the donor substrate and also the supramolecular fit of the analyte in the cavity of the receptor.

Another interesting application of LbL films is the fabrication of photoelectrochemically active composites. Kotov *et al.* reported the assembly of CdS, PbS and TiO$_2$ NPs, on various substrates (*e.g.,* quartz, glass, Au and Pt)[132]. Interestingly, the absorption properties of CdS and PbS NPs were seemingly unaffected upon deposition. The absorption of the films was found to increase

monotonously with the number of layers. Nevertheless, the photocurrents reached a maximum at 10 bilayers.
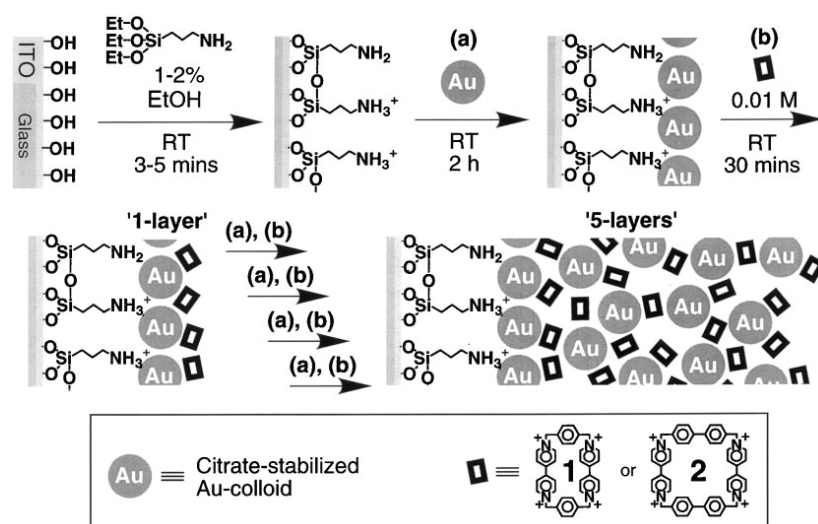
Figure 1.17 Stepwise assembly of the three dimensional array of the bis-bipyridinium cyclophane crosslinked Au-nanoparticle superstructure on a conductive ITO support. Taken from ref [151].

Alternatives to light responsive semiconductors have been the use of hybrid materials containing Au NPs and organometallic chromophores. Typically, the surface of a conductive electrode (*e.g.,* ITO) is modified with an aminopropyl siloxane layer, rendering a positively charged substrate. Then, an alternate assembly of AuNPs and sensitizer is performed. Examples of sensitizer molecules forming light responsive LbL assemblies with AuNPs are: Ru(II)-*tris*-(2,2′-bipyridine) cyclobis (para-quat-p-phenylene) catenane, and Zn(II)-protoporphyrin IX-bis(*N*-methyl-*N*′-undecanoate-4,4′-bipyridinium).[152] Upon irradiation of the electrode in a photochemical system containing a sacrificial electron donor (*e.g.,* Na$_2$EDTA), photocurrents are observed. In both cases, the photocurrents increase with the number of layers. However, the increase is not linear, most likely due to scattering of the light in thick films and the partial absorption of light from the AuNPs.

Previous work in the group of Professor Girault was devoted to the study of light-responsive LbL films of CdSe quantum dots (QDs), in organic solutions.[153] These systems, as previously reported by Corn *et al.*[154,155], represent a good alternative for the study of processes happening at the ITIES, where the multilayer

assembly acts as a pseudo-liquid phase. The films were built by the alternate deposition of poly-L-Lysine (pLys) and poly-L-Glutamic acid (pGlu) and on a 11-mercaptoundecanoic acid-modified gold surface. In each case, the deposition process finishes with the adsorption of pLys layer, thus rendering a positively charge surface. This is followed by immersion step in a solution containing ferri/ferrocyanide ions, incorporating ions into the film, thus making it electroactive. Then, in a final step, the citrate stabilized QDs are adsorbed on the positively charged surface. Figure 1.18 shows schematically the LbL assembly obtained with the protocol describe above.
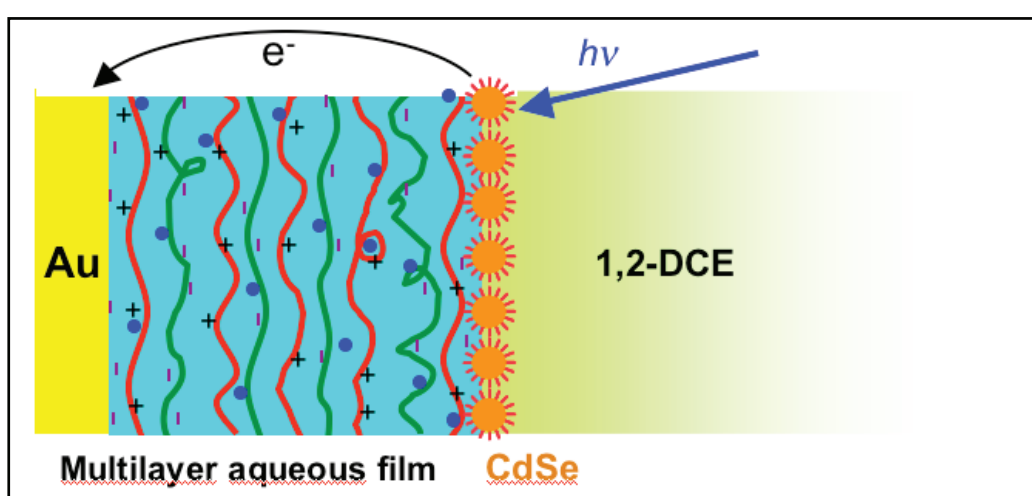
Figure 1.18. Scheme of the LbL assembly as reported by Hojei and coworkers.[153]

Illumination of the modified electrode in DCE solution leads to the formation of electron-hole pairs in the CdSe QDs, and subsequently charge transport inside the film, mediated by of ferri/ferrocianide redox shuttle. The photocurrent responses were analyzed by a detail kinetic model, where the rate constants for electron transfer were found to depend on the potential difference between gold and the organic electrolyte solution, as well as on the thickness of the multilayer assembly. Importantly, the dependence on the potential becomes markedly weaker in films with more than 7 pLys/pGlu bilayers, implying that the electric field at the gold|film interface spreads over 5-7 polyelectrolyte layers.

In a subsequent report, assemblies of the form (pLys/CdSe)$_n$ and (pLys/CdSe@CdS)$_n$, in which the NPs function both as a sensitizer and a mediator

were studied.[131] Again, the multilayered system was tested in an organic solvent, then acting as the aqueous side of a liquid-liquid system. Time-resolved fluorescence measurements showed that the fluorescence decay of the NPs in the multilayer films is slightly different from that in solution, but similar regardless of the film thickness. Another important result was that upon irradiation, $(pLys/CdSe)_n$ films exhibit mainly cathodic currents, most likely due to the reduction of oxygen in the solutions. Conversely, in the case of $(pLys/CdSe@CdS)_n$ films, mainly photoanodic currents are recorded, probably due to WOR.

1.9   Scope of the present work

The Laboratory of Physical and Analytical Electrochemistry (LEPA) have long been interested in the study of processes happening at the interface between two immiscible liquids (ITIES). Those interfaces provide a well-defined platform for fundamental studies of adsorption processes and molecular reactivity. Moreover, they can act as boundary membranes, useful for the separation products of light-activated chemical reactions.

In a series of publications, our laboratory has shown that the protons pumped from the aqueous into the organic phase of a liquid-liquid system, can be reduced by some metallocenes, *via* chemical or photochemical reactions. This resulted in the idea of *batch water splitting at biphasic systems*, where the electrons needed for the reduction of H^+ into H_2, are obtained from the water oxidation at other liquid-liquid interface. Nevertheless, the recognition of the instability of most of the organic solvents used in liquid-liquid studies (*e.g.*, 1.2 DCE, α,α,α-Trifluorotoluene.) under the harsh conditions required for WOR (*i.e.*, degradation in the presence of Ce^{IV} and $[Ru^{III}(bpy)_3]^{3+}$) led us to the idea of using an "unusual" liquid-liquid system: water/acetonitrile mixtures.

The water/ACN mixtures provide a heterogeneous environment at molecular level, with the coexistence of both, water and acetonitrile clusters. Additionally, the outstanding stability of acetonitrile makes it suitable for WOR–related studies. In this regard, this thesis is conceived to provide the foundation towards the development of systems for overall water splitting using liquid-liquid interfaces.

In Chapter 2 we present a strategy to deposit citrate-stabilized IrO_x NPs using a layer methodology. This strategy is after expanded in Chapter 3 to the use of inkjet printing technologies, in this case with application in pH–sensing electrodes.

Chapters 4 and 5 are devoted to the study of water oxidation by $[Ru^{III}(bpy)_3]^{3+}$ mediated by IrO_x NPs in water/ACN mixtures. In Chapter 4 we performed a detailed kinetic study of this process analyzing several factors such as acidity and water contents, and interpreting the results based on the structure of water in those mixtures.

Those results are complemented in Chapter 5 with a study by cyclic voltammetry using the PDDA- IrO_x modified electrodes as described in Chapter 2.

Finally in Chapter 5 we present an example of a light driven water oxidation and hydrogen reduction by tetrathiafulvalene (TTF) in ACN and water/ACN mixtures.

1.10 Bibliography

[1]   Chen, H.; Cong, T. N.; Yang, W.; Tan, C.; Li, Y.; Ding, Y. *Progress in Natural Science* 19, (**2009)**, 291-312.

[2]   Lund, H.; Salgi, G. *Energy Conversion and Management* 50, (**2009)**, 1172-1179.

[3]   Barber, J. *Chemical Society Reviews* 38, (**2009)**, 185-196.

[4]   Andreiadis, E. S.; Chavarot-Kerlidou, M.; Fontecave, M.; Artero, V. *Photochemistry and Photobiology* 87, (**2011)**, 946-964.

[5]   Kärkäs, M. D.; Verho, O.; Johnston, E. V.; Åkermark, B. *Chemical Reviews* 114, (**2014)**, 11863-12001.

[6]   Rüttinger, W.; Dismukes, G. C. *Chemical Reviews* 97, (**1997)**, 1-24.

[7]   Sartorel, A.; Carraro, M.; Toma, F. M.; Prato, M.; Bonchio, M. *Energy & Environmental Science* 5, (**2012)**, 5592-5603.

[8]   Stripp, S. T.; Happe, T. *Dalton Transactions*, (**2009)**, 9960-9969.

[9]   Allen, J. F.; de Paula, W. B. M.; Puthiyaveetil, S.; Nield, J. *Trends in Plant Science* 16, (**2011)**, 645-655.

[10]   Meyer, T. J.; Huynh, M. H. V.; Thorp, H. H. *Angewandte Chemie International Edition* 46, (**2007)**, 5284-5304.

[11]   Joliot, P.; Kok, B. *In Bioenergetics of Photosynthesis*; Academic Press: New York, 1975.

[12]   Yachandra, V. K.; Guiles, R. D.; McDermott, A.; Britt, R. D.; Dexheimer, S. L.; Sauer, K.; Klein, M. P. *Biochimica et Biophysica Acta (BBA) - Bioenergetics* 850, (**1986)**, 324-332.

[13]   Yachandra, V. K.; Guiles, R. D.; McDermott, A. E.; Cole, J. L.; Britt, R. D.; Dexheimer, S. L.; Sauer, K.; Klein, M. P. *Biochemistry* 26, (**1987)**, 5974-5981.

[14]   Penner-Hahn, J. E.; Fronko, R. M.; Pecoraro, V. L.; Yocum, C. F.; Betts, S. D.; Bowlby, N. R. *Journal of the American Chemical Society* 112, (**1990)**, 2549-2557.

[15]   Yachandra, V.; DeRose, V.; Latimer, M.; Mukerji, I.; Sauer, K.; Klein, M. *Science* 260, (**1993)**, 675-679.

[16]   Latimer, M. J.; DeRose, V. J.; Mukerji, I.; Yachandra, V. K.; Sauer, K.; Klein, M. P. *Biochemistry* 34, (**1995)**, 10898-10909.

[17]   Umena, Y.; Kawakami, K.; Shen, J.-R.; Kamiya, N. *Nature* 473, (**2011)**, 55-60.

[18]   Yano, J.; Yachandra, V. *Chemical Reviews* 114, (**2014)**, 4175-4205.

[19]   Yano, J.; Yachandra, V. K. *Inorganic Chemistry* 47, (**2008)**, 1711-1726.

[20]   Yano, J.; Yachandra, V. K. *Photosynthesis Research* 92, (**2007)**, 289-303.

[21]   Weinberg, D. R.; Gagliardi, C. J.; Hull, J. F.; Murphy, C. F.; Kent, C. A.; Westlake, B. C.; Paul, A.; Ess, D. H.; McCafferty, D. G.; Meyer, T. J. *Chemical Reviews* 112, (**2012)**, 4016-4093.

[22]   Liu, F.; Concepcion, J. J.; Jurss, J. W.; Cardolaccia, T.; Templeton, J. L.; Meyer, T. J. *Inorganic Chemistry* 47, (**2008)**, 1727-1752.

[23]   Sala, X.; Maji, S.; Bofill, R.; García-Antón, J.; Escriche, L.; Llobet, A. *Accounts of Chemical Research* 47, (**2014)**, 504-516.

[24]   Shafirovich, V. Y.; Shilov, A. E. *Journal Name: Kinet. Catal. (USSR) (Engl. Transl.); (United States); Journal Volume: 20:5; Other Information: Translated from Kinet. Katal.; 20: No. 5, 1156-1162(Sep 1979)*, (**1979)**, Medium: X; Size: Pages: 950-955.

[25]   Luneva, N. P.; Knerelman, E. I.; Shafirovich, V. Y.; Shilov, A. E. *Journal of the Chemical Society, Chemical Communications*, (**1987)**, 1504-1505.

[26]   Okuno, Y.; Yonemitsu, O.; Chiba, Y. *Chemistry Letters* 12, (**1983)**, 815-818.

[27]   Jiao, F.; Frei, H. *Chemical Communications* 46, (**2010)**, 2920-2922.

[28]   Najafpour, M. M.; Ehrenberg, T.; Wiechen, M.; Kurz, P. *Angewandte Chemie International Edition* 49, (**2010)**, 2233-2237.

[29]   Limburg, J.; Vrettos, J. S.; Liable-Sands, L. M.; Rheingold, A. L.; Crabtree, R. H.; Brudvig, G. W. *Science* 283, (**1999)**, 1524-1527.

[30]   Limburg, J.; Vrettos, J. S.; Chen, H.; de Paula, J. C.; Crabtree, R. H.; Brudvig, G. W. *Journal of the American Chemical Society* 123, (**2001)**, 423-430.

[31]   Tagore, R.; Crabtree, R. H.; Brudvig, G. W. *Inorganic Chemistry* 47, (**2008)**, 1815-1823.

[32]   Chen; Tagore, R.; Olack, G.; Vrettos, J. S.; Weng, T.-C.; Penner-Hahn, J.; Crabtree, R. H.; Brudvig, G. W. *Inorganic Chemistry* 46, (**2007)**, 34-43.

[33]   Limburg, B.; Bouwman, E.; Bonnet, S. *Coordination Chemistry Reviews* 256, (**2012)**, 1451-1467.

[34]   Chen, H.; Faller, J. W.; Crabtree, R. H.; Brudvig, G. W. *Journal of the American Chemical Society* 126, (**2004)**, 7345-7349.

[35]   Yagi, M.; Narita, K. *Journal of the American Chemical Society* 126, (**2004)**, 8084-8085.

[36]   Kurz, P. *Dalton Transactions*, (**2009)**, 6103-6108.

[37]   Kiwi, J.; Grätzel, M. *Angewandte Chemie International Edition in English* 18, (**1979)**, 624-626.

[38]   Kalyanasundaram, K.; Grätzel, M. *Angewandte Chemie International Edition in English* 18, (**1979)**, 701-702.

[39]   Kiwi, J.; Borgarello, E.; Pelizzetti, E.; Visca, M.; Grätzel, M. *Angewandte Chemie International Edition in English* 19, (**1980)**, 646-648.

[40]   Lewerenz, H. J.; Stucki, S.; Kötz, R. *Surface Science* 126, (**1983)**, 463-468.

[41]   Kötz, R.; Stucki, S. *Electrochimica Acta* 31, (**1986)**, 1311-1316.

[42]   Danilovic, N.; Subbaraman, R.; Chang, K. C.; Chang, S. H.; Kang, Y.; Snyder, J.; Paulikas, A. P.; Strmcnik, D.; Kim, Y. T.; Myers, D.; Stamenkovic, V. R.; Markovic, N. M. *Angewandte Chemie International Edition* 53, (**2014)**, 14016-14021.

[43]   Gersten, S. W.; Samuels, G. J.; Meyer, T. J. *Journal of the American Chemical Society* 104, (**1982)**, 4029-4030.

[44]   Sens, C.; Romero, I.; Rodríguez, M.; Llobet, A.; Parella, T.; Benet-Buchholz, J. *Journal of the American Chemical Society* 126, (**2004)**, 7798-7799.

[45]   Wada, T.; Tsuge, K.; Tanaka, K. *Angewandte Chemie International Edition* 39, (**2000)**, 1479-1482.

[46]   Wada, T.; Tsuge, K.; Tanaka, K. *Inorganic Chemistry* 40, (**2000)**, 329-337.

[47]   Chronister, C. W.; Binstead, R. A.; Ni, J.; Meyer, T. J. *Inorganic Chemistry* 36, (**1997)**, 3814-3815.

[48]   Zong, R.; Thummel, R. P. *Journal of the American Chemical Society* 127, (**2005)**, 12802-12803.

[49]   Concepcion, J. J.; Jurss, J. W.; Templeton, J. L.; Meyer, T. J. *Journal of the American Chemical Society* 130, (**2008)**, 16462-16463.

[50]   Concepcion, J. J.; Tsai, M.-K.; Muckerman, J. T.; Meyer, T. J. *Journal of the American Chemical Society* 132, (**2010)**, 1545-1557.

[51]   Concepcion, J. J.; Jurss, J. W.; Norris, M. R.; Chen, Z.; Templeton, J. L.; Meyer, T. J. *Inorganic Chemistry* 49, (**2010)**, 1277-1279.

[52] Chen, Z.; Concepcion, J. J.; Hu, X.; Yang, W.; Hoertz, P. G.; Meyer, T. J. *Proceedings of the National Academy of Sciences* 107, (**2010**), 7225-7229.

[53] Dutta, P. K.; Das, S. K. *Journal of the American Chemical Society* 119, (**1997**), 4311-4312.

[54] Locatelli, F.; Didillon, B.; Uzio, D.; Niccolai, G.; Candy, J. P.; Basset, J. M. *Journal of Catalysis* 193, (**2000**), 154-160.

[55] Hara, M.; Lean, J. T.; Mallouk, T. E. *Chemistry of Materials* 13, (**2001**), 4668-4675.

[56] Kaschak, D. M.; Mallouk, T. E. *Journal of the American Chemical Society* 118, (**1996**), 4222-4223.

[57] Kerimo, J.; Adams, D. M.; Barbara, P. F.; Kaschak, D. M.; Mallouk, T. E. *The Journal of Physical Chemistry B* 102, (**1998**), 9451-9460.

[58] Hara, M.; Waraksa, C. C.; Lean, J. T.; Lewis, B. A.; Mallouk, T. E. *The Journal of Physical Chemistry A* 104, (**2000**), 5275-5280.

[59] Hoertz, P. G.; Kim, Y.-I.; Youngblood, W. J.; Mallouk, T. E. *The Journal of Physical Chemistry B* 111, (**2007**), 6845-6856.

[60] Morris, N. D.; Suzuki, M.; Mallouk, T. E. *The Journal of Physical Chemistry A* 108, (**2004**), 9115-9119.

[61] Youngblood, W. J.; Lee, S.-H. A.; Kobayashi, Y.; Hernandez-Pagan, E. A.; Hoertz, P. G.; Moore, T. A.; Moore, A. L.; Gust, D.; Mallouk, T. E. *Journal of the American Chemical Society* 131, (**2009**), 926-927.

[62] Mirbagheri, N.; Chevallier, J.; Kibsgaard, J.; Besenbacher, F.; Ferapontova, E. E. *ChemPhysChem* 15, (**2014**), 2844-2850.

[63] Yagi, M.; Tomita, E.; Sakita, S.; Kuwabara, T.; Nagai, K. *The Journal of Physical Chemistry B* 109, (**2005**), 21489-21491.

[64] Chuang, M.-C.; Ho, J.-a. A. *RSC Advances* 2, (**2012**), 4092-4096.

[65] Nakagawa, T.; Beasley, C. A.; Murray, R. W. *The Journal of Physical Chemistry C* 113, (**2009**), 12958-12961.

[66] Michaux, K. E.; Murray, R. W. *Langmuir* 29, (**2013**), 12254-12258.

[67] Hsiao, H.-Y.; Chuang, M.-C. *Electrochimica Acta* 137, (**2014**), 190-196.

[68] McDaniel, N. D.; Coughlin, F. J.; Tinker, L. L.; Bernhard, S. *Journal of the American Chemical Society* 130, (**2008**), 210-217.

[69] Schley, N. D.; Blakemore, J. D.; Subbaiyan, N. K.; Incarvito, C. D.; D'Souza, F.; Crabtree, R. H.; Brudvig, G. W. *Journal of the American Chemical Society* 133, (**2011**), 10473-10481.

[70] Hintermair, U.; Hashmi, S. M.; Elimelech, M.; Crabtree, R. H. *Journal of the American Chemical Society* 134, (**2012**), 9785-9795.

[71] Savini, A.; Belanzoni, P.; Bellachioma, G.; Zuccaccia, C.; Zuccaccia, D.; Macchioni, A. *Green Chemistry* 13, (**2011**), 3360-3374.

[72] Hull, J. F.; Balcells, D.; Blakemore, J. D.; Incarvito, C. D.; Eisenstein, O.; Brudvig, G. W.; Crabtree, R. H. *Journal of the American Chemical Society* 131, (**2009**), 8730-8731.

[73] Blakemore, J. D.; Schley, N. D.; Balcells, D.; Hull, J. F.; Olack, G. W.; Incarvito, C. D.; Eisenstein, O.; Brudvig, G. W.; Crabtree, R. H. *Journal of the American Chemical Society* 132, (**2010**), 16017-16029.

[74] Blakemore, J. D.; Schley, N. D.; Olack, G. W.; Incarvito, C. D.; Brudvig, G. W.; Crabtree, R. H. *Chemical Science* 2, (**2011**), 94-98.

[75] Blakemore, J. D.; Mara, M. W.; Kushner-Lenhoff, M. N.; Schley, N. D.; Konezny, S. J.; Rivalta, I.; Negre, C. F. A.; Snoeberger, R. C.; Kokhan, O.; Huang, J.; Stickrath, A.; Tran, L. A.; Parr, M. L.; Chen, L. X.; Tiede, D. M.; Batista, V. S.; Crabtree, R. H.; Brudvig, G. W. *Inorganic Chemistry* 52, (**2013**), 1860-1871.

[76] Blakemore, J. D.; Schley, N. D.; Kushner-Lenhoff, M. N.; Winter, A. M.; D'Souza, F.; Crabtree, R. H.; Brudvig, G. W. *Inorganic Chemistry* 51, (**2012**), 7749-7763.

[77] Graeupner, J.; Brewster, T. P.; Blakemore, J. D.; Schley, N. D.; Thomsen, J. M.; Brudvig, G. W.; Hazari, N.; Crabtree, R. H. *Organometallics* 31, (**2012**), 7158-7164.

[78] Savini, A.; Bellachioma, G.; Ciancaleoni, G.; Zuccaccia, C.; Zuccaccia, D.; Macchioni, A. *Chemical Communications* 46, (**2010**), 9218-9219.

[79] Savini, A.; Bucci, A.; Bellachioma, G.; Giancola, S.; Palomba, F.; Rocchigiani, L.; Rossi, A.; Suriani, M.; Zuccaccia, C.; Macchioni, A. *Journal of Organometallic Chemistry* 771, (**2014**), 24-32.

[80] DePasquale, J.; Nieto, I.; Reuther, L. E.; Herbst-Gervasoni, C. J.; Paul, J. J.; Mochalin, V.; Zeller, M.; Thomas, C. M.; Addison, A. W.; Papish, E. T. *Inorganic Chemistry* 52, (**2013**), 9175-9183.

[81]   Thomsen, J. M.; Huang, D. L.; Crabtree, R. H.; Brudvig, G. W. *Dalton Transactions* 44, (**2015**), 12452-12472.

[82]   Hintermair, U.; Sheehan, S. W.; Parent, A. R.; Ess, D. H.; Richens, D. T.; Vaccaro, P. H.; Brudvig, G. W.; Crabtree, R. H. *Journal of the American Chemical Society* 135, (**2013**), 10837-10851.

[83]   Sheehan, S. W.; Thomsen, J. M.; Hintermair, U.; Crabtree, R. H.; Brudvig, G. W.; Schmuttenmaer, C. A. *Nat Commun* 6, (**2015**).

[84]   Kirch, M.; Lehn, J.-M.; Sauvage, J.-P. *Helvetica Chimica Acta* 62, (**1979**), 1345-1384.

[85]   Fontecilla-Camps, J. C.; Volbeda, A.; Cavazza, C.; Nicolet, Y. *Chemical Reviews* 107, (**2007**), 4273-4303.

[86]   Morales-Guio, C. G.; Stern, L.-A.; Hu, X. *Chemical Society Reviews* 43, (**2014**), 6555-6569.

[87]   Zeng, M.; Li, Y. *Journal of Materials Chemistry A* 3, (**2015**), 14942-14962.

[88]   Fletcher, S. *Journal of Solid State Electrochemistry* 13, (**2009**), 537-549.

[89]   Trasatti, S. *Journal of Electroanalytical Chemistry and Interfacial Electrochemistry* 39, (**1972**), 163-184.

[90]   Danilovic, N.; Subbaraman, R.; Strmcnik, D.; Chang, K.-C.; Paulikas, A. P.; Stamenkovic, V. R.; Markovic, N. M. *Angewandte Chemie International Edition* 51, (**2012**), 12495-12498.

[91]   Quaino, P.; Juarez, F.; Santos, E.; Schmickler, W. *Beilstein Journal of Nanotechnology* 5, (**2014**), 846-854.

[92]   Hinnemann, B.; Moses, P. G.; Bonde, J.; Jørgensen, K. P.; Nielsen, J. H.; Horch, S.; Chorkendorff, I.; Nørskov, J. K. *Journal of the American Chemical Society* 127, (**2005**), 5308-5309.

[93]   Greeley, J.; Jaramillo, T. F.; Bonde, J.; Chorkendorff, I.; Norskov, J. K. *Nat Mater* 5, (**2006**), 909-913.

[94]   Chen, J.; Lim, B.; Lee, E. P.; Xia, Y. *Nano Today* 4, (**2009**), 81-95.

[95]   Xu, Y.; Zhang, B. *Chemical Society Reviews* 43, (**2014**), 2439-2450.

[96]   Zhang, J.; Li, C. M. *Chemical Society Reviews* 41, (**2012**), 7016-7031.

[97]   Esposito, D. V.; Chen, J. G. *Energy & Environmental Science* 4, (**2011**), 3900-3912.

[98]   Bodner, M.; Hofer, A.; Hacker, V. *Wiley Interdisciplinary Reviews: Energy and Environment* 4, (**2015**), 365-381.

[99]   Rommal, H. E. G.; Morgan, P. J. *Journal of the Electrochemical Society* 135, (**1988)**, 343-346.

[100]   Soares, D. M.; Teschke, O.; Torriani, I. *Journal of the Electrochemical Society* 139, (**1992**), 98-105.

[101]   Los, P.; Rami, A.; Lasia, A. *Journal of Applied Electrochemistry* 23, (**1993**), 135-140.

[102]   Raj, I. A.; Vasu, K. I. *Journal of Applied Electrochemistry* 20, (**1990**), 32-38.

[103]   Conway, B. E.; Bai, L. *International Journal of Hydrogen Energy* 11, (**1986**), 533-540.

[104]   Jakšić, J. M.; Vojnović, M. V.; Krstajić, N. V. *Electrochimica Acta* 45, (**2000**), 4151-4158.

[105]   Brown, D. E.; Mahmood, M. N.; Man, M. C. M.; Turner, A. K. *Electrochimica Acta* 29, (**1984)**, 1551-1556.

[106]   Fan, C.; Piron, D. L.; Sleb, A.; Paradis, P. *Journal of the Electrochemical Society* 141, (**1994)**, 382-387.

[107]   Navarro-Flores, E.; Chong, Z.; Omanovic, S. *Journal of Molecular Catalysis A: Chemical* 226, (**2005)**, 179-197.

[108]   Hatay, I.; Su, B.; Li, F.; Partovi-Nia, R.; Vrubel, H.; Hu, X.; Ersoz, M.; Girault, H. H. *Angewandte Chemie International Edition* 48, (**2009)**, 5139-5142.

[109]   Su, B.; Hatay, I.; Ge, P. Y.; Mendez, M.; Corminboeuf, C.; Samec, Z.; Ersoz, M.; Girault, H. H. *Chemical Communications* 46, (**2010)**, 2918-2919.

[110]   Hatay, I.; Ge, P. Y.; Vrubel, H.; Hu, X.; Girault, H. H. *Energy & Environmental Science* 4, (**2011)**, 4246-4251.

[111]   Nieminen, J. J.; Hatay, I.; Ge, P.; Mendez, M. A.; Murtomaki, L.; Girault, H. H. *Chemical Communications* 47, (**2011)**, 5548-5550.

[112]   Mendez, M. A.; Partovi-Nia, R.; Hatay, I.; Su, B.; Ge, P.; Olaya, A.; Younan, N.; Hojeij, M.; Girault, H. H. *Physical Chemistry Chemical Physics* 12, (**2010)**, 15163-15171.

[113]   Ge, P.; Scanlon, M. D.; Peljo, P.; Bian, X.; Vubrel, H.; O'Neill, A.; Coleman, J. N.; Cantoni, M.; Hu, X.; Kontturi, K.; Liu, B.; Girault, H. H. *Chemical Communications* 48, (**2012)**, 6484-6486.

[114] Scanlon, M. D.; Bian, X.; Vrubel, H.; Amstutz, V.; Schenk, K.; Hu, X.; Liu, B.; Girault, H. H. *Physical Chemistry Chemical Physics* 15, (**2013**), 2847-2857.

[115] Bian, X.; Scanlon, M. D.; Wang, S.; Liao, L.; Tang, Y.; Liu, B.; Girault, H. H. *Chemical Science* 4, (**2013**), 3432-3441.

[116] Ge, P.; Todorova, T. K.; Patir, I. H.; Olaya, A. J.; Vrubel, H.; Mendez, M.; Hu, X.; Corminboeuf, C.; Girault, H. H. *Proceedings of the National Academy of Sciences* 109, (**2012**), 11558-11563.

[117] Ge, P.; Olaya, A. J.; Scanlon, M. D.; Hatay Patir, I.; Vrubel, H.; Girault, H. H. *ChemPhysChem* 14, (**2013**), 2308-2316.

[118] Rivier, L.; Stockmann, T. J.; Méndez, M. A.; Scanlon, M. D.; Peljo, P.; Opallo, M.; Girault, H. H. *The Journal of Physical Chemistry C* 119, (**2015**), 25761-25769.

[119] Ariga, K.; Yamauchi, Y.; Rydzek, G.; Ji, Q.; Yonamine, Y.; Wu, K. C. W.; Hill, J. P. *Chemistry Letters* 43, (**2014**), 36-68.

[120] Iost, R. M.; Crespilho, F. N. *Biosensors and Bioelectronics* 31, (**2012**), 1-10.

[121] Zhao, W.; Xu, J.-J.; Chen, H.-Y. *Electroanalysis* 18, (**2006**), 1737-1748.

[122] Jomaa, H. W.; Schlenoff, J. B. *Langmuir* 21, (**2005**), 8081-8084.

[123] Huguenin, F.; Gonzalez, E. R.; Oliveira, O. N. *The Journal of Physical Chemistry B* 109, (**2005**), 12837-12844.

[124] Zhang, M.; Yan, Y.; Gong, K.; Mao, L.; Guo, Z.; Chen, Y. *Langmuir* 20, (**2004**), 8781-8785.

[125] Ariga, K.; Hill, J. P.; Ji, Q. *Physical Chemistry Chemical Physics* 9, (**2007**), 2319-2340.

[126] Iler, R. K. *Journal of Colloid and Interface Science* 21, (**1966**), 569-594.

[127] Decher, G.; Hong, J.-D. *Makromolekulare Chemie. Macromolecular Symposia* 46, (**1991**), 321-327.

[128] Decher, G.; Hong, J. D.; Schmitt, J. *Thin Solid Films* 210–211, Part 2, (**1992**), 831-835.

[129] Kleinfeld, E. R.; Ferguson, G. S. *Science* 265, (**1994**), 370-373.

[130] Lvov, Y.; Ariga, K.; Ichinose, I.; Kunitake, T. *Langmuir* 12, (**1996**), 3038-3044.

[131] Hojeij, M.; Su, B.; Tan, S.; Mériguet, G.; Girault, H. H. *ACS Nano* 2, (**2008**), 984-992.

[132] Kotov, N. A.; Dekany, I.; Fendler, J. H. *The Journal of Physical Chemistry* 99, (**1995)**, 13065-13069.

[133] Cassagneau, T.; Mallouk, T. E.; Fendler, J. H. *Journal of the American Chemical Society* 120, (**1998)**, 7848-7859.

[134] Ko, Y.; Baek, H.; Kim, Y.; Yoon, M.; Cho, J. *ACS Nano* 7, (**2013)**, 143-153.

[135] Dhar, J.; Patil, S. *ACS Applied Materials & Interfaces* 4, (**2012)**, 1803-1812.

[136] Lvov, Y.; Ariga, K.; Ichinose, I.; Kunitake, T. *Journal of the American Chemical Society* 117, (**1995)**, 6117-6123.

[137] Godman, N. P.; DeLuca, J. L.; McCollum, S. R.; Schmidtke, D. W.; Glatzhofer, D. T. *Langmuir* 32, (**2016)**, 3541-3551.

[138] Ma, H.; Hu, N.; Rusling, J. F. *Langmuir* 16, (**2000)**, 4969-4975.

[139] He, J.-A.; Samuelson, L.; Li, L.; Kumar, J.; Tripathy, S. K. *Langmuir* 14, (**1998)**, 1674-1679.

[140] Caruso, F.; Möhwald, H. *Journal of the American Chemical Society* 121, (**1999)**, 6039-6046.

[141] Decher, G. In *Multilayer Thin Films*; Wiley-VCH Verlag GmbH & Co. KGaA: 2003, p 1-46.

[142] Kondo, T.; Uosaki, K. *Journal of Photochemistry and Photobiology C: Photochemistry Reviews* 8, (**2007)**, 1-17.

[143] Rydzek, G.; Ji, Q.; Li, M.; Schaaf, P.; Hill, J. P.; Boulmedais, F.; Ariga, K. *Nano Today* 10, (**2015)**, 138-167.

[144] Decher, G. *Science* 277, (**1997)**, 1232-1237.

[145] Laurent, D.; Schlenoff, J. B. *Langmuir* 13, (**1997)**, 1552-1557.

[146] Stockton, W. B.; Rubner, M. F. *Macromolecules* 30, (**1997)**, 2717-2725.

[147] Wang, L.; Wang, Z.; Zhang, X.; Shen, J.; Chi, L.; Fuchs, H. *Macromolecular Rapid Communications* 18, (**1997)**, 509-514.

[148] Bergbreiter, D. E.; Liao, K.-S. *Soft Matter* 5, (**2009)**, 23-28.

[149] Schmitt, J.; Decher, G.; Dressick, W. J.; Brandow, S. L.; Geer, R. E.; Shashidhar, R.; Calvert, J. M. *Advanced Materials* 9, (**1997)**, 61-65.

[150] Ferreyra, N.; Coche-Guerente, L.; Fatisson, J.; Lopez Teijelo, M.; Labbe, P. *Chemical Communications*, (**2003)**, 2056-2057.

[151] Lahav, M.; Shipway, A. N.; Willner, I.; Nielsen, M. B.; Stoddart, J. F. *Journal of Electroanalytical Chemistry* 482, (**2000)**, 217-221.

[152] Lahav, M.; Heleg-Shabtai, V.; Wasserman, J.; Katz, E.; Willner, I.; Dürr, H.; Hu, Y.-Z.; Bossmann, S. H. *Journal of the American Chemical Society* 122, (**2000)**, 11480-11487.

[153] Hojeij, M.; Eugster, N.; Su, B.; Girault, H. H. *Langmuir* 22, (**2006)**, 10652-10658.

[154] Cheng, Y.; Corn, R. M. *The Journal of Physical Chemistry B* 103, (**1999)**, 8726-8731.

[155] Cheng, Y.; Murtomäki, L.; Corn, R. M. *Journal of Electroanalytical Chemistry* 483, (**2000)**, 88-94.

Chapter 2

Layer-by-Layer Deposition of Iridium Oxide on FTO

_____

2.1   Introduction

Iridium oxide nanoparticles (IrO_x NPs) exhibit high electrocatalytic activity towards water oxidation reaction (WOR), at moderate overpotentials (0.20 – 0.29 V)[1-6], and stability against anodic corrosion over a wide pH range, whether incorporated into electrochemical or photo-electrochemical systems.[7,8]. The scarcity of Ir and the enhanced activity of nanoscale (higher surface-to-volume ratio)[9] *versus* bulk heterogeneous catalysts or solid IrO_x electrodes promotes the use of IrO_x as NPs, typically studied as colloidal solutions or films on various electrode surfaces.

The design of immobilization strategies to prepare stable, electrocatalytic high-surface area amorphous IrO_x NP films that *(i)* maximize the surface coverage of electroactive catalytic IrO_x centers and *(ii)* simultaneously retain the properties of individual (as opposed to aggregated) NPs, are key to the development of modified electrodes capable of promoting the WOR at low

overpotentials with high Faradaic efficiencies. Pre-formed IrO_x NPs from colloidal solutions have been attached to indium tin oxide (ITO),[1,10-12] fluorinated tin oxide (FTO),[3,13] gold,[1,13,14] platinum (Pt),[1,14] glassy carbon (GC),[1,4,5,13,14] hematite[15] and spectroscopic graphite (Gr)[6] electrodes by chemisorption,[16] physisorption, [6] electroflocculation by either controlled potential amperometry (CPA)[1,14] or dual-potential pulsed amperometry (DPPA),[5] anodic electrodeposition,[3,11,17] electrophoresis[15] and electrostatic interactions[4] Additionally, IrO_x NP films have been generated *in situ* by anodic electrolysis of $[Ir(OH)_6]^{2-}$ solutions[13]

Importantly, different IrO_x NP film formation strategies using the same colloid solutions affect *(i)* the electrocatalytic properties and *(ii)* the stability of the films formed post-deposition on an electrode surface. Ferapontova and co-workers immobilized water-capped $IrO_x \cdot nH_2O$ NPs on graphite electrodes by both electrochemical deposition and physisorption[6]. Their study revealed that the electrochemically deposited IrO_x NP films exhibited a higher stability and activity than those physisorbed. Murray and co-workers originally developed an electroflocculation approach where the electrode is biased at potentials where the water oxidation reaction takes place[1,14]. As a result, a significant amount of protons are produced at the electrode surface and cause the precipitation of hydroxyl-capped IrO_x NPs. Meanwhile, the copious O_2 evolved during electroflocculation induced mesoporosity in the resulting adherent films. Chuang and co-workers revisited electroflocculation with the premise of using DPPA, the purpose of which was to intermittently reduce evolved O_2 during electroflocculation to minimize the amount of gas at the electrode surface and promote adhesion of the IrO_x NPs.[5] This change in electrochemical technique not only improved film stability but also changed the physical morphology (minimizing aggregation) and chemical composition of the films, thus altering the kinetics of the WOR and also serving as an excellent example of the powerful influence of immobilization strategy when designing efficient electrodes.

In this chapter, we describe an alternative immobilization methodology to prepare IrO_x NP films on FTO as WOR electrodes by layer-by-layer (LbL) deposition of alternate layers of oppositely charged

poly(diallyldimethylammonium chloride) (PDDA) polymer and citrate stabilized IrO_x NPs on the electrode surface. This flexible approach allowed us to finely tune the number of electroactive iridium centers by incorporating additional layers, producing stable, amorphous IrO_x NP films containing well-dispersed catalytic NPs. Furthermore, the use of stabilized particles allows us to obtain an electrochemical response which resembles the highly reversible waves observed in hydrous iridium oxide films (HIROFs), differing from the more irreversible behavior obtained in flocculated films. This behavior, which remains across the whole pH scale, is mainly attributed to the effect of the capping agent, which ensures that the number of electroactive sites remains approximately the same by avoiding the strong interaction between individual centers.

2.2   Materials and methods

2.2.1 Chemicals

All chemicals were used as received without further purification. Potassium hexachloroiridate (K_2IrCl6, 99.99%), tri-sodium citrate dihydrate ($\geq$99.0), poly(diallydimethylammonium chloride) (PDDA, 20%, Mw 200,000 – 350,000) and perchloric acid ($HClO_4$, 70%) were purchased from Aldrich. All aqueous solutions were prepared with ultrapure water (Millipore Milli-Q, specific resistivity 18.2 MΩ•cm). Pure O_2 (medical grade) cylinders were purchased from Carbagas.

2.2.2 Synthesis IrO_x NPs

Colloidal citrate stabilized IrO_x NPs were synthesized as described by Mallouk and co-workers.[7, 10] 0.0300 g of K_2IrCl_6 ($6.20\cdot10^{-5}$ mol) and 0.0547 g of tri-sodium citrate dihydrate ($1.86\cdot10^{-4}$ mol) were dissolved in 50 mL of de-ionized water. The pH of this solution was adjusted to approximately 7.5 with 0.25 M NaOH. This brown solution was then transferred to a 100 mL round

bottomed flask with a reflux condenser attached and heated at 95 °C in an oil bath. After 30 minutes the round-bottomed flask was removed from the oil bath and the solution allowed to cool down to room temperature. The pH of this solution was precisely adjusted to 7.5 with 0.25 M NaOH. The heating at 95 °C for 30 minutes followed by addition of NaOH was repeated until the pH stabilized at 7.5. The solution was heated at 95 °C for a further 2 hours with O_2 bubbling throughout. Finally, the colloidal IrO_x NP solution was cooled to room temperature and dialyzed in deionized water using Spectra/Pore 7 membranes with molecular weight cut-offs (MWCO) of 1 kDa. The dialysis was performed over a 24-hour period and the water changed at least four times. Post-dialysis, the colloidal solution was diluted to a total volume of 100 mL giving 0.62 mM of colloidal citrate stabilized IrO_x NPs.

2.2.3 Layer-by-layer deposition of IrO_x NPs films on FTO electrodes

Prior to deposition, the FTO slides (15 Ω/sq., 2.2 mm thickness, Solaronix) were cleaned by sequential washing with acetone, sonication in a base bath (1 M KOH in an ethanol/water mixture (8:2)) for 20 minutes, rinsing with water, immersion in 1 M H_2SO_4 for 15 minutes and, finally, treatment with O_2 plasma for 15 minutes. In order to ensure reproducibility, the LbL deposition was controlled by a custom dip-coating robot with an arm capable of movement in an arc, as well as up-and-down in the *z*-direction perpendicular to the table (see Figure 2.1).

The LbL deposition sequence began by immersing the cleaned FTO electrode for 15 minutes in a solution containing the cationic polymer PDDA (4.76 % w/v) in 0.4 M NaCl. Next, the electrode was rinsed twice with water and subsequently immersed in a 0.62 mM solution of colloidal citrate stabilized IrO_x NPs for 30 minutes. Finally, the IrO_x/PDDA-modified FTO electrode was rinsed twice in deionized water and allowed to air dry. The desired number of IrO_x/PDDA bilayers were obtained by repeating the sequence the necessary number of times.
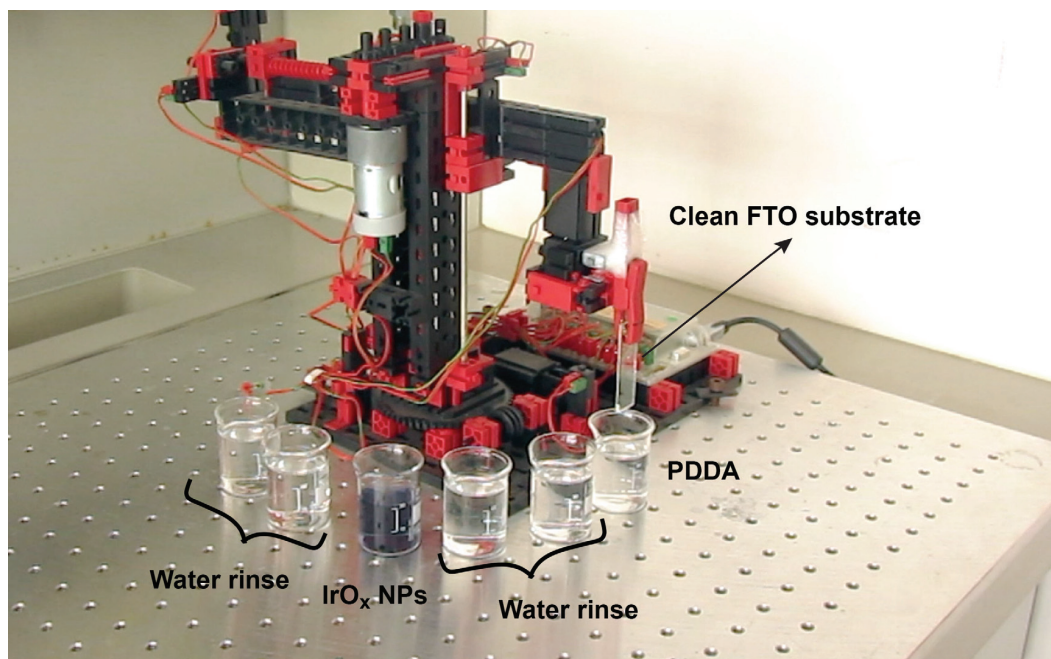
Figure 2.1 Setup used for the layer-by-layer deposition of IrO$_x$ -PDDA bilayers

2.2.4 Characterization methods

The as-synthesized colloidal IrO$_x$ NPs were characterized by UV/vis spectroscopy, transmission electron microscopy, X-ray diffraction (XRD), and X-ray photoelectron microscopy (XPS). The UV-Vis spectrum was obtained using an Ocean Optics USB 4000 optic fiber spectrophotometer. TEM images were recorded using a CM12 (Philips) transmission electron microscope, operating with a LaB$_6$ electron source at 120 kV. The samples were deposited onto a TEM grid from a solution prepared by mixing an equal volume of the IrO$_x$ NP solution and ethanol. The X-Ray diffraction measurements were obtained using a Bruker D8 X-ray diffractometer (UK), operating with a Cu Kα X-ray source at 40 kV, and 40 mA. For this experiment the sample of IrO$_x$ was pre-concentrated to approx. 50 mM by using a rotaevaporator, deposited on the surface of a substrate, allowed to dry with nitrogen stream, and finally dried under vacuum.

The IrO$_x$/PDDA-modified FTO electrodes were also analyzed by high-resolution scanning electron microscopy (HR SEM) using a SEM MERLIN composed of a GEMINI II column (Zeiss). As discussed *vide infra*, prior to UV/vis measurements the IrO$_x$/PDDA-modified FTO electrodes were pre-treated by polarization at 0.635 *vs.*

SHE (*i.e.,* 0.425 V *vs.* Ag/AgCl (3 M NaCl)) for 90s. Spectro-electrochemical characterization of the IrO_x/PDDA-modified FTO electrodes was performed in a three-electrode configuration using a PGSTAT 30 potentiostat (Metrohm, CH). No *iR* compensation was applied to the cell and all voltammetry experiments were carried out under aerobic conditions at an ambient temperature of 23 ± 2 °C.
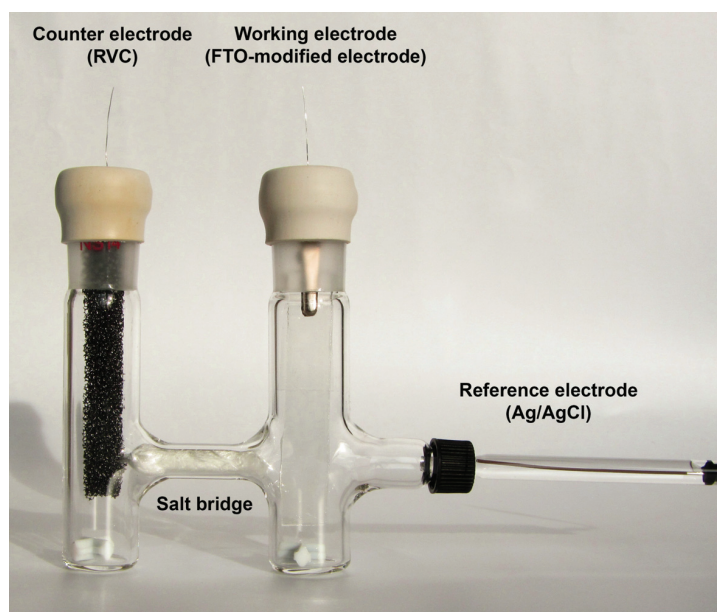

Figure 2.2 Gas-tight bulk electrolysis cell used for electrocatalytic O_2 generation and quantification during IrO_x/PDDA bilayer stability and Faradaic efficiency experiments.

Bulk electrolysis experiments were carried out in aqueous solutions containing either 0.1 M $HClO_4$ (pH 1), 0.5 M phosphate buffer (pH 7) or 0.1 M NaOH (pH 13). A classic bulk electrolysis cell configuration (Figure 2.2) was employed using an IrO_x/PDDA-modified FTO electrode with 14 IrO_x/PDDA bilayers as the working electrode, Duocel® reticulated vitreous carbon (RVC, pores/inch = 30; relative density 3%, supplied by ERG Aerospace Corporation, U.S.A.) as the counter electrode and Ag/AgCl (3 M NaCl) as the reference electrode. All the potentials were converted into the standard hydrogen electrode scale (SHE) by adding the potential value of the Ag/AgCl in the SHE scale (0.210 V). The anodic and cathodic compartments were separated by a glass wool plug to prevent re-oxidation of O_2 at the RVC counter electrode. O_2 measurements were carried out with a FOXY fluorescent O_2 sensor from Ocean Optics. Prior to O_2 measurements, the electrolysis cell was sonicated for approximately 20 s. This permitted any O_2 bubbles generated, but

trapped, at the IrO_x/PDDA-modified FTO electrode surface to migrate to the headspace.

Then, the FOXY probe was inserted through a septum into the headspace of the working electrode compartment. In each case the amounts of O_2 dissolved in solution were considered negligible and not considered in the calculations.

For practical reasons bulk electrolysis experiments were performed under aerobic conditions. Thus, in order to determine the amounts of O_2 evolved in moles during bulk electrolysis ($\eta_{O_2(evolved)}$), it was neccesary to calculate the total number of moles of O_2 present at the beginning ($\eta_{O_2(initial)}$) and at the end ($\eta_{O_2(final)}$) of each experiment. $\eta_{O_2(initial)}$ was calculated from the ideal gas equation, taking into account that the initial gas in the head space contains 20.9 % O_2:

$$\eta_{O_2(initial)} = \left(\frac{P_{atm} \times V_{HS}}{R \times T} \right) \times 0.209 \qquad (2.1)$$

where P_{atm} is the atmospheric pressure, V_{HS} is the volume of the head space, T is the room temperature and R the gas constant. $\eta_{O_2(final)}$ was calculated as follows:

$$\eta_{O_2(final)} = \left(\frac{\%O_2}{100 - \%O_2} \right) \left(\frac{P_{atm} \times V_{HS}}{R \times T} \right) (1 - 0.209) \qquad (2.2)$$

Therefore,

$$\eta_{O_2(evolved)} = \eta_{O_2(final)} - \eta_{O_2(initial)} \qquad (2.3)$$

Finally, the Faradaic efficiency (*%Eff*) can be calculated as the ratio between experimental number of moles obtained in the equation (2.3) and theoretical number of moles given by the Faraday's law:

$$\%Eff = 100 \cdot \left(\frac{\eta_{O_2 \text{(evolved)}}}{Q / nF} \right) \qquad (2.4)$$

where Q is the charge passed during bulk electrolysis , n is the numer of moles electrons needed to produce one mole of O_2, and F is the Faraday's constant.

2.3   Results and discussion

2.3.1 Characterization of the IrO_x NPs

Figure 2.3 shows the UV-visible spectrum of the IrO_x colloids prepared by the method previously described. The absorbance spectrum exhibits an intense UV absorbance below 400 nm, a broad band with an absorbance maximum at 590 nm that extends into the near-IR, and a non-zero baseline beyond 700 nm, presumably as a result of light scattering.

Hoertz and coworkers reported that the absorption properties of the surfactant-stabilized IrO_x colloids are a function of the size and the aggregation degree of the particles, which in turns depends on the synthesis conditions (*e.g.,* capping agent, temperature, and time)[18]. For instance, small and non-aggregated particles (~2nm) obtained with malonate as capping agent, exhibit narrower peak at 564 nm in comparison to that obtained with citrate (λ_{max} = 585 nm), where the particles are significantly larger (>10nm). Interestingly, the TEM images obtained with the citrate-stabilized colloids (Figure 2.4) reveal that those aggregates are composed of even smaller NPs (2nm), most likely due to the interaction of the individual centers through the third carboxylate group oriented away from the IrO_x surface. The UV-Vis spectrums as well as the TEM images are in good agreement with previous reports and have been used as criteria of quality along Chapters 2, 4, and 5. Finally, the

amorphous character of the IrOx solids was corroborated by the X-Ray diffraction measurements (Figure 2.5) where only broad bumps were observed.
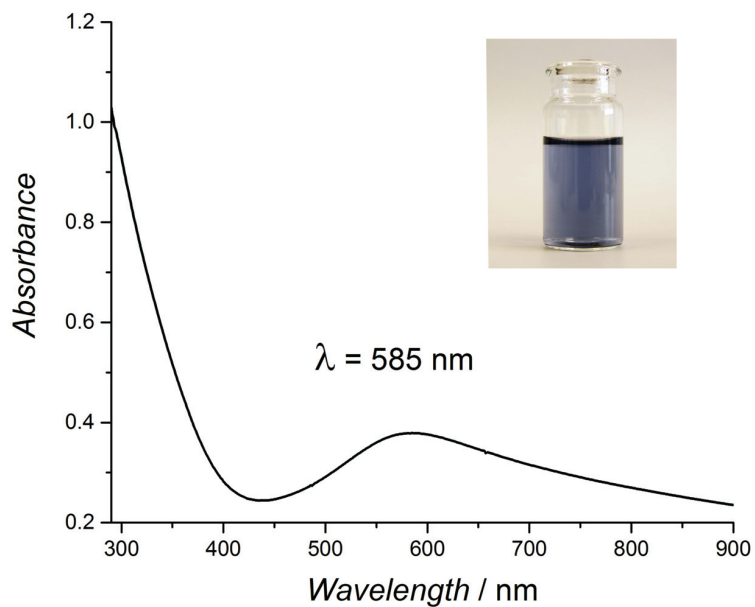

Figure 2.3 UV/vis absorbance spectra of IrO$_x$ NPs stabilized with citrate. A cell containing the blue colloid is shown in the inset.
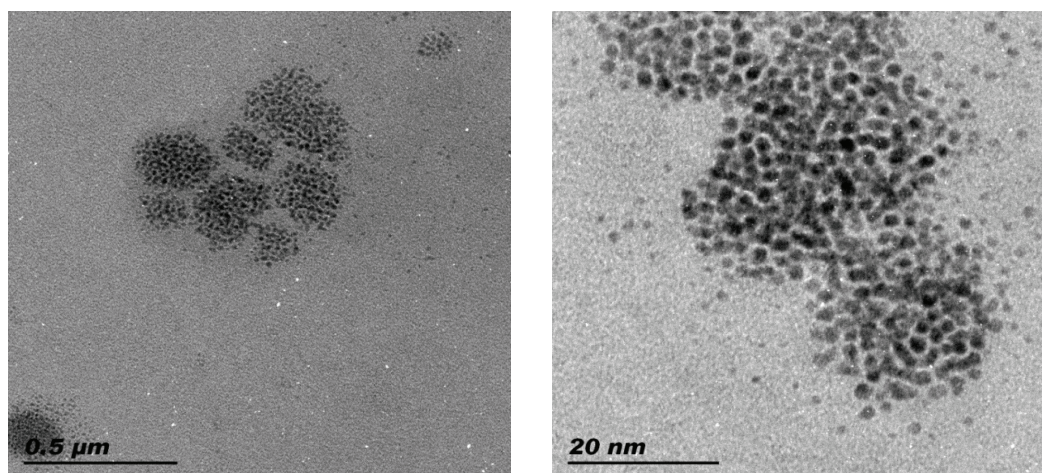

Figure 2.4 TEM images of citrate stabilized IrO$_x$ NPs at two different magnifications.
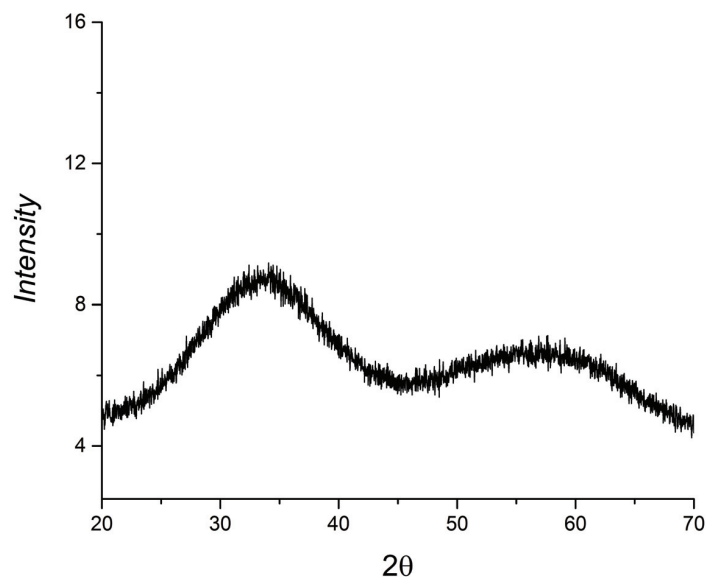
Figure 2. 5 X-ray diffraction patterns of citrate stabilized IrO_x NPs

2.3.2 Morphology of the LbL deposited IrO_x NP films

High-resolution SEM images revealed that the FTO electrode surface was coated in an amorphous tissue-like structure upon deposition of 14 IrO_x/PDDA-bilayers with uniform distribution of the IrO_x NPs across the film (white spots, 10 – 20 nm in size; see Figures 2.6 A & B). Direct comparison with SEM images of an unmodified FTO electrode clearly demonstrates that the contours of the LbL film follow the morphology of the underlying FTO surface (Figures 2.6 C & D). The observation of these IrO_x NPs in 10 – 20 nm clusters is fully consistent with both our TEM images of the as-prepared colloidal IrO_x NP solution herein (Figure 2.4), and previous observations by Hoertz *et al*[18] as discussed above.

As no larger aggregates were observed by SEM in the LbL IrO_x/PDDA-films, we can conclude that the present method provides an efficient route to prepare tailored (in terms of surface coverage of electrocatalytic NPs in particular, discussed *vide infra*) NP films on an electrode surface that are free of aggregation. Furthermore, IrO_x/PDDA-modified FTO electrodes were subjected to prolonged sonication in ethanol-water to induce the removal of some of the NP film. TEM images of these solutions (Figure 2.7) revealed the presence of individual 2 nm NPs supporting the fact that the IrO_x clusters retain their original size and shapes post-LbL deposition.
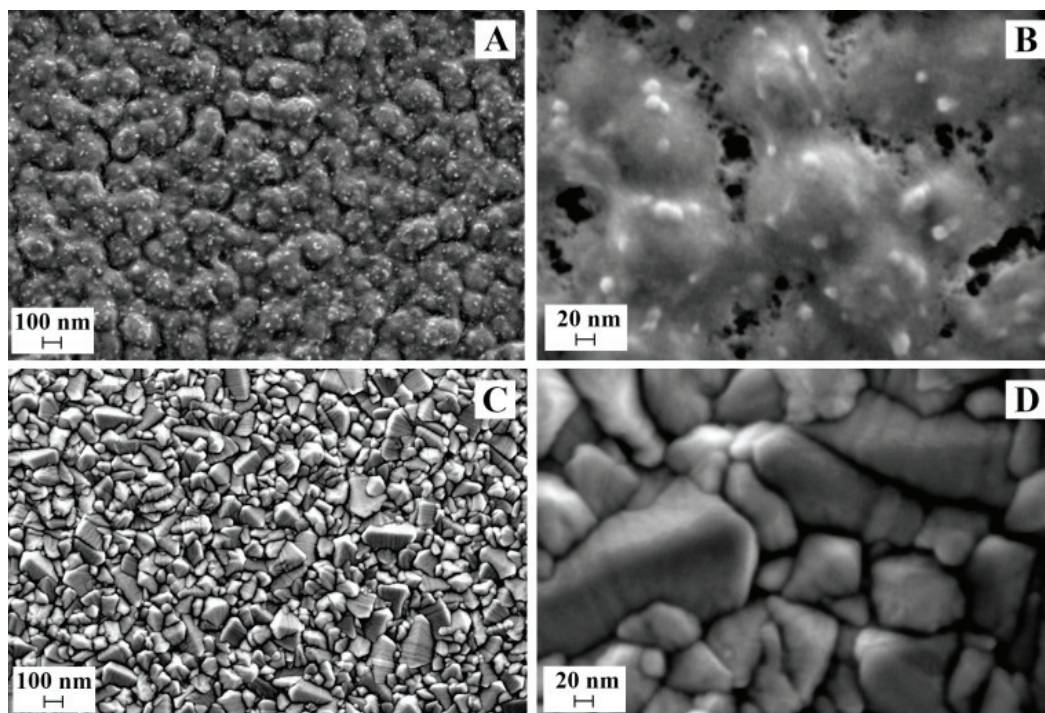
Figure 2.6 (A, B) SEM images at two different magnifications of the surface morphology of an FTO electrode modified using the layer-by-layer (LbL) methodology with 14 IrO_x/PDDA-bilayers. **(C, D)** For comparison, SEM images at the same magnifications of the bare FTO electrode are shown.
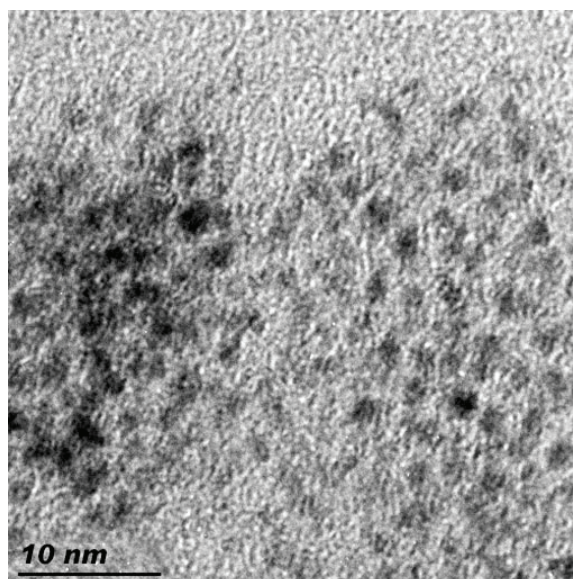

Figure 2.7 TEM images the residue obtained after sonicating an FTO electrode modified with 14 IrO_x/PDDA bilayers for 4 hours in ethanol.

2.3.3 Spectro-electrochemistry of LbL deposited IrO$_x$ NP films on FTO electrodes

Cyclic voltammetry (CV) of an IrO$_x$-modified FTO electrode consisting of 10 IrO$_x$/PDDA-bilayers in phosphate buffered solution (pH 7) is presented in Figure 2.8 A. The response (black CV curve), dominated by two reversible redox couples at ~ 0.40 V and ~ 0.72 V *vs.* SHE, is in sharp contrast to the essentially featureless CV of the bare FTO electrode (red CV curve) under otherwise identical experimental conditions. The CV response of the IrO$_x$/PDDA-bilayers strongly resembles that previously reported for hydrous iridium oxide films (HIROFs).[19-29]
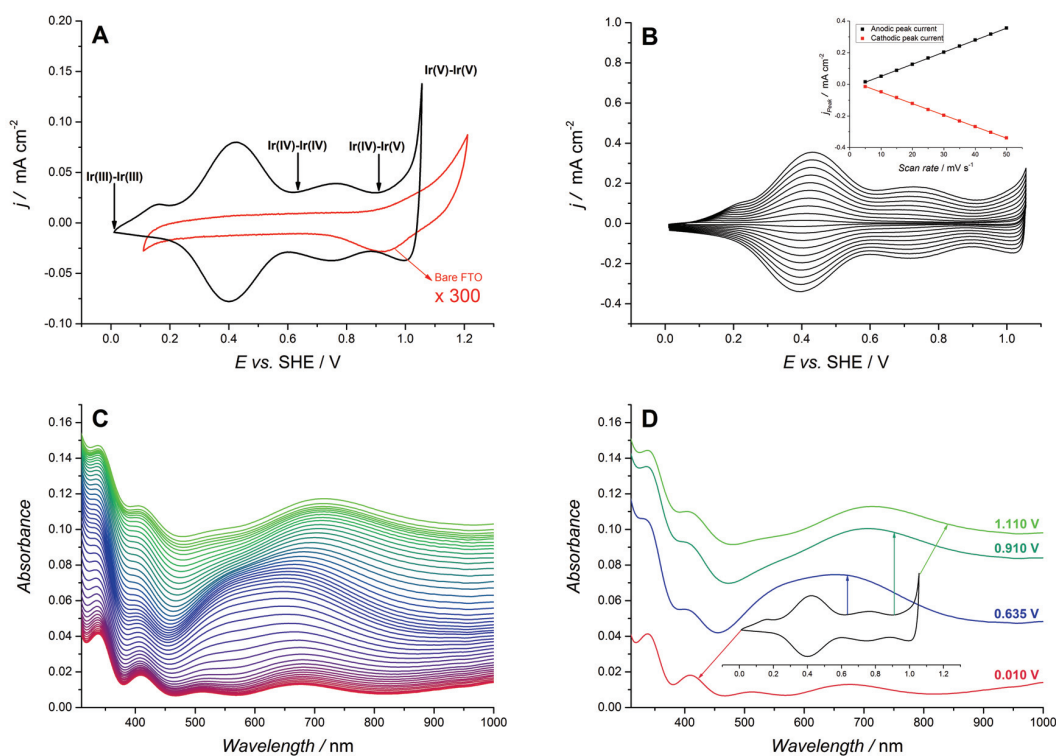
Figure 2.8 Spectro-electrochemistry of the IrO$_x$/PDDA bilayer modified FTO electrodes. (A) Comparison of the CV responses of a bare FTO electrode (red CV curve, magnified 300 times) and an FTO electrode modified with 10 IrO$_x$/PDDA bilayers by LbL assembly (black CV curve). Scan rate used was 10 mV·s^{-1}. **(B)** Scan rate study of an FTO electrode modified with 8 IrO$_x$/PDDA bilayers. Scan rates used: 5, 10, 15, 20, 25, 30, 35, 40, 45 and 50 mV·s^{-1}. Inset: Linear dependence of the Ir(III)/Ir(IV) peak current density (mA·cm^{-2}) *vs.* the scan rate (mV·s^{-1}). **(C)** Series of UV/vis spectra obtained at an FTO electrode modified with 14 IrO$_x$/PDDA bilayers after a pre-treatment step that involved applying potentials over the range 0.010 – 1.110 V (from bottom to top) for 90 s *via* chronoamperometry in 25 mV steps. **(D)** Representative UV/vis spectra at selected applied potentials highlighting the measured red shifts in the UV/vis spectra as the IrO$_x$ NPs in the IrO$_x$/PDDA bilayers were gradually oxidized at higher potentials. All CV data was obtained in 0.5 M phosphate buffer solution (pH 7).

The two reversible redox couples are commonly attributed to the Ir(III)/Ir(IV) and Ir(IV)/Ir(V) transitions, respectively, reflecting the multiple redox states available for the IrO$_x$ centers. Interestingly, the electrochemical response strikingly contrasts with the one observed in flocculated films where the charge associated to the transformation between Ir(III)/Ir(IV) is higher than the one assigned to Ir(IV)/Ir(V).

This unusual behavior, which is not explained in detail, reflects the different nature of the processes happening in the film obtained under such conditions.[1,14] In this sense, the deposits obtained with stabilized particles exhibit a more ideal behavior, where the electron transfer occurs in a reversible manner. This reflects also the ability of the film to easily incorporate the anions required to compensate the change in the charge inside the film. Other features related to the CVs obtained herein are that (i) the charge associated with the second oxidation peak is lower than that of the first peak and (ii) the second peak appears broader.

Previously, for HIROFs, the ratio between the charge associated with the first (Ir(III)/Ir(IV)) and second (Ir(IV)/Ir(V)) peaks has been found to be dependent on the pH, the composition and the concentration of the electrolyte, but always remains less than 1.[23,29] This behaviour has been interpreted as the full oxidation of all IrO$_x$ centers present from Ir(III) to Ir(IV) at $\sim$ 0.40 V, followed by only partial oxidation of the Ir(IV) centers formed to Ir(V). Thus, during the Ir(III)/Ir(IV) transition, two Ir(III) centers, termed Ir(III)-Ir(III), with adsorbed water molecules, *i.e.,* Ir(III)-H$_2$O, are oxidized to two Ir(IV) centers, Ir(IV)-Ir(IV), with adsorbed hydroxyl-groups, *i.e.,* Ir(IV)-OH. Subsequently, these two Ir(IV) centers may undergo full oxidation, forming an Ir(V)-Ir(V) intermediate with double-bonded oxygen-groups attached, *i.e.,* Ir(V)=O. In practice, the latter partial oxidation of the surface hydroxyl-groups is observed and attributed to ensemble effects that suppress the likelihood of two adjacent Ir(V)=O moieties on the electrode surface. Additionally, these lateral repulsive interactions can also dictate the shape of the oxidation peaks and may be a contributory factor to the broadening of the Ir(IV)/Ir(V) peak. Several other factors may also lead to the observed peak broadening including a distribution of formal potentials in the LbL film[30] or coupled ion-electron transfer processes.[31]

Finally, as the potential applied is increased beyond 0.95 V, the surface coverage of Ir(V) increases to the extent that the conditions for the formation of O–O are reached and molecular oxygen (O$_2$) is released as a product of the electrocatalytic

reaction. The cathodic peak at ~0.95 V (*vs.* SHE) is attributed to the reduction of unconsumed Ir(V) species, giving a rough estimate of the Ir(IV)/Ir(V) redox potential.[1]

The effect of scan rate on the voltammetric peak current of the Ir(III)/Ir(IV) transition of an IrO$_x$-modified FTO electrode consisting of eight IrO$_x$/PDDA-bilayers in phosphate buffered solution (pH 7) is presented in Figure 2.8 B. Both the anodic and cathodic peak current densities exhibited a linear relationship with the scan rate up to 50 mV·s^{-1}, indicating that electron transfer from the IrO$_x$ centers to the electrode surface is a diffusion independent surface-controlled process in this scan rate range.

Interpretation of the CV data *vide supra* allows us to identify the required applied potentials necessary to generate either predominantly Ir(III)-Ir(III), Ir(IV)-Ir(IV), Ir(IV)-Ir(V) or Ir(V)-Ir(V) species in the LbL films. This precise control over the oxidation states of the IrO$_x$ centers permits the use of spectroelectrochemistry to match the UV/vis spectroscopic response with the degree of oxidation of the LbL film (Figures 2.8 C). As discussed below, this is essential to accurately determine the surface coverage of IrO$_x$ NPs in the film by UV/vis spectroscopy. Potential step amperometry was used with applied potentials over the range 0.010 – 1.110 V (*vs.* SHE) for 90 s in 25 mV steps to an FTO electrode modified with 14 IrO$_x$/PDDA-bilayers and the UV/vis spectra were recorded at each applied potential (Figure 2.8 C). At more positive applied potentials (> 0.600 V *vs.* SHE) these spectra were strikingly different from that observed for the colloidal IrO$_x$ NPs solution (Figure 2.3). The latter are reported to consist of equimolar proportions of Ir(III) and Ir(IV).[18] However, as clearly illustrated in Figure 2.8 D, with successively more oxidizing potentials applied to the FTO electrode a shift to the red is observed and attributed to the generation of a mixture of Ir(IV) and Ir(V) species in the LbL film.

2.3.4 Optical and electrochemical determination of the IrO$_x$ NP surface coverage as a function of the number of bilayers deposited

FTO electrodes modified with 14 IrO$_x$/PDDA-bilayers appear a light blue color when freshly modified. However, visual inspection reveals that these electrodes turn colorless after "aging" in ambient aerobic conditions for 5 days (Figure 2.9). This

"aging" process whereby the IrO$_x$ NPs are slowly reduced by reaction perhaps with water trapped inside the film, substantially modifies the observed UV/vis spectra in comparison to a freshly modified electrode. Thus, in order to accurately compare several FTO electrodes modified with different numbers of bilayers by LbL on different days, each electrode was subjected to a pre-treatment step prior to UV/vis characterization. The latter involved the application of an applied potential of 0.635 V *vs*. SHE, so just after the first Ir(III)/Ir(IV) redox process, for 90 s to produce an IrO$_x$/PDDA-film of predominately Ir(IV) centers. The application of this potential visually oxidized the IrO$_x$ NP films back to a deeper blue colour and "normalized" the UV/vis responses of all modified electrodes in terms of the oxidation states of the IrO$_x$ NPs therein. A comparison of these normalized UV/vis spectra as a function of the number of IrO$_x$/PDDA-bilayers deposited is presented in Figure 2.10A. Furthermore, a plot of absorbance *vs*. the number of bilayers in Figure 2.10 D (black curve) is linear indicating the reproducible adhesion of each successive bilayer.
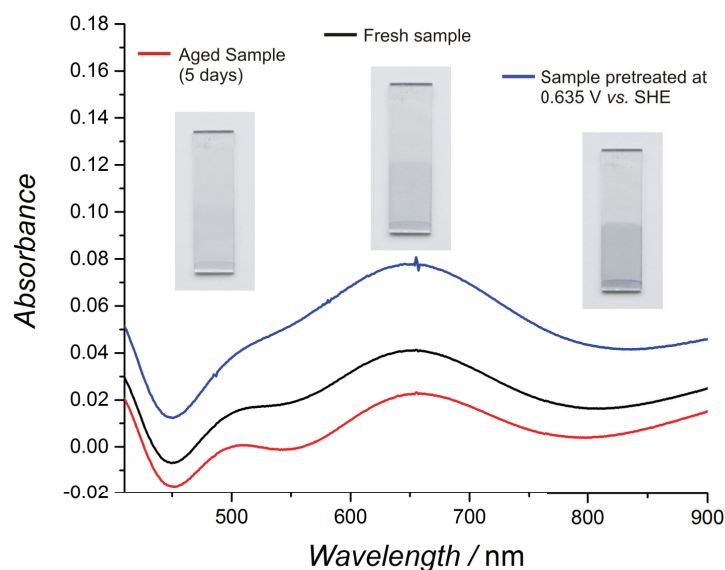
Figure 2.9 UV/Vis spectra obtained from an FTO electrode modified with 14 IrO$_x$/PDDA bilayers immediately after the synthesis (black line), after 5 days of "aging" (blue line), and after pretreatment by application of a potential of 0.635 V *vs*. SHE for 90 s *via* chronoamperometry in 0.5 M phosphate buffer solution (pH 7).

Further qualitative evidence of the "aging" of the IrO$_x$/PDDA-bilayers on the electrode surface upon storage in ambient conditions was provided by monitoring the open circuit potentials (OCPs) of the IrO$_x$/PDDA-bilayer modified electrodes with

time. The precise values of the OCP measured in phosphate buffered solution (pH 7) varied slightly (± 20 mV) between individually modified electrodes, but the trends in the shifts of OCP with time were universal. For all electrodes monitored, the value of the OCP substantially decreased (to more negative potentials) with aging, again in line with the reduction of the IrO_x NPs therein. This was especially evident for the thicker LbL-films (8 - 14 IrO_x/PDDA-bilayers) with 70 – 100 mV shifts after 5 days. In the thinner LbL films (2 - 4 IrO_x/PDDA-bilayers) the variation of the OCP was less pronounced (10 – 50 mV after 5 days).
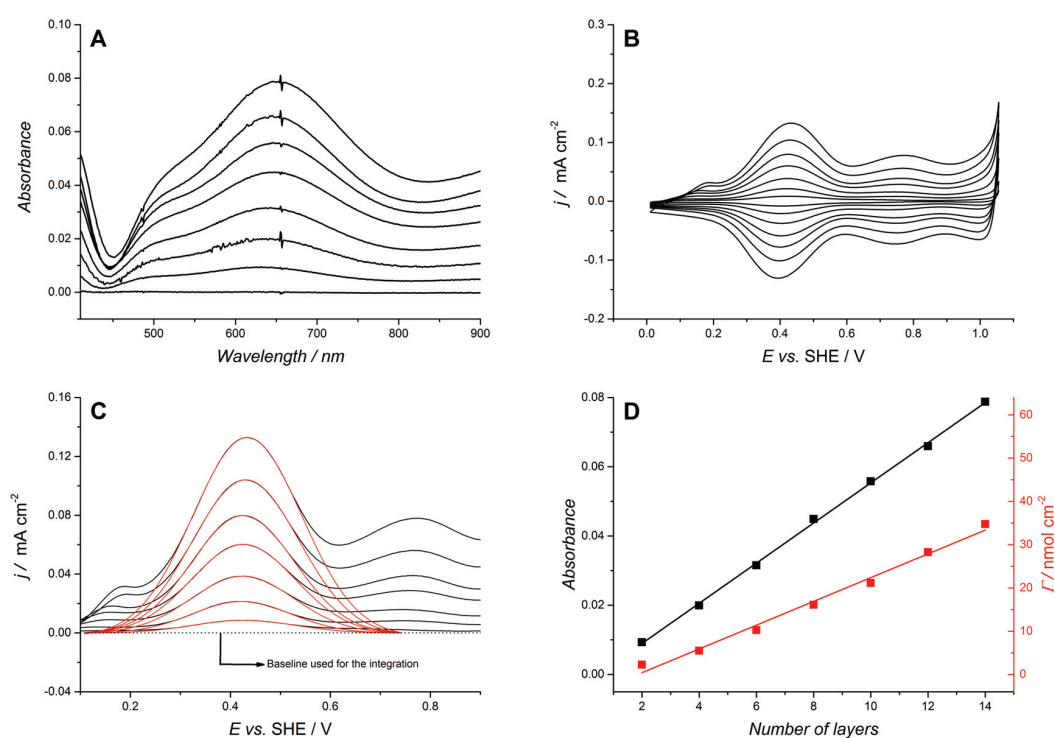
Figure 2.10 Surface coverage determination of the total and "electrochemically active" IrO_x NPs present on the FTO electrode surface with increasing number of IrO_x/PDDA bilayers deposited using the LbL approach. (A) UV/vis spectra of FTO electrodes modified with increasing numbers of IrO_x/PDDA bilayers; 2, 4, 6, 8, 10, 12 and 14 from bottom to top. Prior to acquisition, each IrO_x/PDDA bilayer modified FTO electrode was pre-treated by applying 0.635 V (*vs.* SHE) for 90 s using chronoamperometry. In this manner the IrO_x NPs on each modified FTO electrode uniformly contained predominately Ir(IV), as detailed in the text, allowing accurate comparison of separate electrodes by UV/vis spectroscopy. **(B)** CV of the FTO electrodes with increasing numbers of IrO_x/PDDA bilayers as described in (A). **(C)** Fitting of the Ir(III)/Ir(IV) anodic peak using Gaussian fit functions to integrate the charge (Q / C) used to determine the surface coverage of electrochemically active IrO_x NPs on the FTO electrodes (Γ / nmol cm^{-2}) with increasing numbers of IrO_x/PDDA bilayers. **(D)** UV/vis peak absorbance (measured at λ_{max} = 650 nm; red squares) and Ir(III)/Ir(IV) surface coverage (black squares) with increasing numbers of IrO_x/PDDA bilayers on the FTO electrode surface.

Although UV/vis spectroscopy provides a qualitative measure of the linear increase in the number of IrO$_x$ NPs present on the modified FTO electrodes with each successive bilayer (indicating reproducible adhesion), it does not verify if all IrO$_x$ NPs present are electrochemically addressable, *i.e.,* the IrO$_x$ NPs in the outermost layer are functional and in electrochemical communication with the underlying FTO electrode surface. The latter is a key factor when preparing electrodes containing relatively scarce materials such as Ir. A comparison of the electrochemical responses in phosphate buffered solution (pH 7) of a series of IrO$_x$/PDDA-bilayer modified electrodes with between 2 and 14 bilayers is shown in Figure 2.10 B.

Precise determination of the surface coverage (Γ) of the electrochemically active IrO$_x$ NPs present was achieved by integrating the charge (Q) under the Ir(III)/Ir(IV) anodic peak at 0.2 V using Gaussian fit functions (see Figure 2.10 C) and applying the equation $\Gamma = Q/nFA$. An assumption was made that each IrO$_x$ center transferred one electron, *i.e., n* = 1. As clearly shown in Figure 2.10 D, the surface coverage increased linearly with successive bilayers, mirroring the linear increase in absorbance noted by UV/vis spectroscopy, and confirming that at the scan rate implemented (10 mV·s^{-1}) all of the IrO$_x$ centers were electrochemically addressable.

To complete this picture, CVs of the modified electrodes were recorded using lower scan rates and scanned to higher upper potentials (Figure 2.11 A). The lower scan rates favor a lower ohmic drop, which becomes more important at potentials where the WOR takes place. Figure 2.11 B depicts the current value in the positive scan at an overpotential of 300 mV (compared to the thermodinamic potential for the WOR at pH 7, 0.817 V *vs*. SHE) represented as a function of the number of IrO$_x$/PDDA-bilayers. The observed trend exhibits a saturation-like behavior, with a linear increase of the current density until approximately 10 IrO$_x$/PDDA-bilayers are deposited LbL. Subsequently, the current density remains approximately constant upon the addition of further bilayers.

This saturation-like behavior contrasts with the monotonous linear increase observed in Figure 2.10 D, where the activity of the film was measured as the charge passed during the transformation of Ir(III) to Ir(IV). As the potential becomes higher than $\approx$ 1 V, a significant amount of Ir(V) centers are formed with the subsequent release of O$_2$ and protons. At this potential, diffusion controlled processes are involved, namely ingress of water to the film and egress of protons and O$_2$ molecules

from the film. Thus, as the film becomes thicker, it would seem that after 10 bilayers the rate of the WOR reaches a saturation limit. Potentially, beyond 10 IrO_x/PDDA-bilayers diffusion of protons, O_2 and water molecules through the film may to an extent be inhibited, acting as one cause of the observed saturation-like behaviour. A second possible cause is the potential drop within the film; while the inner layers are at a potential close to that of the electrode, the outer layers may be at lower potentials due to the iR drop within the film.
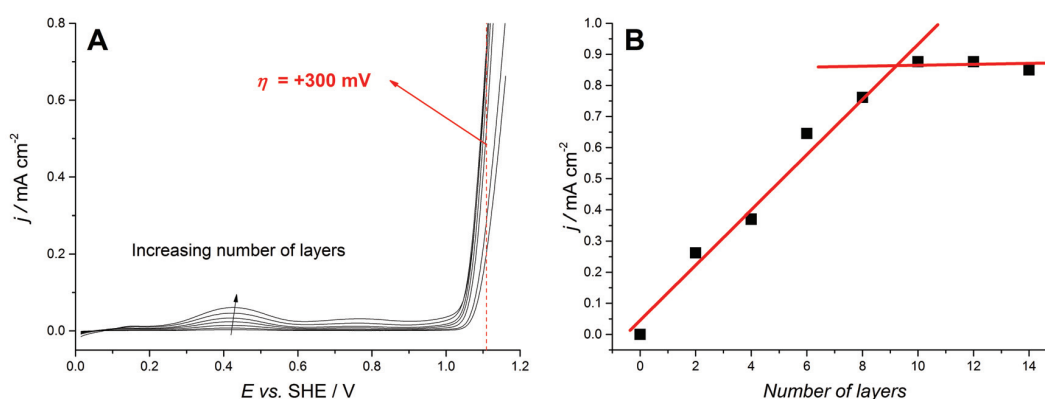
Figure 2.11 Electrochemistry of the FTO modified electrodes at a potential where the WOR takes place. (A) CVs of the FTO electrodes with increasing numbers of IrO_x/PDDA bilayers. (B) Current density on the positive scan at η = 300 mV *vs.* the thermodynamic potential for the WOR as a function of the number of IrO_x/PDDA bilayers.

All in all, this LbL methodology provides a route to enhance by at least one order of magnitude the surface coverage of water oxidation catalyst deposited on the surface of the electrode by keeping intact the activity of the individual IrO_x NPs within the film.

2.3.5 Thermodynamic studies: super-Nernstian pH response and WOR overpotentials as a function of pH

FTO electrodes modified with 8 IrO_x/PDDA-bilayers were characterized by CV across the pH range 1 to 13. The resulting voltammograms were plotted in Figure 2.12 A. In agreement with several previous studies on HIROFs,[23,25] and indeed various other metal oxide systems,[32] a super-Nerstian pH dependence (*i.e.,* the potential-pH dependence differs significantly from the expected 59 mV·pH^{-1} predicted by a

Nernstian analysis) was observed with the Ir(III)-Ir(III)/Ir(IV)-Ir(IV) and Ir(IV)-Ir(IV)/Ir(IV)-Ir(V) redox transitions shifting negatively by 76 and 82 mV·pH^{-1} with decreasing acidity, respectively (Figure 2.12 B). In contrast, the onset potential for the WOR at a current of 0.1 mA cm^{-2}, displayed a typical quasi-Nernstian response shifting negatively 55 mV·pH^{-1} with decreasing acidity (Figure 2.12 A, inset). Thus, as the Ir redox transitions shift to more negative potentials to a greater degree than the WOR onset potential as a function of pH, a consequence is the much clearer separation of the Ir(III)/Ir(IV) and Ir(IV)-Ir(IV)/Ir(IV)-Ir(V) redox transitions from the WOR onset potential at neutral or alkaline conditions.
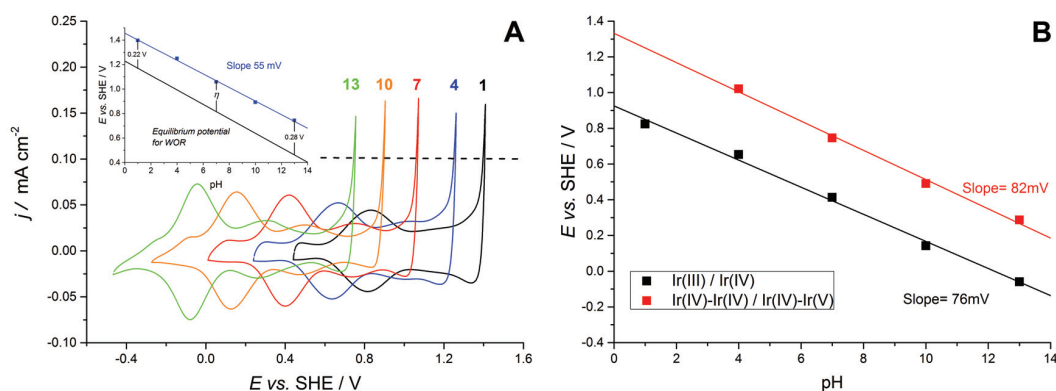
Figure 2.12 Super-Nernstian pH response and WOR onset potentials. (A) CVs of an FTO electrode modified with 8 IrO$_x$/PDDA bilayers measured in aqueous solutions at pH 1 (0.1 M HClO$_4$), 4, 7 and 10 (0.5 M phosphate buffer solutions), and 13 (0.1 M NaOH). The scan rate used was 10 mV·s^{-1}. The inset in (A) highlights the pH dependence of the thermodynamic and experimentally observed onset potentials of the WOR at a current of 0.1 mAcm^{-2}. **(B)** The pH dependence of the potentials associated with the anodic Ir(III)/Ir(IV) (black squares) and cathodic Ir(IV)-Ir(IV)/Ir(IV)-Ir(V) (red squares) redox transitions.

The origin of the super-Nernstian behavior may be explained as follows: the oxidation from Ir(III)-OH$_2$ to Ir(IV)-OH releases one proton and one electron according to the stoichiometry of the reaction. Moreover, as a more oxidized and therefore more acidic center is generated, a fraction of protons is released from the films according to the acid-base equilibrium. Thus, a proton/electron ratio higher than 1 is obtained during the overall transformation from Ir(III) to Ir(IV), resulting in a super-Nernstian dependence of the potential. The same reasoning applies for the second redox process labelled as the Ir(IV)/Ir(IV)/ Ir(IV)-Ir(V). An in-depth mechanistic study on this topic for the LbL-deposited IrO$_x$/PDDA films herein is

beyond the scope of this thesis and the reader is referred to recent mechanistic work by Ahlberg and co-workers in this regard.[28,29]

A comparison of the WOR onset and thermodynamic potentials for water oxidation (inset Figure 2.12 A) highlighted an essentially pH-independent overpotential (η), varying slightly from 0.22 to 0.28 V moving from acidic to alkaline conditions, for IrO_x/PDDA-bilayers FTO electrodes. This value is either lower or comparable to those reported previously for other IrO_x NP-modified electrodes.

Finally, a progressive decrease in the intensity of the Ir(III)/Ir(IV) peak is observed from basic to acidic pH values. However, as the intensity of the peak decreases it concurrently broadens, ultimately rendering a peak with approximately the same charge, and thereby providing the same number of active centers. As previously discussed, the catalytic centers possess acid-base properties, thus changes in the pH necessarily affect the proportion of acid/base species which take part in the charge transfer reaction. As a consequence, at lower pH values a higher proportion of protonated species are present in the film, promoting lateral interactions and therefore broadening of the peaks.

2.3.6 Efficiency towards O_2 evolution and IrO_x/PDDA film stability studies

Bulk electrolysis experiments were carried out with FTO electrodes modified with 14 IrO_x/PDDA-bilayers in 0.1 M $HClO_4$ (pH 1), 0.5 M phosphate buffer (pH 7) and 0.1 M NaOH (pH 13) aqueous solutions. The concentration of the buffer species in solution ensures that the pH as well as the thermodynamic driving force for the WOR remained approximately constant.

During bulk electrolysis the Fermi level of the FTO electrode is controlled by the voltage source, and the Fermi levels of all of the electrochemically addressable IrO_x NPs in the LbL-deposited film shift to that set potential by Fermi level equilibration. In this manner, at each pH condition, an overpotential (η = +400 mV) was applied. As depicted in Figure 2.13, although the Fermi levels of the electrode and IrO_x NPs equilibrate, those of the O_2/H_2O redox couple in solution do not. The latter arises as the kinetics of the rate of discharging the IrO_x NPs, by electron transfer to the

electrode surface facilitated by tunneling of electrons between IrO_x NPs in the film due to the overlapping high densities of states of the metallic oxides,[33] are far superior to the kinetics of charging the IrO_x NPs, *via* the WOR at the surface of each IrO_x NP. Thus, a constant thermodynamic driving force is present that drives electron transfer efficiently to the electrode surface.
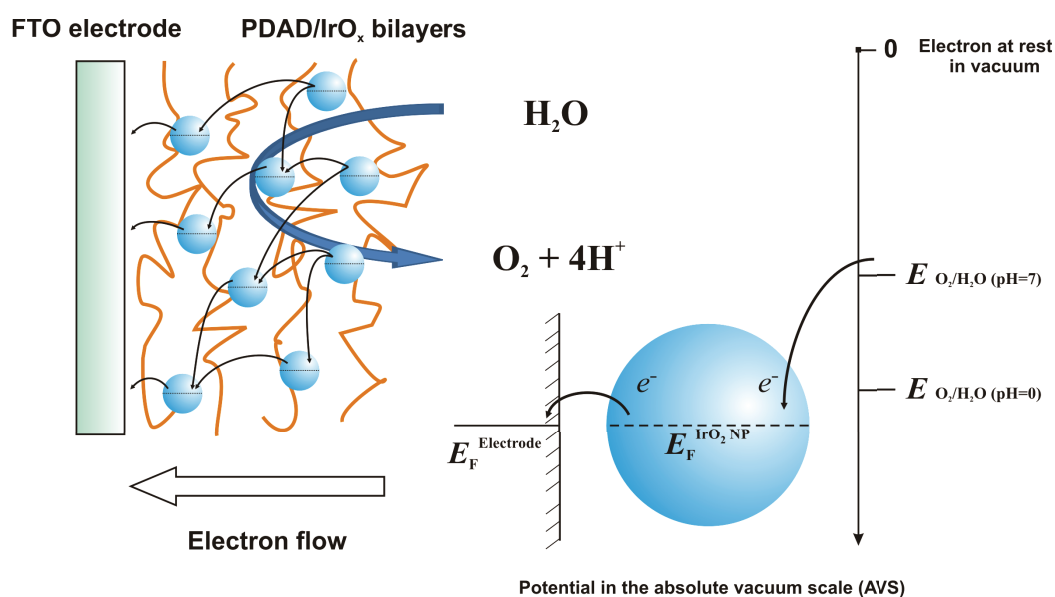
Figure 2.13 Schematic of electron transfer during the WOR for an FTO electrode modified with PDDA/IrO$_x$ bilayers. Electron transfer between the IrO_x centers with the film proceeds *via* a tunneling mechanism through the insulating polymer structure.

A classic bulk electrolysis configuration was utilized (Figure 2.2). These experiments had the dual role of (i) determining the Faradaic efficiency of these IrO_x NP modified electrodes towards O_2 evolution and (ii) determining the stability of the LbL-deposited IrO_x/PDDA bilayers on the FTO electrode surface.

The Faradaic efficiency towards O_2 at each pH studied for FTO electrodes modified with 14 IrO_x/PDDA-bilayers was determined by comparing the actual amounts of O_2 evolved (/ μmol), determined using a FOXY fluorescent O_2 sensor from Ocean Optics, *vs.* the theoretical amounts of O_2 expected based on the quantity of charge passed (Q = 6.85 C for each electrode tested) during bulk electrolysis. Figure 2.14 shows the curves obtained during the oxygen measurement with the FOXY sensor, where t=0 is the instant when the sensor pierces the septum and enter in contact with the headspace of the anodic compartment. The results obtained from the oxygen

measurements are summarized in Table 2.1 and 2.2, and reveal that under acidic and neutral conditions the efficiency of O_2 evolution approaches 100 % within experimental error, but dips below 90 % under alkaline conditions. (For details about the calculations, please see the section section 2.2.4)
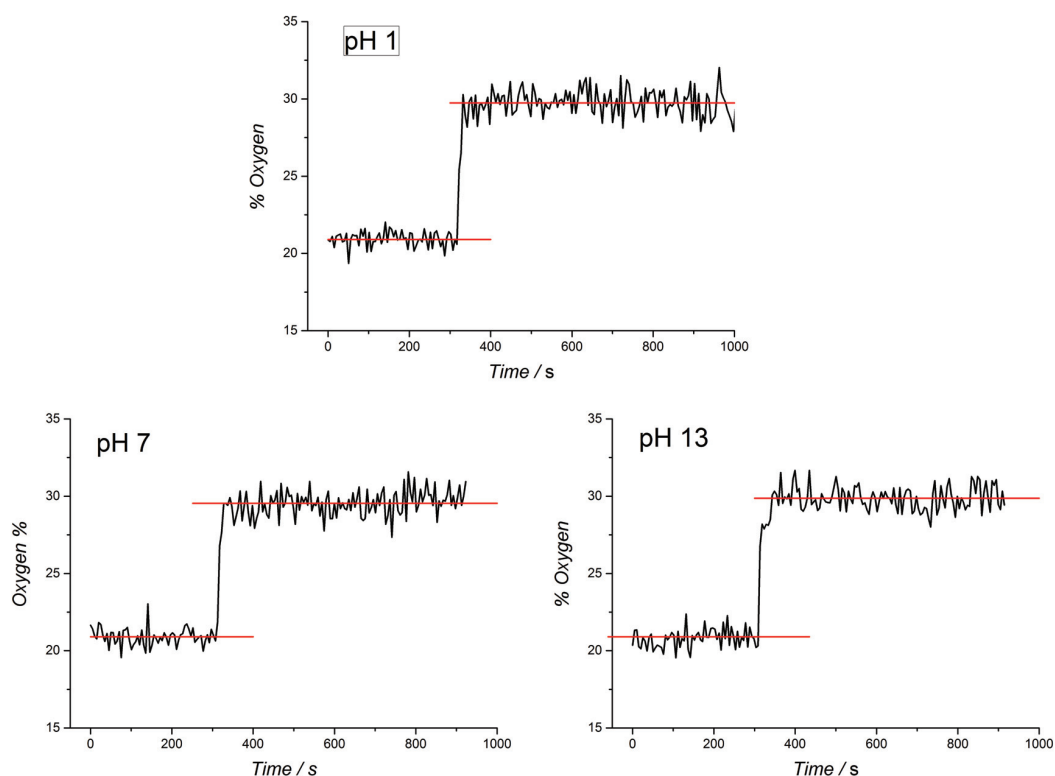
Figure 2.14 O_2 determination was achieved using a FOXY fluorescent O_2 sensor after bulk electrolysis at each pH investigated.

Table 2.1. Summary of the experimentally observed amounts of O_2 evolved ($\eta_{O_2(evolved)}$ / µmol) using a FOXY fluorescent O_2 sensor from an FTO electrode modified with 14 IrO_x/PDDA bilayers after bulk electrolysis experiments carried out in 0.1 M $HClO_4$ (pH = 1), 0.5 M phosphate buffer solution (pH = 7) and 0.1 M NaOH (pH = 13) with applied potentials of 1.57, 1.22 and 0.80 V *vs.* SHE, respectively.

Experimental Conditions	%O_2 measured	Experimentally determined $\eta_{O_2(evolved)}$ / µmol
pH 1	8.98	16.6
pH 7	8.85	17.4
pH 13	9.18	15.6

Table 2.2 Summary of the amounts of O$_2$ evolved ($\eta_{O_2\text{(evolved)}}$ / µmol) determined from Faraday's Law at pH 1, 7, and 13, and determination of the Faradaic efficiency as the ratio of the experimentally measured and theoretically theoretical predicted values of $\eta_{O_2\text{(evolved)}}$.

Experimental Conditions	Charge (Q) / C	Theoretically predicted $\eta_{O_2\text{(evolved)}}$ / µmol	Faradaic efficiency / %
pH 1	6.85	17.7	94
pH 7	6.85	17.7	98
pH 13	6.85	17.7	88

The trends in stability of the IrO$_x$/PDDA modified FTO electrodes towards O$_2$ evolution with pH are clearly evident from voltammetry (Figure 2.15). The measured currents (η = +400 mV) exhibited steady-state behavior during electrolysis (Figures 2.14 A and B), and marginal changes in the CVs taken pre- and post-electrolysis were observed, at pH 1 and pH 7 (Figures 2.15 D and E). Thus, under acidic and neutral conditions the LbL-modified electrodes were robust, exhibiting no meaningful losses in catalytic efficiency during bulk electrolysis. However, at pH 13, the measured current gradually decreased with time (Figure 2.15 C) and the CVs taken pre- and post-electrolysis were substantially different (Figure 2.15 F), both indicative of poor stability in alkaline media. The latter loss of stability may reflect decomposition of the IrO$_x$ NPs, with formation of less reactive species under alkaline conditions, or simply a chemical degradation of the PDDA polymer that binds the IrO$_x$ NPs to the FTO electrode surface. Considering the high stability of IrO$_x$ NPs and their low tendency to corrode in alkaline media,[3] the leaching of the IrO$_x$ NPs from the electrode surface is more likely. Indeed, Stevens and co-workers described that, in the presence of a strong base, quaternary ammonium salts may undergo a 1,2-rearrangement. This reaction, commonly referred to as the Stevens rearrangement,[34-36] results in the formation of a tertiary amine which at basic conditions is neutral. Thus, the electrostatic forces binding the IrO$_x$/PDDA bilayers together weaken or disappear with time under alkaline conditions, leading to a terminal loss of film stability and gradual removal of catalytic IrO$_x$ NPs from the surface of the FTO electrode. This loss of stability under alkaline conditions also explains the lower faradaic efficiencies determined under these conditions (see Table 2.2).
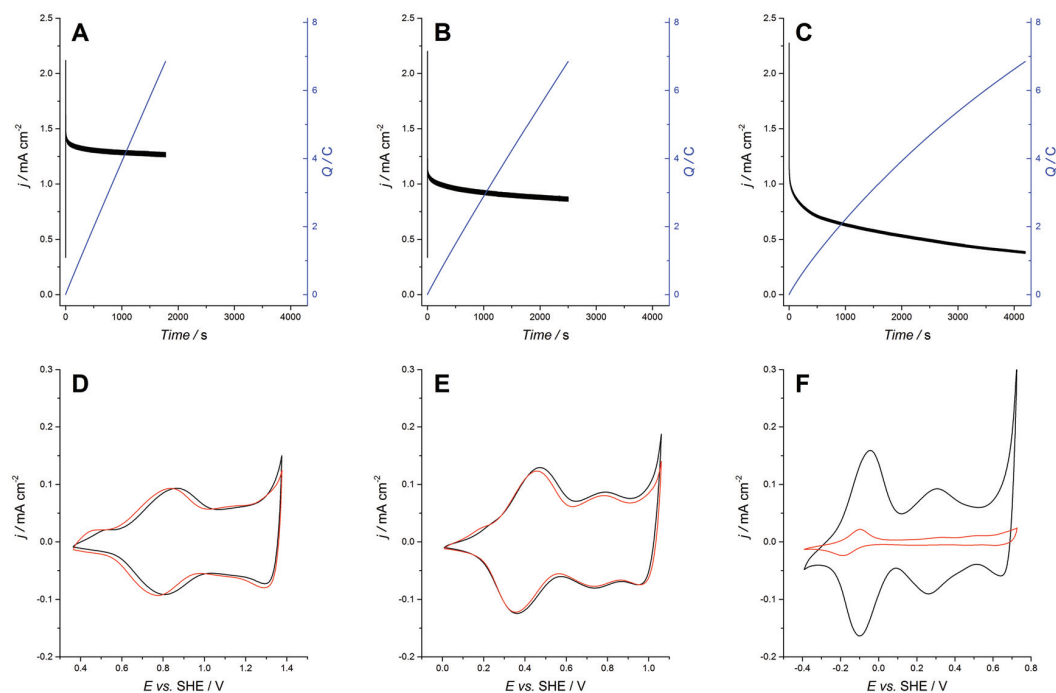
Figure 2.15. **Bulk electrolysis experiments: Efficiency towards O$_2$ evolution and IrO$_x$/PDDA film stability studies. (A - C)** Chronoamperometric plots of the current (black line) and charge (blue line) during water electrolysis using an FTO electrode modified with 14 IrO$_x$/PDDA bilayers in a classic bulk electrolysis cell (see Figure 2.2). In each case an overpotential (η) of +400 mV *vs.* the thermodynamic potential for the WOR was applied to the working electrode. The experiments were carried out in (A) 0.1 M HClO$_4$, (B) 0.5 M phosphate buffer solution (pH 7) and (C) 0.1 M NaOH with applied potentials of 1.57, 1.22 and 0.80 *vs.* SHE, respectively. The non compensated resistance for the three systems measured by impedance spectroscopy was 46 Ω, 48 Ω and 37 Ω respectively. The figures **(D - F)** depict the CVs recorded before (black line) and after (red line) electrolysis for the systems described in (A – C). The scan rate used was 10 mV·s^{-1}.

Additional experiments involved testing the stability of electrode responses at longer times and higher overpotentials to push the electrodes to their working limits. Figure 2.16 A & C shows that at η = +600 mV the catalytic current only decreases by 15% of the initial value after 12 hours of electrolysis under acidic conditions. However, the catalytic current under neutral conditions was seen to degrade under these harsher experimental conditions, Figure 2.16 B & D. Thus, improvements are necessary to stabilize the LbL-deposited IrO$_x$ NP films at all pH values, but especially under alkaline conditions, while retaining permeability to water molecules, O$_2$ and protons. In this regard, future work will involve replacing PDDA with other cationic polymer candidates typically used in LbL methodologies, such as poly(aniline) (PANI), poly(ethylene imine) (PEI), poly-L-lysine, etc. This inherent versatility of a LbL approach is a major advantage to ensure the preparation of stable and catalytically active IrO$_x$ modified WOR electrodes over the entire pH range.
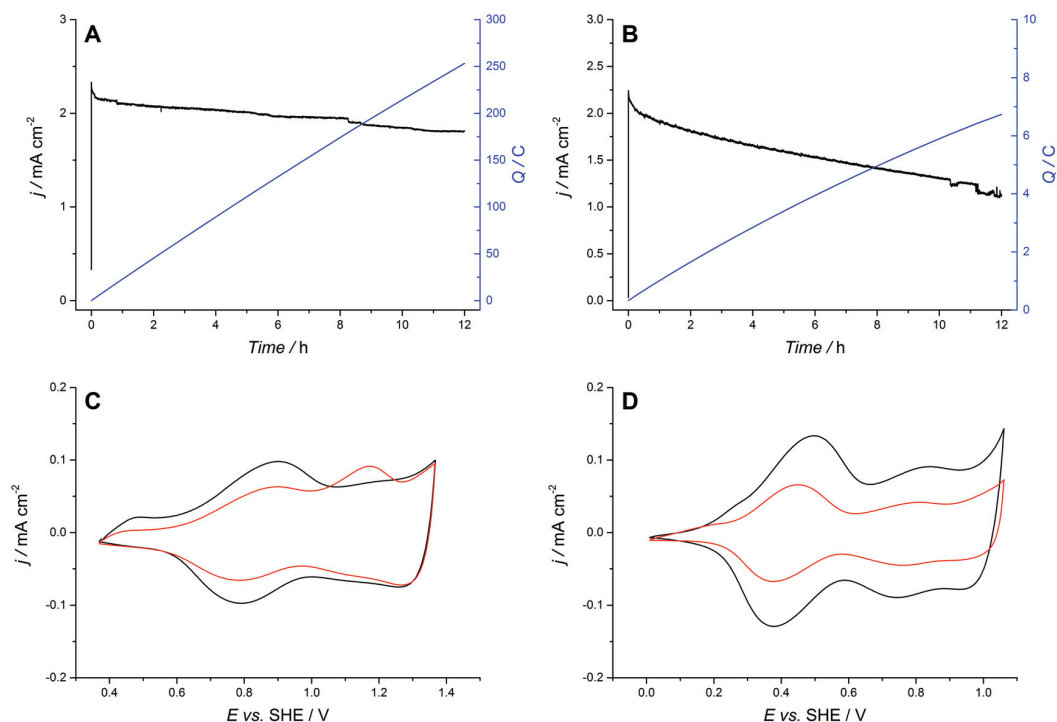
Figure 2.16 Long-term bulk electrolysis experiments. (A, B) Chronoamperometric plots of the current (black line) and charge (blue line) during water electrolysis using an FTO electrode modified with 14 IrO_x/PDDA bilayers in a classic bulk electrolysis cell. In each case an overpotential (η) of +600 mV *vs.* the thermodynamic potential for the WOR was applied to the working electrode. The experiments were carried out in (A) 0.1 M $HClO_4$ and (B) 0.5 M phosphate buffer solution (pH = 7). The figures (C, D) depict the CVs recorded before (black line) and after (red line) electrolysis for the systems described in (A , B). The scan rate used was 10 mV·s^{-1}.

The maximum current density obtained by the FTO electrode modified with 14 IrO_x/PDDA bilayers at η = +400 mV under acidic conditions was 1.5 mA cm^{-2} (Figure 2.16 A). Much higher current densities at η = +400 mV, in the region of 30 to 100 mA cm^{-2}, are required to implement our LbL modifed FTO electrodes in solar or electrolyzer technology. To achieve this, future work will involve changing the experimental conditions (*e.g.,* by varying the concentration of colloidal IrO_x NPs in the dipping solution or replacing and/or using an alternative polymer to PDDA, as noted vide supra) to increase the number of active centres per bilayer and improve the relatively low surface coverages of catalytic IrO_x NPs herein (10^{-9} nmol·cm^{-2}) one order of magnitude.

Also, to highlight the activity of the IrO_x NPs in the PDDA-polymer environment, a comparison was made by normalizing the current density (1.5 mA·cm^{-2}) with the surface coverage (35 nmol·cm^{-2}) for bulk electrolysis carried out under acidic

conditions (see Figure 2.16 A). A value of 0.22 $A \cdot cm^{-2} \cdot mg^{-1}$ was attained and this is close to the value of 0.3 $A \cdot cm^{-2} \cdot mg^{-1}$ reported by Millet and co-workers for an optimized system for water electrolysis[37]. Thus, by further optimizing our experimental conditions to find an order of magnitude increase in the surface coverage of IrO_x NPs, and maintaining or increasing the activity of the individual IrO_x NPs under these optimised conditions, our methodology will be viable for applications in solar and electrolyzer applications.

2.4   Conclusions

Layer-by-layer assembly of catalytic IrO_x NPs represents a flexible, reproducible and scalable approach to developing WOR electrodes. Crucially the resulting "tissue-like" amorphous films allow the as-synthesized IrO_x NPs trapped therein to retain their original shapes and sizes. The latter is key to maintaining the intrinsic catalytic activity of the IrO_x NPs and this is seen in the low overpotentials (0.22 to 0.28 V) necessary to achieve O_2 evolution across the pH range 1 − 13 studied herein. The surface coverage of electrochemically addressable iridium centers can be finely tuned by incorporation of additional IrO_x/PDDA bilayers improving the kinetics of the WOR substantially, as shown by the CV at high potentials. The chosen positively charged polymer in this study, PDDA, is stable under acidic and neutral conditions. Although the films discussed herein are unstable in alkaline conditions the flexibility inherent to a layer-by-layer approach means that in future studies we simply need to replace PDDA with a positively charged polymer that can resist basic conditions.

2.5 Bibliography

[1]   Nakagawa, T.; Beasley, C. A.; Murray, R. W. *The Journal of Physical Chemistry C* 113, (**2009**), 12958-12961.

[2]   Nakagawa, T.; Bjorge, N. S.; Murray, R. W. *Journal of the American Chemical Society* 131, (**2009**), 15578-15579.

[3]   Zhao, Y.; Hernandez-Pagan, E. A.; Vargas-Barbosa, N. M.; Dysart, J. L.; Mallouk, T. E. *The Journal of Physical Chemistry Letters* 2, (**2011**), 402-406.

[4]   Chuang, M.-C.; Ho, J.-a. A. *RSC Advances* 2, (**2012**), 4092-4096.

[5]   Hsiao, H.-Y.; Chuang, M.-C. *Electrochimica Acta* 137, (**2014**), 190-196.

[6]   Mirbagheri, N.; Chevallier, J.; Kibsgaard, J.; Besenbacher, F.; Ferapontova, E. E. *ChemPhysChem* 15, (**2014**), 2844-2850.

[7]   Harriman, A.; Richoux, M.-C.; Christensen, P. A.; Mosseri, S.; Neta, P. *Journal of the Chemical Society, Faraday Transactions 1: Physical Chemistry in Condensed Phases* 83, (**1987**), 3001-3014.

[8]   Harriman, A.; Pickering, I. J.; Thomas, J. M.; Christensen, P. A. *Journal of the Chemical Society, Faraday Transactions 1: Physical Chemistry in Condensed Phases* 84, (**1988**), 2795-2806.

[9]   Bell, A. T. *Science* 299, (**2003**), 1688-1691.

[10]   Kaschak, D. M.; Mallouk, T. E. *Journal of the American Chemical Society* 118, (**1996**), 4222-4223.

[11]   Yagi, M.; Tomita, E.; Kuwabara, T. *Journal of Electroanalytical Chemistry* 579, (**2005**), 83-88.

[12]   Kuwabara, T.; Tomita, E.; Sakita, S.; Hasegawa, D.; Sone, K.; Yagi, M. *The Journal of Physical Chemistry C* 112, (**2008**), 3774-3779.

[13]   Zhao, Y.; Vargas-Barbosa, N. M.; Hernandez-Pagan, E. A.; Mallouk, T. E. *Small* 7, (**2011**), 2087-2093.

[14]   Michaux, K. E.; Murray, R. W. *Langmuir* 29, (**2013**), 12254-12258.

[15]   Tilley, S. D.; Cornuz, M.; Sivula, K.; Grätzel, M. *Angewandte Chemie International Edition* 49, (**2010**), 6405-6408.

[16]   Yagi, M.; Tomita, E.; Sakita, S.; Kuwabara, T.; Nagai, K. *The Journal of Physical Chemistry B* 109, (**2005**), 21489-21491.

[17]   Petit, M. A.; Plichon, V. *Journal of Electroanalytical Chemistry* 444, (**1998**), 247-252.

[18]   Hoertz, P. G.; Kim, Y.-I.; Youngblood, W. J.; Mallouk, T. E. *The Journal of Physical Chemistry B* 111, (**2007**), 6845-6856.

[19]   Buckley, D. N.; Burke, L. D. *Journal of the Chemical Society, Faraday Transactions 1: Physical Chemistry in Condensed Phases* 71, (**1975**), 1447-1459.

[20]   Buckley, D. N.; Burke, L. D. *Journal of the Chemical Society, Faraday Transactions 1: Physical Chemistry in Condensed Phases* 72, (**1976**), 2431-2440.

[21]   Buckley, D. N.; Burke, L. D.; Mulcahy, J. K. *Journal of the Chemical Society, Faraday Transactions 1: Physical Chemistry in Condensed Phases* 72, (**1976**), 1896-1902.

[22]   Burke, L. D.; Whelan, D. P. *Journal of Electroanalytical Chemistry and Interfacial Electrochemistry* 124, (**1981**), 333-337.

[23]   Conway, B. E.; Mozota, J. *Electrochimica Acta* 28, (**1983**), 9-16.

[24]   Burke, L. D.; Mulcahy, J. K.; Whelan, D. P. *Journal of Electroanalytical Chemistry and Interfacial Electrochemistry* 163, (**1984**), 117-128.

[25]   Burke, L. D.; Whelan, D. P. *Journal of Electroanalytical Chemistry and Interfacial Electrochemistry* 162, (**1984**), 121-141.

[26]   Pickup, P. G.; Birss, V. I. *Journal of Electroanalytical Chemistry and Interfacial Electrochemistry* 240, (**1988**), 171-183.

[27]   Bock, C.; Birss, V. I. *Electrochimica Acta* 46, (**2001**), 837-849.

[28]   Steegstra, P.; Ahlberg, E. *Electrochimica Acta* 76, (**2012**), 26-33.

[29]   Steegstra, P.; Busch, M.; Panas, I.; Ahlberg, E. *The Journal of Physical Chemistry C* 117, (**2013**), 20975-20981.

[30]   Honeychurch, M. J.; Rechnitz, G. A. *Electroanalysis* 10, (**1998**), 285-293.

[31]   Myland, J. C.; Oldham, K. B. *Journal of Electroanalytical Chemistry* 530, (**2002**), 1-9.

[32]   Lyons, M. E. G.; Doyle, R. L.; Brandon, M. P. *Physical Chemistry Chemical Physics* 13, (**2011**), 21530-21551.

[33]   Kim, J.; Kim, B.-K.; Cho, S. K.; Bard, A. J. *Journal of the American Chemical Society* 136, (**2014**), 8173-8176.

[34] Stevens, T. S.; Creighton, E. M.; Gordon, A. B.; MacNicol, M. *Journal of the Chemical Society (Resumed)*, (**1928**), 3193-3197.

[35] Dunn, J. L.; Stevens, T. S. *Journal of the Chemical Society (Resumed)*, (**1932**), 1926-1931.

[36] Vanecko, J. A.; Wan, H.; West, F. G. *Tetrahedron* 62, (**2006**), 1043-1062.

[37] Millet, P.; Ngameni, R.; Grigoriev, S. A.; Mbemba, N.; Brisset, F.; Ranjbari, A.; Etiévant, C. *International Journal of Hydrogen Energy* 35, (**2010**), 5043-5052.

Chapter 3

Layer-by-Layer Inkjet Printing of IrO$_x$-Based pH-Sensors

_____

3.1   Introduction

Monitoring the pH is of fundamental importance in both research and industry as many chemical and biological processes are pH-dependent. The most widespread pH sensor is the ion-selective glass electrode thanks to its outstanding selectivity to protons and relatively fast response time. Nevertheless, the inherent fragility, high impedance, membrane fouling and the difficulties in miniaturization of the glass membrane limit its application in many areas[1,2]. To date many alternatives to the convectional glass membrane electrode have been proposed, such as ion-sensitive field effect transistors (ISFETs)[3-6], the implementation of hydrogels[7] and the use of metal oxide electrodes among others[8]. Metal oxides offer several crucial advantages, such as a linear response over a wide pH range, resistance to harsh environments where the glass membrane is affected and the ease and flexible preparation by using microfabrication techniques[1,2,9].

IrO$_x$-based pH sensors are one of the most promising among metal oxide bases

sensors, due to a good stability over a broad pH range at, high temperature[10], high pressure[9] and in presence of aggressive environments[11]. Furthermore, they show a fast response even in non-aqueous solutions[12] and excellent biocompatibility[13]. In Chapter 2 a LbL approach was described to obtain reproducible IrO_x NP films with good electrochemical properties, and potentially usable in solar energy applications[14]. However, to avoid the necessity of intermediate rinsing steps, and in order to approach batch production, alternative fabrication techniques are required. Inkjet printing (IJP) is a digital, mask-less and contact-less material deposition technique with high flexibility in terms of pattern design and ink composition and it shows a high accuracy of the ink droplet deposition.[15,16] Alternating inkjet printing of two solutions from two parallel printheads to generate LbL assemblies brings an improved nanoscale control over the layer thickness, homogeneity, variable coverage of the surface with change of the number of bilayers, and facile manipulation of pattern dimensions. Furthermore, through the well-controlled amount of deposited material, the intermediate rinsing steps needed in LbL dipping approach, could potentially be reduced, or completely avoided. Therefore, only a final rinsing step would be applied to remove the low molecular weight species such as the ion excess of each component.

In this chapter, we present the fabrication and application of IrO_x-based potentiometric pH sensors using the concept of layer-by-layer inkjet printing (LbL IJP) deposition. LbL assemblies were composed of positively charged PDDA and negatively charged IrO_x citrate-stabilized NPs and deposited alternately on flexible ITO/PET substrates. Both, the IrO_x and PDDA inks were formulated and carefully optimized to fulfill the requirements for stable inkjet printing and good ink-substrate interaction. The electrodes were characterized by scanning electron microscopy as well as optical and electrochemical methods. Compared to the LbL approach presented in the previous chapter, the production rate has drastically been increased while achieving a similar pH sensing performance, reduced material waste, low cost, patterned surface, timesaving and scalability for mass production.

3.2   Materials and methods

3.2.1 Chemicals

All chemicals were used as received without further purification. ITO/PET substrates (60 Ω/sq, 125 μm thickness), potassium hexachloroiridate (K$_2$IrCl$_6$, 99.99%), tri-sodium citrate dihydrate (≥99.0), poly(diallydimethylammonium chloride) (PDDA, 20% wt. in water, medium molecular weight Mw 200 000 – 350 000) and perchloric acid (HClO$_4$, 70%), sodium dihydrogen phosphate dihydrate (NaH$_2$PO$_4$•2H$_2$O, 99%), di-sodium hydrogen phosphate dodecahydrate (Na$_2$HPO$_4$•12H$_2$O, 99%) were purchased from Sigma Aldrich, while di-sodium tetraborate decahydrate was ordered from Acros (Na$_2$B$_4$O$_7$ •12H$_2$O, 99.5%).

All aqueous solutions were prepared with ultrapure water (Millipore Milli-Q, specific resistivity 18.2 MΩ·cm). Pure O$_2$ (medical) cylinders were purchased from Carbagas.

3.2.2 Synthesis of IrO$_x$ NPs

The IrO$_x$ NPs were synthesized by using a slightly modified method than the one reported in Chapter 2. Herein, the amount of K$_2$IrCl$_6$ and tri-sodium citrate-dihydrate was 0.302 g and 0.547 g, respectively. Therefore, the final concentration of IrO$_x$ NPs was 31 mM.

3.2.3 Ink preparation

Two different ink formulations were developed. The first ink, containing PDDA, was prepared by diluting medium molecular weight PDDA (20% wt. in water, Aldrich) and mixing with isopropanol in ratio 3:1 (v/v) to reach a final concentration of 0.0025%. The second ink, containing IrO$_x$, was obtained by mixing the as-synthetized IrO$_x$ NPs (Section 3.2.2) with isopropanol in ratio 1:1 (v/v), reaching a final IrO$_x$ concentration of 1.24 mM.

Surface tension measurements of the two inks were performed using a Drop Shape Analyzer DSA30S (Krüss, Germany). The viscosity was determined with a SV-1A series viscometer (A&D, Japan), while the particle size distribution was measured using a ZetaSizer Nano ZS (Malvern, UK).

3.2.4 Inkjet printing of the PDDA-IrO$_x$/ITO/PET electrode

The pH sensors were fabricated using an X-Serie CeraPrinter (Ceradrop, France) composed of three parallel piezoelectric drop-on-demand printheads, *i.e.*, two Q-Class Sapphire QS-256 at a time each with 256 individually addressable nozzles for either 10, 30 or 80 pL nominal droplet volumes and one disposable cartridge DMC-11610 (all printheads from Dimatix Fujifilm, USA) containing 16 individually addressable nozzles with 10 pL nominal droplet volume. The LbL assemblies were then achieved by the alternate deposition of the PDDA and IrO$_x$ inks from one QS-256 30 pL printhead and one disposable cartridge, respectively. Prior to the deposition, the ITO/PET substrates were cleaned with acetone, immersed in 1 mM NaOH for 30 min and finally treated with oxygen plasma (Diener Electronics) for 15 min. The latter process increased the surface energy of the substrate improving the wetting properties for the PDDA ink.

Custom waveforms were used to gain optimal droplet formation. The print designs were created with the CeraSlice software from Ceradrop. Several print parameters were optimized including splat diameter, substrate temperature and printhead height (*i.e.*, 0.5 mm). In order to achieve a high quality film, while using a minimum volume of the ink formulation, a single nozzle, with a splat diameter of 80 µm and 40 µm droplet interpenetration was used for the PDDA ink. On the other hand, three nozzles were used for the IrO$_x$ ink with 40 µm splat diameter and 10 µm of droplet interpenetration. A slightly increased optimum substrate temperature of 40 °C was used during the printing, ensuring rapid drying of the ink at the substrate, while avoiding precipitation and subsequent blockage of the nozzles (*i.e.*, by the heat transfer from the substrate to the printhead for long term printings). Priming patterns were printed before the real electrodes for droplet stabilization in addition to the printhead cleaning cycles prior and after the printing process.

3.2.5 Pattern/sensor characterization

The printed patterns were analyzed using a Merlin Zeiss high-resolution scanning electron microscope (HR SEM) equipped with a Gemini II column and a secondary electron in-lens detector. Cyclic voltammograms (CVs) were recorded with a PGSTAT128N Autolab potentiostat (Metrohm, The Netherlands) in a three-electrode arrangement using the ITO/PET electrode modified with 1 - 5 PDDA-IrO$_x$ bilayers as a working electrode (WE), a platinum wire as counter electrode (CE) and Ag/AgCl (3 M NaCl) as a reference electrode (RE). The open-circuit potential (OCP) of the inkjet printed pH electrodes was measured as a function of the pH of various buffer solutions (pH 3 – 11) using a custom-made robot and intermittent cleaning procedures.

3.3 Results and discussion

3.3.1 Ink formulation and printing of the electrodes

The quality of inkjet-printed patterns can be affected mainly by three factors: ink properties, printing conditions and substrate surface properties. A good ink formulation needs to fulfill several requirements in terms of physicochemical properties and fluid dynamics (*e.g.,* particle size, viscosity and surface tension). In general, the optimal viscosity for ink jettable fluids in piezoelectric drop-on-demand printers is in the range of 3–20 mPa·s, while the optimum surface tension is around 30 mN/m.[17]

The PDDA polymer ink was prepared by diluting the aqueous PDDA solution with isopropanol (Section 3.2.1) in order to lower the surface tension of the ink from 72 to 30 mN/m. The viscosity of this ink was found to be 2.4 mPa s and no particles above 1 nm were detected (Figure 3.1a-c). The IrO$_x$ ink was prepared by using the as-synthesized IrO$_x$ NPs (Section 3.2.2). The size of the particles in the ink must be at least two orders of magnitude smaller than the diameter of the nozzle orifice in the printhead to prevent clogging and nozzle blockage. Characterization of the IrO$_x$ NPs

demonstrated that the synthesis method described above produced nanoparticles with a narrow size distribution centered at *ca.* 10 nm and hence suitable for inkjet printing. The IrO$_x$ colloid was mixed with isopropanol reaching a viscosity and surface tension of 2.8 mPas and of 22 mN/m, respectively (Figure 3.1d-f). In both cases, the inks fulfilled the major requirements for inkjet printing and were stable during the entire printing process.
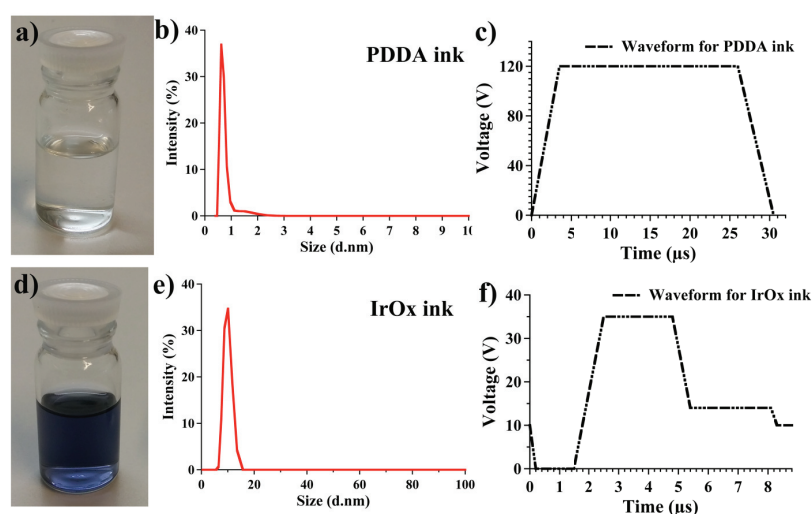

Figure 3.1 Ink formulations including particle size distribution measurements and applied jetting waveforms for the PDDA (a-c) and IrO$_x$ ink (d-f).

The LbL inkjet printing process started with the deposition of the positively charged PDDA on the negatively charged ITO/PET substrate (Figure 3.2). The ink solvents evaporated rapidly resulting in a film of positively charged polymer on the substrate surface. Then, negatively charged IrO$_x$ nanoparticles were printed restoring the negative charge of the surface. This process was then repeated until the desired number of bilayers was achieved. In all cases the patterns were homogeneous, *i.e.*, well-defined printed bands with sharp periphery and uniform loading were achieved.

Ideally, the LbL IJP deposition of one material should be carried out in a way that the amount of deposited material is restricted to a monolayer, thus leading to a charge reversal on the surface. This could be achieved by the delivery of a precise amount of material compared to the previously printed layer. However, the challenging optimization of the ratio between the components of the assemblies seems not to be

required as previously demonstrated [18], and by the obtention of stable inkjet printed PDDA-IrOx LbL assemblies herein. For instance, Andres *et al.* reported the formation of stable deposits of PDDA and Au NPs by using a LbL IJP approach[18]. In order to investigate the surface coverage, the authors deposited several printed Au NP layers over a PDDA-modified substrate. Their deposits were stable to rinsing and based on their results, the authors concluded that a strict ratio between the two-bilayer components is not required. As a first approximation, the concentration of both PDDA and IrO$_x$ NPs used in this work was in a similar range as those previously reported by Andres *et al.* using citrate-stabilized Au NPs with similar particle sizes (*i.e.,* 13 nm). It can be expected that in the event of an excess of either the polyelectrolyte or nanoparticles, the extrinsic charge compensation via counter ions may occur without the destabilization of the film. Ongoing experiments are devoted to the optimization of the amount of polymer deposited in order to increase even further the robustness of the assemblies.
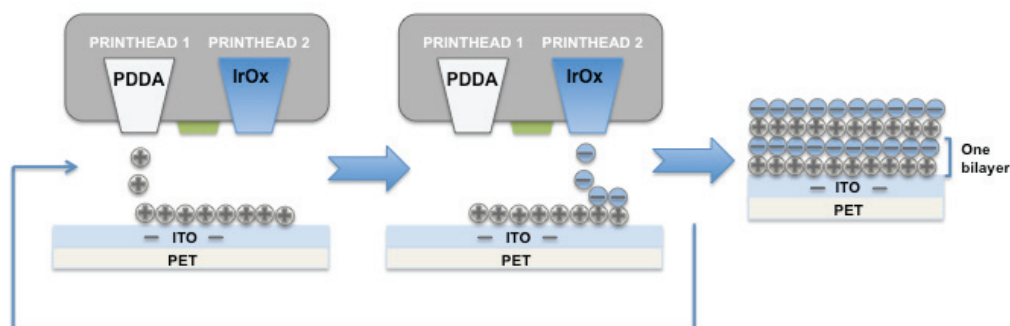
Figure 3.2 Schematic representation of LbL IJP of negatively and positively charged particles for pH sensing.

3.3.2 Morphological characterization

Figure 3.3 shows the HR SEM images for an ITO/PET electrode surface modified with 5 PDDA-IrO$_x$ bilayers. At micrometer scale (Fig. 3.3a), the IrO$_x$ NPs are present in an inhomogeneous pattern with some regions of the substrate are practically uncovered. This was the result of the accumulation of IrO$_x$ NPs in the deposited ink droplets during the drying process. A closer inspection of highly dense regions (Figure 3.3b) shows the particles visible as white clusters of 20-200 nm in size, contrasting strongly with the bare ITO surface (Fig. 3.3c).

Figure 3.3 (A, B) HR SEM at two different magnifications of the surface morphology of an ITO electrode modified with five IJP PDDA- IrO$_x$ bilayers (C) For comparison, a SEM image of the bare FTO electrode is shown.
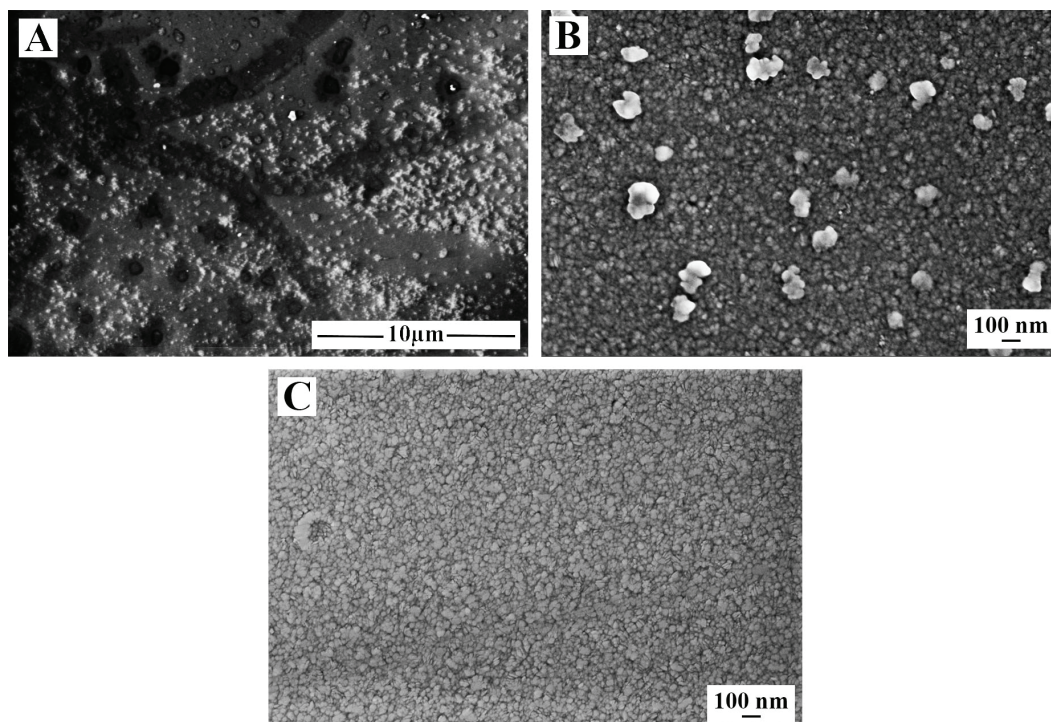
3.3.3 Electrochemical characterization

3.3.3.1   Cyclic Voltammetry

Figure 3.4 shows the cyclic voltammetry in 0.5 M phosphate buffer solution (pH 7) for ITO/PET substrates modified with 1 - 5 bilayers of PDDA-IrO$_x$. The voltammetric profile is very different from that of hydrated iridium oxide films (HIROFs),[14,19,20] displaying a rather irreversible signal with a cathodic peak at 0.1 V and the counter anodic part at 0.4 V. Yang *et al.*[19] reported that electrodeposited IrO$_x$ obtained by anodic deposition exhibit the typical behavior of HIROFs, including well-defined waves for the processes termed as Ir(III)/Ir(IV). However, all features of the voltammetry practically disappear after heat treatment. Those modifications, which were accompanied to a transition from super-Nernstian to near-Nernstian pH-dependence, were attributed to changes in the porosity and oxidation state. Herein, the presence of low hydrated islands of IrO$_x$ can also be responsible for the irreversible waves. Additionally, some portions of the film can be poorly conductive due to the small excess of one or another component in the bilayer assembly.
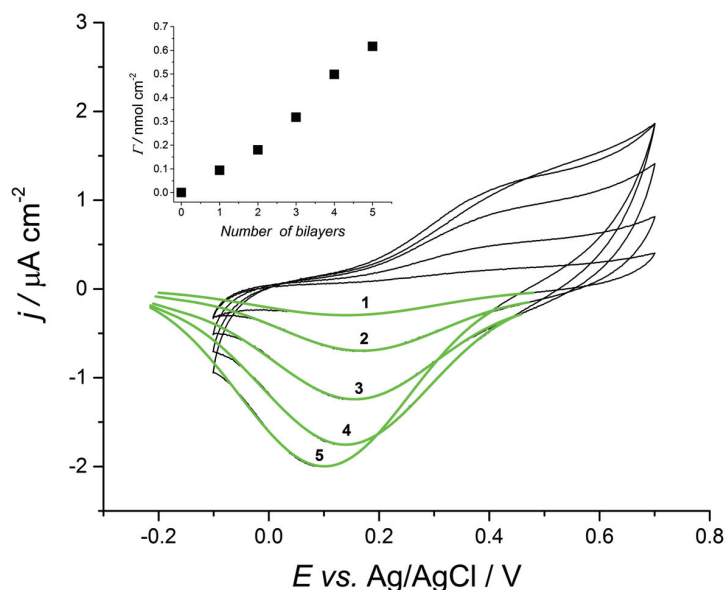
Figure 3.4 Cyclic voltammograms of bare ITO/PET electrode and electrode modified with 1 – 5 PDDA-IrO$_x$ bilayers. The green lines corresponds to the fittings of the Ir(III)/Ir(IV) cathodic peak using Gaussian fit functions to integrate the charge (Q / C) and estimate the surface coverage of electrochemically active IrO$_x$ (Γ / nmol cm^{-2}). Scan rate 10 mV s^{-1}, supporting electrolyte 0.5 M phosphate buffer solution (pH 7). Inset plot: surface coverage of electrodes with 1 – 5 PDDA-IrO$_x$ bilayers.

The determination of the active surface coverage Γ of the electrochemically active IrO$_x$ NPs was performed by integrating the charge Q under the cathodic peak at ≈ 0.1 V using Gaussian fit functions and applying the equation $\Gamma = Q/nFA$, where F is the faraday constant, A is the area of the electrode and n is the number of electrons transferred per active center, which is assumed to be 1. The inset of Figure 3.4 shows that the coverage increases linearly with increasing number of bilayers, reflecting that the number of sensing centers can be precisely controlled by the incorporation of further bilayers. Noteworthy, the coverage obtained for one bilayer (0.094 nmol cm^{-2}) represents a $\approx 7\%$ of the total amount of IrO$_x$, calculated from the total volume of ink deposited per bilayer (0.6 µL) to have an electrode area of 0.54 cm^2. Based on the fraction of iridium atoms the surface of the IrO$_x$ NPs prepared under similar conditions (15%)[21], it can be concluded that the aggregation process upon deposition does not cause dramatic changes in the number of active iridium centers, thus keeping useful the methodology present herein for the deposition of high-surface IrO$_x$ NPs.

According to the pH dependence of the potential, the mechanism of the pH sensing could be described based on one of the following 1e$^-$/1H$^+$ processes[19,20]:

$$Ir_2O_3 + 6H^+ + 6e^- \rightleftharpoons 2Ir + 3H_2O \qquad (3.1)$$

$$IrO_2 + 4H^+ + 4e^- \rightleftharpoons Ir + 2H_2O \qquad (3.2)$$

$$2IrO_2 + 2H^+ + 2e^- \rightleftharpoons Ir_2O_3 + H_2O \qquad (3.3)$$

3.3.3.2   OCP measurements

Effect of the number of layers

The open-circuit potential (OCP) of the IJP pH electrodes from 1 – 5 bilayers was measured as a function of the pH for different buffer solutions ranging from pH 3 – 11, *vs*. the conventional Ag/AgCl (3 M KCl) reference electrode. The geometric area for all printed pH electrodes was ~ 0.54 cm^2 and the pH sensors were used directly after the printing process without further pretreatment. The pH sensing and reference electrodes were placed in an arm holder of a custom-made robot as the one used for LbL deposition in the previous chapter (Section 2.2.3). In this way, it was possible to immerse the electrodes into different buffer solutions and measure the OCP continuously for 6 min. The potential–pH curve was constructed for the electrodes with 1 - 5 bilayers, in the used buffer range. All obtained values, including the pH sensitivity (calculated from the slope of the curve), the offset at pH 0 (E^0), Pearson's correlation coefficient (R^2) and the drift of the potential during the measurement are summarized in Table 3.1.

Table 3.1. pH sensitivity of the IJP pH electrodes as a function of the number of bilayers.

Number of bilayers	1	2	3	4	5
Slope (mV/pH)	59	58	58	59	58
E_0 (mV)*	612	609	608	610	608
r^2	0.936	0.955	0.989	0.994	0.996
Drift (mV)	0 - 44	0 - 36	0 - 28	0 - 16	0 - 10

**Potential value extrapolated to at pH=0.*

The pH electrodes showed a linear response in the examined pH range (Table 3.1). The response of the electrodes upon immersion into the buffer solutions was rapid reaching a stable value after 2 - 3 s. It is known that the pH-sensing properties of IrO$_x$ films are sensitive to the structure, composition and oxidation state, which strongly depend on the fabrication method. Hitchman *et al.*[22] and Olthius *et al.*[23] correlated the pH sensitivity of IROFs with the oxidation state of iridium, associating the higher oxidation state with a higher slope. In case of typical hydrous materials, such as those prepared by oxidation of iridium substrates, super-Nernstian slopes (60 – 80 mV/pH) were reported[24]. Conversely, the inkjet printed IrO$_x$ films reported herein exhibit slopes of 58 mV/pH, which are nearly identical to that predicted by the Nernst equation, suggesting that under the present conditions they behave rather as an anhydrous material. On the other hand, the potential drift decreased drastically with increasing number of bilayers (Table 3.1). For the 5-bilayer electrode the maximum drift value was 10 mV, which is fairly low compared to 44 mV for 1-bilayer. Hence, very stable pH sensors were prepared with low coverage of Ir (*i.e.*, Γ < 1 nmol cm^{-2}).

Reproducibility

In order to fully evaluate the pH-sensing characteristics and to demonstrate the reproducibility of the inkjet printing process, the potential – pH dependence of five different 5-bilayer electrodes from the same batch (*vs.* Ag/AgCl (3 M KCl) reference electrode) were evaluated using two measurement protocols: acid-to-base and base-to-acid direction (Figure 3.5, Table 3.2). These protocols were implemented by synchronizing the robot and potentiostat software, and performed via the sequential immersion of the electrodes into the buffer solutions (pH 3, 5, 7, 9 and 11 and *vice versa*), followed by cleaning steps in order to avoid cross-contamination (30 s in deionized water). All measurement protocols were repeated with five different 5-bilayer electrodes.

The average sensitivity obtained for the 5-bilayer IJP electrodes was 58.4 mV/pH, with an RSD of 0.60% (*n* = 5), confirming the excellent reproducibility of the IJP process with a correlation coefficient greater than 0.99 for all measurements. The response time was calculated as the time necessary to reach 90% transition of the potential difference, which was 1 s in unstirred solutions[25].
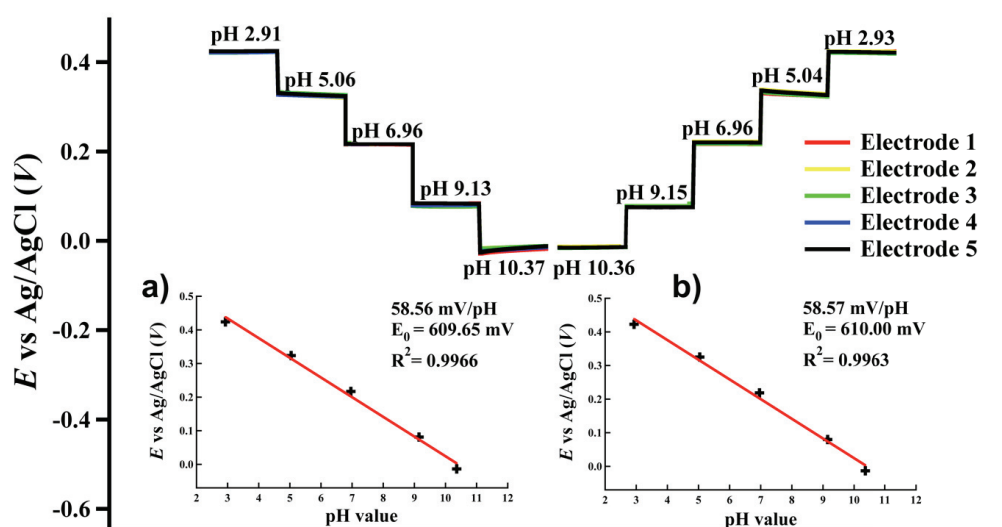
Figure 3.5 pH measurements of the different 5-bilayer IJP electrodes from the same printed batch, for acid-to-base and base-to-acid protocols. Inset plots represent the average potential – pH dependence for a) acid-to-base and b) base-to-acid direction (*the error bars represent the standard deviation for five different electrodes*; *bars are smaller than the data symbol employed*).

Table 3.2 Reproducibility and pH sensing characteristics of the 5-bilayer IJP electrodes.

Parameter	Titration	Average	Std. Deviation
Slope (mV/pH)	Acid-Base	58.4	0.2
	Base-Acid	58.4	0.4
E^0 (mV)*	Acid-Base	608.5	1.0
	Base-Acid	608.8	3.2

Potential value extrapolated to at pH=0.

The main source of the drift of iridium oxide-based pH electrodes in environmental conditions is dissolved oxygen. However, the LbL IJP IROFs do not show measurable interferences from stirring the solution during the measurement or from the presence of dissolved oxygen in the solution.

3.4 Conclusions

A novel method for the large-scale fabrication of pH-sensitive films using layer-by-layer inkjet printing was illustrated. It was been shown that such methodology can be successfully used for the fabrication of thin nanofilm bilayers of oppositely charged IrO$_x$ nanoparticles and PDDA polymer. Simple control over the NP surface coverage with the number of printed bilayers provided fast tuning of pH sensing properties. The printed pH electrodes exhibited fast response time, excellent reproducibility and near-Nernstian sensitivity (58 - 59 mV/pH). The results presented herein could be the basis of novel, facile and economical possibilities for the research and development as well as mass production of flexible and disposable potentiometric pH sensors for a wide range of applications. Compared to our previous LbL dip coating approach for PDDA-IrO$_x$-bilayer electrodes for energy conversion a drastic increase in the production rate was achieved with various advantages including minimum material waste, low cost, defined and flexible patterns, timesaving and up-scalability

3.5 Bibliography

[1]   Ges, I. A.; Ivanov, B. L.; Schaffer, D. K.; Lima, E. A.; Werdich, A. A.; Baudenbacher, F. J. *Biosensors and Bioelectronics* 21, (**2005)**, 248-256.

[2]   Carroll, S.; Baldwin, R. P. *Analytical Chemistry* 82, (**2010)**, 878-885.

[3]   Cané, C.; Gràcia, I.; Merlos, A. *Microelectronics Journal* 28, (**1997)**, 389-405.

[4]   Han, J.; Cui, D.; Li, Y.; Zhang, H.; Huang, Y.; Zheng, Z.; Zhu, Y.; Li, X. *Sensors and Actuators B: Chemical* 66, (**2000)**, 203-204.

[5]   Shitashima, K.; Kyo, M.; Koike, Y.; Henmi, H. In *Underwater Technology, 2002. Proceedings of the 2002 International Symposium on* 2002, p 106-108.

[6]   Dong, Z.; Wejinya, U. C.; Elhajj, I. H. *Sensors and Actuators A: Physical* 194, (**2013)**, 181-187.

[7]   Gerlach, G.; Guenther, M.; Sorber, J.; Suchaneck, G.; Arndt, K.-F.; Richter, A. *Sensors and Actuators B: Chemical* 111–112, (**2005)**, 555-561.

[8]   Fog, A.; Buck, R. P. *Sensors and Actuators* 5, (**1984)**, 137-146.

[9]   Katsube, T.; Lauks, I.; Zemel, J. N. *Sensors and Actuators* 2, (**1981)**, 399-410.

[10]   Wang, M.; Yao, S.; Madou, M. *Sensors and Actuators B: Chemical* 81, (**2002)**, 313-315.

[11]   Lauks, I.; Yuen, M. F.; Dietz, T. *Sensors and Actuators* 4, (**1983)**, 375-379.

[12]   Izutsu, K.; Yamamoto, H. *Analytical Sciences* 12, (**1996)**, 905-909.

[13]   Lu, Y.; Wang, T.; Cai, Z.; Cao, Y.; Yang, H.; Duan, Y. Y. *Sensors and Actuators B: Chemical* 137, (**2009)**, 334-339.

[14]   Hidalgo-Acosta, J. C.; Scanlon, M. D.; Mendez, M. A.; Amstutz, V.; Vrubel, H.; Opallo, M.; Girault, H. H. *Physical Chemistry Chemical Physics* 18, (**2016)**, 9295-9304.

[15]   Lesch, A.; Cortés-Salazar, F.; Amstutz, V.; Tacchini, P.; Girault, H. H. *Analytical Chemistry* 87, (**2015)**, 1026-1033.

[16]   Lesch, A.; Cortés-Salazar, F.; Bassetto, V. C.; Amstutz, V.; Girault, H. H. *CHIMIA International Journal for Chemistry* 69, (**2015)**, 284-289.

[17]   de Gans BJ, S. U. *Macromolecular Rapid Communications* 24, (**2003)**, 659-666.

[18] Andres, C. M.; Kotov, N. A. *Journal of the American Chemical Society* 132, (**2010**), 14496-14502.

[19] Kim, T. Y.; Yang, S. *Sensors and Actuators B: Chemical* 196, (**2014**), 31–38.

[20] Steegstra, P.; Ahlberg, E. *Electrochimica Acta* 76, (**2012**), 26-33.

[21] Morris, N. D.; Suzuki, M.; Mallouk, T. E. *J. Phys. Chem. A* 108, (**2004**).

[22] Hitchman, M. L. R., S. *Analyst* 116, (**1991**), 1131–1133.

[23] Olthuis, W. R., M. A. M.; Bergveld, P.; Bos, M.; van der Linden, W. E. *Sens. Actuators B* 2, (**1990**), 247–256.

[24] Burke, L. D. W., D. P. *J. Electroanal. Chem. Interfacial Electrochem.* 124, (**1981**), 333-337.

[25] Huang, X. R. R., Q. Q.; Yuan, X. J.; Wen, W.; Chen, W.; Zhan, D. P *Electrochemistry Communications* 40, (**2014**), 35 – 37.

Chapter 4

Catalysis of Water Oxidation in Acetonitrile by Iridium Oxide Nanoparticles

_____

4.1   Introduction

The catalytic WOR in aqueous media is well documented in literature.[1-5] However, relatively few studies have been devoted to the influence of primarily non-aqueous conditions, such as trace water present in organic solvents or ionic liquids.[6-9] Such a bias for aqueous conditions is surprising given that (*i*) Nature carries out the WOR under hydrophobic conditions in the presence of trace water as the O_2-evolving complex of Photosystem (II) is embedded in the lipid environment of thylakoid membranes,[10,11] (*ii*) the stabilities of molecular water oxidation catalysts (WOCs) are known to improve in non-aqueous environments[12] and (*iii*) changes in the solvation environment of water are known to drastically modify its physicochemical properties[13] and reactivity.[8,14]

The use of co-solvents has proven to be a good approach to modify the reactivity of the water molecule. In this regard, Meyer and co-workers reported that the rate of

the WOR at nanostructured indium tin oxide (ITO) electrodes modified with the molecular catalysts $[Ru(Mebimpy)(bpy)(OH_2)]^{2+}$ (Mebimpy = 2,6-bis(1-methylbenzimidazol-2-yl)pyridine; bpy = 2,2′-bipyridine)[6] and $[Fe^{III}(dpaq)(H_2O)]^{2+}$ (dpaq = 2-[bis(pyridine-2-ylmethyl)][7] amino-N-quinolin-8-yl-acetamido) was enhanced when mixtures of water and propylene carbonate were used as a reaction media instead of neat water. In a series of publications Bond and co-workers also highlighted the use of ionic liquids as a media to facilitate the WOR.[8,9] The exceptional reactivity was attributed to the modification of the structure of molecular water in ionic liquids where it may exist in a unique "free" state that excludes self-aggregation *via* hydrogen-bonding.

Clearly, the influence of a primarily non-aqueous environment profoundly affects the structure, reactivity and mechanistic pathways adopted by dissolved water molecules during the catalytic WOR. In this chapter, we present a systematic analysis of the influence of the constituents of the reaction media (catalyst concentration, buffer employed and especially the water content) on the catalytic WOR in water/acetonitrile (ACN) miscible solutions using well-established iridium oxide nanoparticles (IrO$_x$ NPs) as heterogeneous WOCs and $[Ru^{III}(bpy)_3]^{3+}$ as the sacrificial electron acceptor or redox shuttle.

4.2   Materials and methods

4.2.1 Chemicals

All chemicals were used as received without further purification. Ruthenium (III) chloride hydrate (RuCl$_3 \cdot x$H$_2$O, 99.98%), potassium hexachloroiridate (K$_2$IrCl$_6$, 99.99%), tri-sodium citrate dihydrate (≥99.0) and sodium bicarbonate (NaHCO$_3$, ≥99.5) were purchased from Aldrich. Tetrabutylammonium hexafluorophosphate (TBAPF$_6$, ≥99.0%), sodium hexafluorosilicate (Na$_2$SiF$_6$, 97%) and activated manganese oxide (MnO$_2$, technical grade) were ordered from Fluka, 2,2'-Bipyridine (>99%) was purchased from Acros, while potassium hexafluorophosphate (KPF$_6$, 99.5%) was received from Strem chemicals. Sulphuric acid (H$_2$SO$_4$ (95-98%) and

perchloric acid ($HClO_4$ (70%) were purchased from Aldrich. All aqueous solutions were prepared with ultrapure water (Millipore Milli-Q, specific resistivity 18.2 MΩ•cm). The organic solvents dimethyl sulfoxide (DMSO, $\geq$99.9%), toluene (>99.5%), acetone (>99.5%), diethylether (>99.8%) and ethanol (>99.8%) were purchased from Sigma. Acetonitrile (ACN, extra dry over molecular sieves, 99.9%) was ordered from Acros. Pure oxygen cylinders were purchased from Carbagas.

4.2.2 Synthetic protocols

4.2.2.1 Synthesis IrO_x NPs

The synthesis and analysis of the IrO_x NPs was performed as shown in detail Chapter 2 (Section 2.2.2)

4.2.2.2 Preparation of the Na_2SiF_6/$NaHCO_3$ buffer

The buffer was prepared as reported by Hara and coworkers [15]. Briefly, 0.705 g of Na_2SiF_6 (MW 188.06 gmol^{-1}) was dissolved in 100 mL of water and the pH was fixed to 5.7 by addition of $NaHCO_3$ under vigorous stirring. The buffer solution was then sonicated for 15 min and aged overnight in a plastic bottle. The aging step was important since the actual buffer is a poly(silicate) hydrolysis product of Na_2SiF_6. The buffer was finally filtered, and the pH fixed at 5.7 with H_2SO_4 1M.

4.2.2.3 Synthesis of $Ru(bpy)_3Cl_2$•$6H_2O$

$Ru(bpy)_3Cl_2$ was prepared using $Ru(DMSO)_4Cl_2$ as the starting material. The latter complex was prepared as reported by Evans *et al.*[1] Briefly, 3.82 mmol of $RuCl_3.xH_2O$ was dissolved in 5 ml of DMSO and refluxed for 5 min. The mixture turned a brown-orange color when the reaction was complete. The solution volume was subsequently reduced to 0.5-1.0 mL by passing a gentle stream of nitrogen gas over the gently heated liquid. The addition of acetone (20 mL) produced a yellow precipitate that was separated by filtration. This yellow solid was washed with acetone and vacuum dried.

95

In a typical synthesis, 1.34 mmol of $Ru(DMSO)_4Cl_2$ was placed in a 100 mL round-bottom flask along with 4.68 mmol of 2,2'-bipyridine and 50 mL of ethanol. The mixture was refluxed with continuous stirring until the solution turned red-orange. This color change typically took no more than 1 hour. The obtained product was dried and the solid washed with toluene in order to remove excess ligand. The dry solid was dissolved in water and slowly dropped into acetone. Finally, the precipitate was filtered, washed with acetone and dried under vacuum.

4.2.2.4   Synthesis of Ru(bpy)$_3$(PF$_6$)$_2$

The synthesis was carried out as described by Ji *et al.*[16] Briefly, 1.16 mmol of $Ru(bpy)_3Cl_2 \cdot 6H_2O$ was dissolved in 20 mL of water and added drop wise into an equal volume of a warm stirring solution containing 5.81 mmol of aqueous KPF_6. The obtained orange product was kept under stirring conditions for two hours, filtered, washed with cold water and dried under vacuum. The obtained powder was dissolved in the minimum amount of acetone and precipitated by the addition of diethylether. The microcrystalline product was filtered, washed with ether and dried under vacuum overnight. The yield was 92%.

4.2.2.5   Synthesis of Ru(bpy)$_3$(PF$_6$)$_3$

The synthesis was adapted from the procedures reported by Biner *et al.*[17] and DeSimone *et al.*[18] Briefly, 0.303 mmol of $Ru(bpy)_3Cl_2 \cdot 6H_2O$ was dissolved under stirring in 6 mL of 7 M H_2SO_4. After that, the solution was cooled in an ice/water bath. The addition of 36 mg of MnO_2 immediately produced a color change in the solution from orange to green. After 1 hour, the excess MnO_2 was separated by filtration and the liquid mixed slowly with 4.4 mL of 0.42 M aqueous KPF_6. The final step produced a green precipitate, which was filtered under vacuum and washed with a small amount of pure cold water. No decomposition of the product was observed under these conditions. The final solid was dried under vacuum for at least 4 hours. The obtained product obtained was stable for several months once stored in a refrigerator.

4.2.3 Methods

4.2.3.1   Kinetics measurements by UV-vis spectroscopy

Kinetic measurements of the WOR in water/ACN mixtures were obtained by monitoring the disappearance of the UV/vis absorbance peak corresponding to the oxidized sacrificial electron acceptor, $[Ru^{III}(bpy)_3]^{3+}$ (λ_{max} = 673 nm, prepared as the hydrophobic salt $Ru^{III}(bpy)_3(PF_6)_3$ with time using an Ocean optics USB 4000 fiber optic spectrophotometer. All kinetic measurements were performed using aqueous solutions and dry ACN solvent thoroughly de-gassed with nitrogen, under anaerobic conditions in a glovebox purged with nitrogen (O_2 < 1 ppm, H_2O < 1 ppm) and at an ambient temperature of 23 ± 2 ºC.

Two separate kinetic studies were performed. The first involved investigating the influence of "acidity regulators" and the concentration of IrO_x NPs on the rates of the WOR. Perchloric acid ($HClO_4$) and the buffer bicarbonate/hexafluorosilicate ($NaHCO_3/Na_2SiF_6$) were employed as the "acidity regulators". The total water content in the water/ACN mixture was maintained constant at 10 % (v/v) for these measurements. In a typical experiment 1.5 mL of 2.67 mM $[Ru^{III}(bpy)_3]^{3+}$ dissolved in dry ACN was placed in a quartz cuvette. Next, 0.5 mL of a water/ACN mixture (0.4:1 v/v) containing the acidity regulator and the catalyst was injected under vigorous stirring and the absorbance values at 673 nm and 900 nm recorded as a function of time. The final mixture contained either 4.3 mM $NaHCO_3/Na_2SiF_6$ or 20 mM $HClO_4$ and increasing concentrations of IrO_x NPs from 0 to 31 μM. The preparation of each sample with increasing [IrO_x NP] is detailed explicitly table 4.1

The pre-mixing of water/ACN prior to injection into the pure dry ACN solvent was essential to obtain accurate kinetic rate constants in the first seconds after injection. Direct injection of a pure aqueous solution to dry ACN leads to slow mixing and dramatic changes in the optical properties of the solution, thereby affecting accurate determination of the kinetic rate constants. However, it is noteworthy that implementing the pre-mixing protocol restricts the appearance of absorbance peak spikes or instabilities to the first second after catalyst injection. The absorbance value at 900 nm was used for background correction. This methodology enabled changes in the baseline to be corrected, in particular immediately after injection when the two miscible liquids of different refractive indices mix.

Table 4.1 Summary of the mixtures containing IrO_x NPs, water and ACN used in the experiments to study the influence of the "acidity regulator" and the concentration of the IrO_x NP catalyst on the kinetics responses. The "acidity regulator" stock concentrations were 400 mM $HClO_4$ or 86 mM $NaHCO_3/Na_2SiF_6$, leading to final concentrations of 20 mM $HClO_4$ or 4.3 mM $NaHCO_3/Na_2SiF_6$ in the samples analyzed, respectively. The IrO_x NP stock concentration was 0.62 mM.

Sample	Vol. "acidity regulator" / mL	Vol. IrO_x NPs / mL	Vol. water / mL	Vol. ACN / mL	$[IrO_x$ NP] / μM
(*i*)	0.400	0	0.400	1.2	0
(*ii*)	0.400	0.080	0.320	1.2	6.2
(*iii*)	0.400	0.160	0.240	1.2	12.4
(*iv*)	0.400	0.240	0.160	1.2	18.6
(*v*)	0.400	0.320	0.080	1.2	24.8
(*vi*)	0.400	0.400	0	1.2	31.0

The second set of kinetic data was obtained to highlight the influence of varying the water content (from 5 to 85 % (v/v)) in the water/ACN mixture on the rates of the WOR in the presence of 20 mM $HClO_4$ and 27 μM IrO_x NPs. Three distinct regimes were identified with water contents (*i*) between 5 and 25 % (v/v), *(ii)* between 35 and 50 % (v/v), and (*iii*) between 70 and 85 % (v/v). Each regime required a slightly modified experimental approach when preparing the samples for kinetics analysis.

(*i*) **Water content between 5 and 25 % (v/v).** These experiments were carried out in an analogous fashion to those previously described and explicitly show in the table 4.1, by modifying the proportion of the mixture containing the catalyst, as shown in the table 4.2.

Table 4.2 Summary of the mixtures containing IrO_x NPs, water and ACN used in the experiments to study the influence of the water content in the range 5 to 25 % (v/v). The IrO_x NP stock concentration was 0.62 mM. The final concentrations of $HClO_4$ and IrO_x NPs in the samples to be analyzed were 20 mM and 27 mM, respectively. *In this experiment the concentration of the acid solution was 3.2 M

Sample	Vol. 1 M $HClO_4$ / mL	Vol. water / mL	Vol. IrO_x NPs / mL	Vol ACN / mL	Water content /% (v/v)
(*i*)	0.050*	0	0.350	1.6	5%
(*ii*)	0.160	0.290	0.350	1.2	10%
(*iii*)	0.160	0.690	0.350	0.8	15%
(*iv*)	0.160	1.49	0.350	0	25%

(ii) Water content between 35 and 50 % (v/v). For these experiments, 1.0 mL of 4 mM $Ru^{II}(bpy)_3(PF_6)_3$ solution was placed in a quartz cell. Subsequently, 1.0 mL of a solution containing water, ACN, $HClO_4$ and IrO_x NPs was added and the absorbance at 673 nm and 900 nm recorded as a function of time. The mixtures were prepared as shown in the table 4.3.

Table 4.3 Summary of the mixtures containing IrO_x NPs, water and ACN used in the experiments to study the influence of the water content in the range 35 to 50 % (v/v). The IrO_x NP stock concentration was 0.62 mM. The final concentrations of $HClO_4$ and IrO_x NPs in the samples to be analyzed were 20 mM and 27 mM, respectively

Sample	Vol. 0.5 M $HClO_4$ / mL	Vol. water / mL	Vol. IrO_x NPs / mL	Vol ACN / mL	Water content /% (v/v)
(*v*)	0.160	1.065	0.175	0.6	35%
(*vi*)	0.160	1.665	0.175	0	50%

(iii) Water content between 70 and 85 % (v/v). For these experiments, a solution 2.67 mM $Ru^{II}(bpy)_3(PF_6)_3$ was dissolved in 26.67 mM $HClO_4$ prepared in water/ACN(13:2 (v/v)). As $[Ru^{III}(bpy)_3]^{3+}$ was found to be stable in acidic water-rich mixtures of water/ACN in the range of minutes, each solution was prepared immediately prior to analysis. 1.5 mL of the latter solution was placed in a quartz cell. Next, 0.5 mL of a solution containing water, ACN, and IrO_x NPs was added and the

absorbance at 673 nm and 900 nm recorded as a function of time. These mixtures were prepared as shown in the table 4.4

Table 4.4 Summary of the mixtures containing IrO_x NPs, water and ACN used in the experiments to study the influence of the water content in the range 70 to 85 % (v/v). The IrO_x NP stock concentration was 0.62 mM. The final concentrations of $HClO_4$ and IrO_x NPs in the samples to be analyzed were 20 mM and 27 mM, respectively

Sample	Vol. 0.5 M HClO$_4$ / mL	Vol. water / mL	Vol. IrO$_x$ NPs / mL	Vol ACN / mL	Water content /% (v/v)
(*vii*)	0.160	0.050	0.350	1.6	70%
(*viii*)	0.160	0.850	0.350	0.8	80%
(i*x*)	0.160	1.250	0.350	00.4	85%

4.2.3.2   Analysis of the products

The analysis of the products for the mixtures containing 10% water was carried out under identical conditions to those previously described but using a septum sealed cell. In this set of experiments the final concentration of IrO_x NPs was 31μM. At t = 0, a fixed amount of catalyst was injected to the cell. Once the time necessary for the completion of the reaction had elapsed both the liquid and the headspace were analyzed by ^{1}HNMR spectroscopy and Gas Chromatography respectively.

^{1}H NMR spectroscopy:

The liquid was analyzed by ^{1}H NMR in an NMR tube in a Bruker Biospin Avance-400 spectrometer. Chemical shifts were expressed in parts per million (ppm) relative to tetramethylsilane (TMS). The NMR spectra were acquired after the desired time for the reaction was reached. For these experiments, the water/ACN mixtures were prepared using D_2O and ACN-D_3.

Gas Chromatography:

The headspace of the vial was sampled using a syringe with a push-pull valve (SGE Analytical Sciences) and subsequently analyzed by gas chromatography using a Perkin-Elmer gas chromatograph (Clarus 500, equipped with 5 Å molecular sieves 80/100 mesh) with a thermal conductivity detector (TCD) and argon as the carrier gas. The quantitative determination of molecular oxygen (O_2) evolved from the samples was achieved in a similar manner to that reported in the Chapter 2, but taking into account that a significant ammout of O_2 is present in the solution. The number of moles of O_2 in the head space ($\eta_{O_{2(HS)}}$) was calculated from the percentage obtained according to the calibration curve ($\%O_2$, Figure 4.1, see below) as follows:

$$\eta_{O_{2(HS)}} = \left(\frac{\%O_2}{100 - \%O_2} \right) \left(\frac{P_{atm} \times V_{HS}}{R \times T} \right) \tag{4.1}$$

where P_{atm} is the atmospheric pressure, V_{HS} is the volume of the head space, T is the room temperature and R is the gas constant. Additionally, the number of moles of dissolved O_2 in solution ($\eta_{O_{2(Sol)}}$) was calculated using Henry's law as follows:

$$\eta_{O_{2(Sol)}} = V_{sol} \bullet P_{O_2} \bullet H \tag{4.2}$$

where P_{O2} is the partial pressure and H is Henry's constant. An approximate value of H was taken and assumed to be that of pure ACN (2.42×10^{-3} M·Pa^{-1}).[7] Assuming ideal gas behavior, the partial pressure of O_2 (P_{O_2}) can be expressed as:

$$P_{O_2} = \frac{\eta_{O_{2HS}} \bullet R \bullet T}{V_{HS}} \tag{4.3}$$

Finally, the total number of moles of O_2 evolved was calculated as the sum of $\eta_{O_{2(HS)}}$ and $\eta_{O_{2(Sol)}}$.
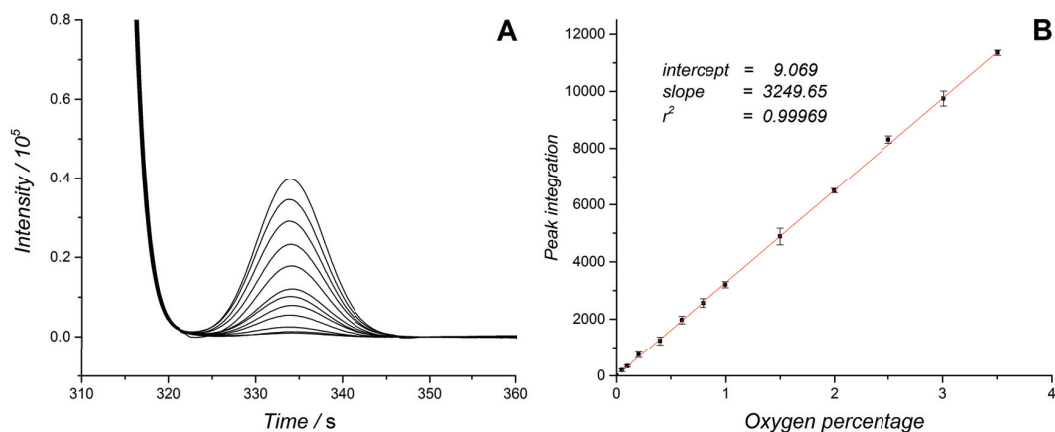

Figure 4.1 (A) Plot of GC data for gas samples with increasing concentrations of O_2 from bottom to top. **(B)** Calibration curve obtained by plotting the the area of the O_2 peak in the chromatogram *vs.* the fraction of O_2 in the head-space. Each point on the curve is the average of three measurements and the errors bars represent two times the standard deviation. Samples with differents amounts of O_2 were obtained by succesive dilution of an O_2 standard with N_2.

4.2.3.3   Electrochemical measurements

All electrochemical measurements in organic media were performed in a three-electrode configuration using a PGSTAT 30 potentiostat (Metrohm, CH). No iR compensation was applied to the cell. All voltammetry experiments were completed using organic media thoroughly de-gassed with nitrogen, under anaerobic conditions in a glovebox filled with nitrogen (O_2 < 1 ppm, H_2O < 1 ppm) and at an ambient temperature of 23 ± 2 ºC.

Bulk electrolysis experiments were carried out in water/ACN mixtures initially containing 2 mM $Ru^{II}(bpy)_3(PF_6)_2$, 0.1 M tetrabutylammonium hexafluorophosphate (TBAPF$_6$), 31μM IrO$_x$ NPs and 4.3 mM $NaHCO_3./Na_2SiF_6$. A classic bulk electrolysis cell configuration was employed using a Duocel® reticulated vitreous carbon working electrode (RVC, pores/inch = 30; relative density 3%, supplied by ERG Aerospace Corporation, U.S.A.), a Pt-mesh counter electrode and a Ag/Ag^+ double-junction organic reference electrode. The anodic and cathodic compartments were separated by a glass wool plug to prevent the re-oxidation of O_2 at the Pt-mesh counter electrode. Prior to experiments, RVC electrodes were cleaned by immersion

in ethanol for 20 min, followed by drying under a stream of nitrogen gas. RVC was chosen as the working electrode due to its large specific area, robust mechanical properties and high overpotential for the WOR compared to Pt under similar conditions. The gas products accumulated in the headspace of the electrolysis cell were sampled and analyzed by gas chromatography, as previously described.

4.2.3.4   Physicochemical characterization of the water/ACN mixtures

Infra-red (IR) spectroscopy.

Water/ACN mixtures tested by IR spectroscopy were prepared by mixing ACN with water containing 20 % D_2O. The O-D and C≡N stretching bands for HDO and ACN in the mixtures at various water mole fractions (X_{H_2O}) were measured at room temperature (25 °C) from 2000 to 3000 cm^{-1} on a Varian 800 FT-IR ATR Spectrometer.

Viscosity measurements.

Viscosity measurements were carried at room temperature (25°C) in a viscometer SV-A series, Stand Type A&D Company, limited.

4.3   Results and discussion

4.3.1 Characterization of the complexes

Transient cyclic voltammograms at a macroelectrode for 2.0 mM Ru(bpy)$_3$(PF$_6$)$_2$ Ru(bpy)$_3$(PF$_6$)$_3$ in dry acetonitrile (0.1M TBAPF$_6$) are shown in Figure 4.2 A. In both cases, the complexes give rise to the expected 4-electrochemically reversible redox processes, occurring essentially at the same potentials (E$_{Ox, 1}$ = 0.89 V, E$_{Red, 1}$ = -1.72 V, E$_{Red, 2}$ = -1.92 V, E$_{Red, 3}$ = -2.17 V vs Fc$^+$/Fc). The absence of extra peaks in the

CVs excludes the possibility of remaining free-ruthenium from the synthesis, which would manifest itself as extra redox signals between the processes labeled as $E_{Ox,\ 1}$ and $E_{Red,\ 1.}$

The UV/vis spectra of the pure complexes are shown in the figure 4.2 B. The UV Vis spectra of the $[Ru^{II}(bpy)_3]^{2+}$ exhibits a strong band at 451 nm assigned to the metal ligand charge transfer d$\rightarrow\pi$. On the other hand, the $[Ru^{III}(bpy)_3]^{3+}$ presents two bands bands, the first one at 420 nm and the second one at 673 nm. Taking into account the extinction coefficients of the two complexes and the overlapping between the bands of $[Ru^{II}(bpy)_3]^{2+}$ and $[Ru^{III}(bpy)_3]^{3+}$ in the region 400 – 500 nm, it is more suitable to follow the kinetics of $[Ru(bpy)_3]^{3+}$ reduction as the disappearance of the band at 673 nm rather than the appearance of the MLCT band at 451 nm.

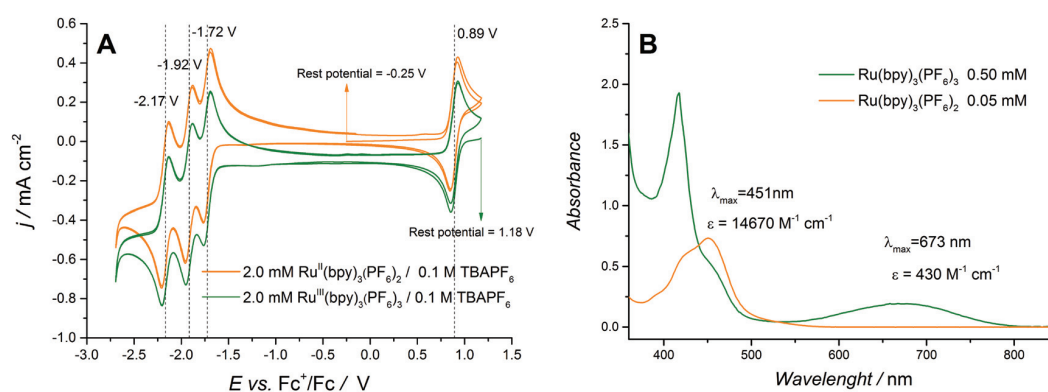**Figure 4.2 (A)** Cyclic voltammograms of 2 mM Ru(bpy)$_3$(PF$_6$)$_2$ and 2 mM Ru(bpy)$_3$(PF$_6$)$_3$ (containing 0.1 M tetrabutylammonium hexafluorophosphate (TBAPF$_6$) as supporting electrolyte) obtained with a glassy carbon electrode at a scan rate of 50 mVs^{-1}. The voltammetry was performed in dry ACN and under anaerobic conditions as described above. **(B)** UV/vis absorbance spectra of 0.05 mM Ru (bpy)$_3$(PF$_6$)$_2$ and 0.50 mM Ru(bpy)$_3$(PF$_6$)$_3$ in dry ACN.

4.3.2 Designing a model system for water oxidation in a non-aqueous environment.

Current state-of-the-art research to overcome the WOR "bottleneck" in water-splitting is dominated by the search for novel WOCs, either homogenous molecular or heterogeneous NP-based species and ideally consisting entirely of earth-abundant non-precious elements, that necessitate the lowest possible overpotential to achieve exceptionally fast catalytic rates. In this article, we deviate from this common approach and instead focus on improving the reactivity of the water molecules

themselves, by changing the reaction conditions under which the WOR takes place, and not on improving the reactivity of the catalyst. Thus, in designing these experiments, we chose the well-known bench-mark catalyst and oxidant combination of IrO_x NPs and $[Ru^{III}(bpy)_3]^{3+}$ to test the influence of the composition of the reaction media on the WOR catalytic rates.

As noted in detail *vide supra*, the reactivity of water molecules varies considerably in non-aqueous environments. We chose a primarily non-aqueous environment based on water/ACN mixtures as a large body of physicochemical[19,20] and spectroscopic data is available for this solvent system.[21-26] Additionally, ACN is an abundant solvent of low toxicity, is miscible with water in any proportion, has a wide polarizable potential window with an oxidative limit of > 2 V (vs. SHE)[27] and is thus stable in the presence of the powerful oxidant $[Ru^{III}(bpy)^3]^{3+}$.

$[Ru_{III}(bpy)_3]^{3+}$ is typically produced photochemically in situ, in order to act as an oxidant for the WOR in the presence of an appropriate catalyst, such as IrO_x NPs.[15,28,29] In the presence of light, $[Ru^{II}(bpy)_3]^{2+}$ is excited and the metal-to-ligand charge transfer (MLCT) excited state, $[Ru(bpy)_3]^{2+*}$, is formed. The latter is oxidatively quenched by a suitable sacrificial electron acceptor, such as persulfate $(S_2O_8^{2-})$, to produce $[Ru^{III}(bpy)_3]^{3+}$. In the presence of IrO_x NPs, the $[Ru^{III}(bpy)_3]^{3+}$ is reduced back to $[Ru^{II}(bpy)_3]^{2+}$ and O_2 is produced. Detailed kinetic studies of the WOR in aqueous media mediated by $[Ru^{III}(bpy)_3]^{3+}$ and catalyzed by IrO_x NPs were reported by Morris and coworkers in a $NaHCO_3/Na_2SiF_6$ buffer (pH 5.7).[30] The analysis of the kinetic data showed that the rate-determining step (RDS) in the process is electron transfer between $[Ru^{III}(bpy)_3]^{3+}$ and the surface Ir catalytic centers. In the present work, we have chemically synthesized $[Ru_{III}(bpy)_3]^{3+}$ as its hydrophobic PF_6 salt for direct use as a sacrificial oxidant. The advantages of this strategy in comparison to the aqueous photochemical approach were threefold: (i) it enabled us to carry out homogeneous kinetic measurements in hydrophobic ACN-rich media, (ii) the stability of $[Ru^{III}(bpy)_3]^{3+}$ in dry ACN is drastically improved compared to an aqueous solution (see Figure 4.3) and (iii) we avoided the complications associated with the use of $S_2O_8^{2-}$, namely its poor solubility in organic media and the presence of highly oxidizing intermediates (e.g., $SO^{4\cdot-}$) that may themselves promote the WOR and obscure the accurate determination of kinetic rate constants.
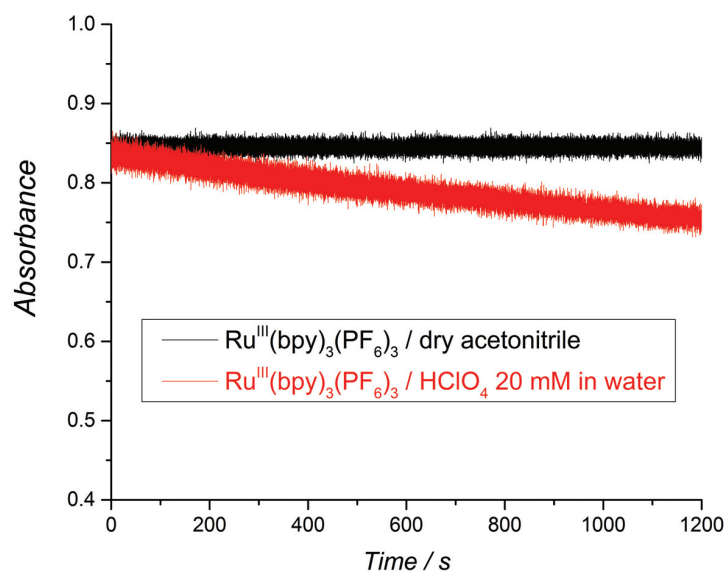
Figure 4.3. Real time absorbance measurements at 673 nm for 2 mM Ru(bpy)$_3$(PF$_6$)$_3$ dissolved in dry ACN and an aqueous solution of 20 mM HClO$_4$.

Before embarking on a detailed kinetic study, a simple preliminary experiment was devised to quickly test if water molecules were indeed more reactive in the primarily non-aqueous environment of the present model water/ACN system. The first step involved forming an immiscible biphasic water/ACN system by dissolving potassium chloride in the aqueous phase at a concentration of 1 M before contacting it with an equal volume of ACN. Upon vigorous stirring, a stable biphasic system was obtained with the less dense ACN-rich phase on top and the aqueous-rich phase at the bottom. Addition of a known amount of solid Ru^{III}(bpy)$_3$(PF$_6$)$_3$ (5 to 10 mg) to the resulting biphasic system in the absence of catalyst revealed a faster reduction of [Ru^{III}(bpy)$_3$]$^{3+}$ in the ACN-rich phase. This clear increase in reactivity was visible to the naked eye as the ACN-rich phase immediately turns orange whereas the aqueous-rich phase retained the green color of unreacted [Ru^{III}(bpy)$_3$]$^{3+}$ (inset Figure 4.4). The facile reduction of [Ru^{III}(bpy)$_3$]$^{3+}$ in the ACN-rich phase may be attributed to the WOR and perhaps, to an extent, by the co-evolution of Cl$_2$. Hence, this simple experiment provides a qualitative example of the increased reactivity of water molecules in an ACN-rich phase.
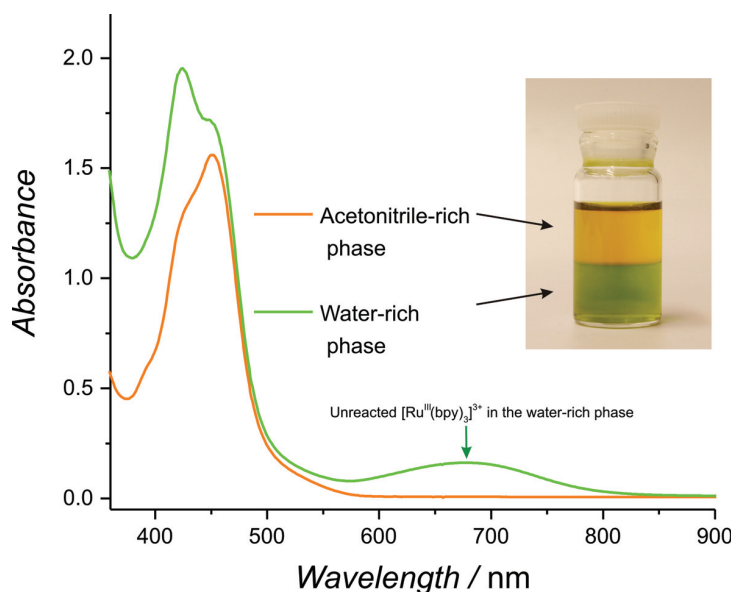
Figure 4.4 Highlighting the increased reactivity of water molecules in a non-aqueous environment. UV/vis spectra of both phases in a biphasic system composed of a water-rich phase (green in colour) and an organic-rich phase (orange in colour) after the addition of small amounts of $Ru^{III}(bpy)_3(PF_6)_3$

Consistent with these observations, UV/vis spectra of both phases taken after 1 min. of reaction (Figure 4.4) revealed a significant characteristic absorption band for unreacted $[Ru^{III}(bpy)_3]^{3+}$ at 673 nm in the water-rich (bottom) phase and its complete absence in the ACN-rich (top) phase. Even more strikingly, rapid and vigorous O_2 evolution was observed to occur preferentially in the organic phase.

4.3.3 Influence of "acidity regulators" and [IrO$_x$ NPs] on the kinetics of the WOR.

The preliminary experiment depicted in Figure 4.4 clearly shows that the WOR proceeds faster in the primarily non-aqueous water/ACN environment even in the absence of catalyst. Thus, initial kinetic experiments were designed to see if the reactivity of the water molecules with $[Ru^{III}(bpy)_3]^{3+}$ as the electron acceptor in the water/ACN mixture could be optimally tuned by introducing catalytic IrO$_x$ NPs and "acidity regulator" aqueous solutions of HClO$_4$ or NaHCO$_3$/Na$_2$SiF$_6$ (pH =5.7). Although the pH is difficult to control given the obvious difficulties in the evaluation of the activity coefficient of the proton, the weak basicity of ACN ensures that it is not directly protonated to form CH_3CNH^+ in water/ACN mixtures. Thus, in the event

of protons being introduced either by dissociation of a strong acid or released during the WOR, the solvation shell of the proton is practically in the form of $(H_2O)nH^+ \cdot ACN$.[13] Therefore, the aqueous buffer will still act as an acidity regulator in this mixed environment. The use of buffer is crucial since changes of the proton activity during the WOR significantly influence the thermodynamic driving force of the reaction, making analysis of the data rather complex A set of experiments highlighting the difficulty in obtaining meaningful kinetic data in the absence of buffer is shown in the figure 4.5 . The data clearly shows that in such conditions, no linear correlation exists between *ln[absorbance]* and time in the crucial interval between 0 to 5 s for kinetics analysis.
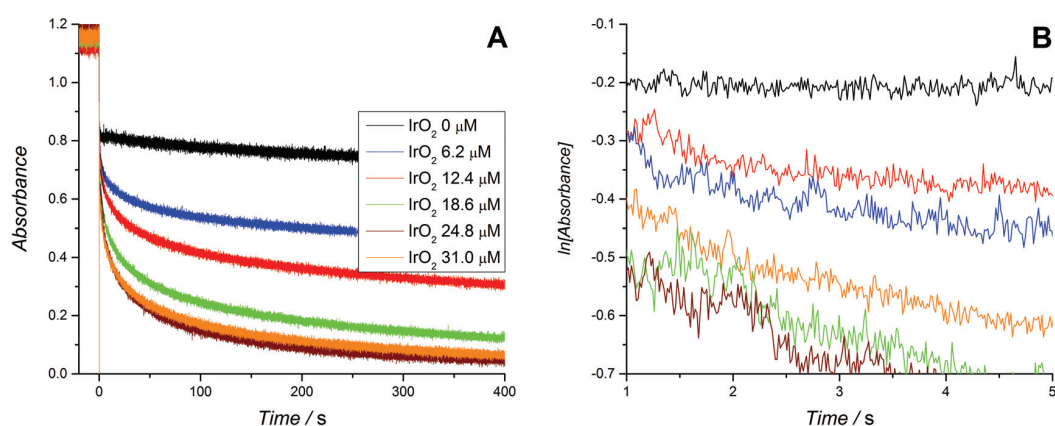

Figure 4.5 (A) Real time absorbance measurements for $[Ru^{III}(bpy)_3]^{3+}$ solutions after the addition of a mixture containing water, ACN and IrO_x NPs in different concentrations. The absorbance was plotted as the difference between the values at 673 nm and 900nm. The final content of water was 10 % (v/v). **(B)** Plots of ln[Absorbance] *vs.* time derived from the data in (A).

Figure 4.6 shows the corrected UV/vis absorbance profiles for the disappearance of the absorbance band at 673 nm for the two buffered systems, A ($HClO_4$) and B ($NaHCO_3/Na2SiF_6$), both without catalyst and in the presence of increasing concentrations of IrO_x NPs. As in the figure 4.5 B, the real time absorbance data was re-plotted on a logarithmic scale (Figures 4.6C ($HClO_4$) and 4.6D ($NaHCO_3/Na_2SiF_6$)) to obtain first-order rate constants. Linear trends were observed for both acidity regulators and at all IrO_x NP concentrations investigated up to 5 s after injecting the water/ACN mixture (containing IrO_x NPs and the acidity regulator) to the dry ACN solvent (containing $[Ru^{III}(bpy)_3]^{3+}$). Deviations from this linear behavior at longer time scales were attributed to significant changes in the acidity of the environment

due to the release of considerable quantities of protons during the WOR, causing a larger thermodynamic driving force required to overcome the WOR and slower rates of reaction in comparison to initial conditions.
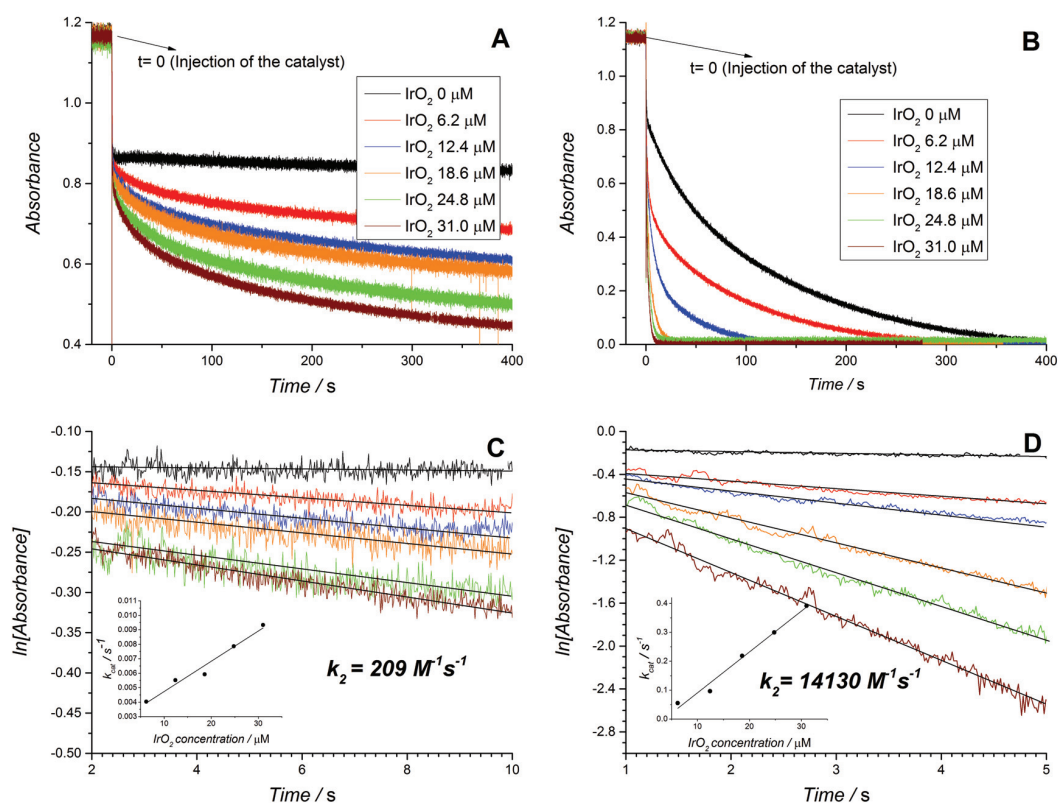

Figure 4.6 The influence of "acidity regulators". Real time absorbance measurements for $[Ru^{III}(bpy)_3]^{3+}$ solutions after the addition of a mixture containing water, acetonitrile, buffer, and IrO_x nanoparticles in different concentrations. The acidity regulators used were (A) 20 mM $HClO_4$ and (B) 4.3 mM $NaHCO_3/Na_2SiF_6$. In both cases the absorbances were plotted as the difference between the values at 673 nm and 900nm. The final content of water was 10 % (v/v). ln[Absorbance] *vs.* time plots derived from the data in (A) for 20 mM $HClO_4$ and (B) for 4.3 mM $NaHCO_3/Na_2SiF_6$ are shown in (C) and (D), respectively. The inset in each case represents the plot of the first order constant determined as the slope of the curve *vs.* the concentration of catalyst

Considering that water is always in large excess with respect to the electron donor, the rate law can be the expressed as:

$$\frac{\partial\left[Ru^{III}\left(bpy\right)_3^{3+}\right]}{\partial t} = k_{obs}\left[Ru^{III}\left(bpy\right)_3^{3+}\right] \qquad (4.4)$$

where k_{obs} represents the pseudo-first order constant obtained from the slope of the curves in Figures 4.6C and 4.6D. Interestingly, for experiments carried out with NaHCO$_3$/Na$_2$SiF$_6$, the reduction of $[Ru^{III}(bpy)_3]^{3+}$ occurred at comparable rates both in absence and presence of catalyst. Thus, k_{obs} was split into two different contributions, k_0 and k_{cat}, to independently determine, the rate constant for the $[Ru^{III}(bpy)_3]^{3+}$ reduction in the absence and presence of catalyst, respectively. k_0, the rate constant for the non-catalyzed consumption of $[Ru^{III}(bpy)_3]^{3+}$, was determined from the slope of the pseudo-first order plot in the absence of IrO$_x$ NPs. It therefore followed that $k_{cat} = k_{obs} - k_0$. Plots of k_{cat} versus the IrO$_x$ NP concentration for both acidity regulators (insets in Figures 4.6C and 4.6D) are linear indicating an explicit dependence of the rate on the concentration of catalyst as follows:

$$\frac{\partial\left[Ru^{III}\left(bpy\right)_3^{3+}\right]}{\partial t} = k_0\left[Ru^{III}\left(bpy\right)_3^{3+}\right] + k_{cat}\left[Ru^{III}\left(bpy\right)_3^{3+}\right]$$
$$= k_0\left[Ru^{III}\left(bpy\right)_3^{3+}\right] + k_2\left[Ru^{III}\left(bpy\right)_3^{3+}\right]\left[IrO_2\right] \qquad (4.5)$$

where k_2 represents the pseudo-second order constant for the catalyzed WOR.

A number of clear trends emerge on inspection of the kinetic data extracted from Figure 4.6 and summarized in Table 4.6. Firstly, higher rates of reaction were observed when NaHCO$_3$/Na$_2$SiF$_6$ was used as the acidity regulator, both in the absence and presence of IrO$_x$ NPs, in comparison to those obtained with HClO$_4$. The former trend without catalysis is solely due to the higher thermodynamic driving force required to oxidize water in the presence of higher HClO$_4$ concentrations. Meanwhile, the latter trend with catalysis is additionally influenced by the pH dependent redox properties of the IrO$_x$ NP surface active sites.[31-33] Indeed, although the conditions of the

NaHCO$_3$/Na$_2$SiF$_6$ buffered WOR studied by Morris *et al.* are different to those discussed herein, in terms of reaction-media composition and [Ru^{III}(bpy)$_3$]$^{3+}$ concentration, the magnitude order of the rate constants between both studies were identical, giving credibility to our obtained values.[30] Secondly, a linear relationship exists between the [IrO$_x$ NPs] and the observed rates of catalysis with both buffering systems, supporting the bimolecular nature of the mechanism under the present conditions (equation 4.5).

In addition to the rates of catalysis, another key attribute of a water oxidation system is the stability of the redox acceptor. Ghosh *et al.* have reported that in the absence of a catalyst the reduction of [Ru^{III}(bpy)$_3$]$^{3+}$ in water yields negligible amounts of O$_2$ or H$_2$O$_2$. This observation was attributed to the irreversible degradation of the [Ru^{III}(bpy)$_3$]$^{3+}$ into a variety of products including several Ru complexes and CO$_2$.[34] Similar results were found herein, with no O$_2$ detected by gas chromatography. Efforts to detect H$_2$O$_2$ by the well-known starch-iodine method were hampered by the poor solubility of the reagents in the ACN/water mixture. Thus, although very low amounts of H$_2$O$_2$ were detected, the results were irreproducible and not reliable.

Table 4.5 Summary of the kinetic data extracted from figure 2.

System	k_0 / 10^{-4} s^{-1}	[IrO$_x$] / μM	k_{cat} / 10^{-3} M^{-1} s^{-1}	k_2 / M^{-1} s^{-1}
HClO$_4$	7	6.2	4.0	209
		12.4	5.5	
		18.6	5.9	
		24.8	7.9	
		31.0	9.3	
NaHCO$_3$/ Na$_2$SiF$_6$	154	6.2	55.1	14130
		12.4	96.5	
		18.6	218.6	
		24.8	299.6	
		31.0	391.6	

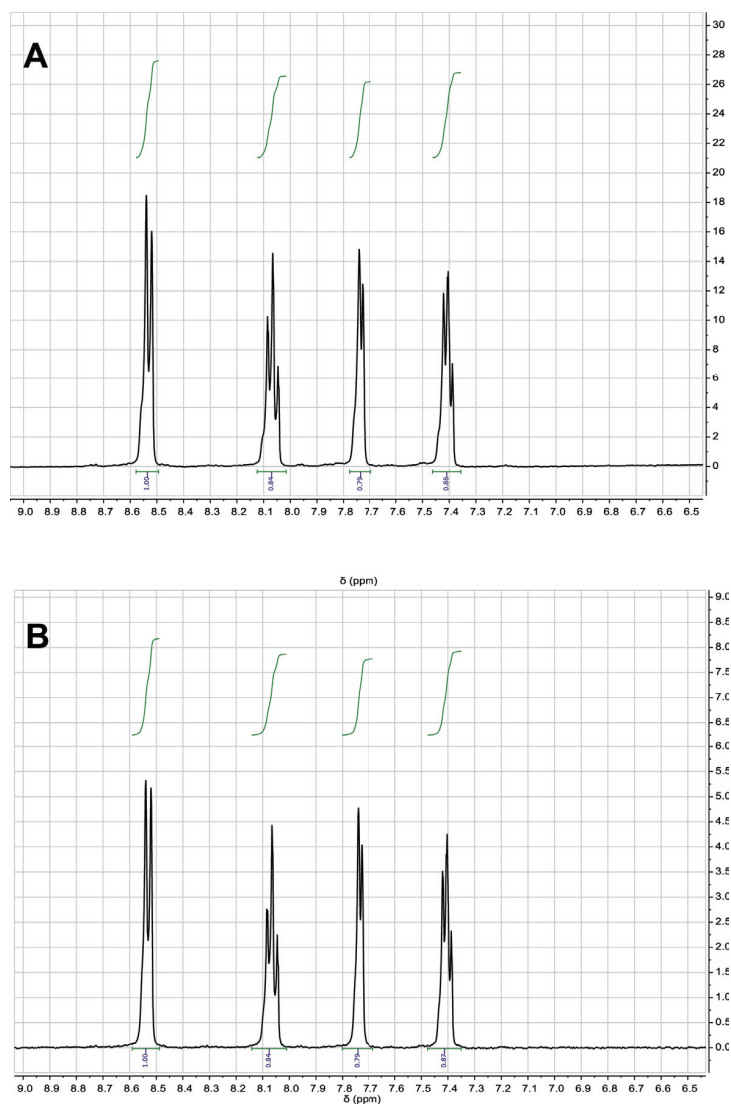**Figure 4.7** ^{1}H NMR spectrum for a sample of Ru(bpy)$_3$(bpy)$_3$(PF$_6$)$_3$ recorded after 30 minutes of reaction in (A) the absence and (B) the presence of catalyst (31 μM IrO$_x$ NPs). The other experimental conditions were identical to those described in Figure 4.6 B *i.e.,* the sample contained 2 mM Ru(bpy)$_3$(PF$_6$)$_3$, and 4.3 mM NaHCO$_3$/Na$_2$SiF$_6$ buffer in a water/ACN-D$_3$ mixture containing 10 % (v/v) of water. In both cases completion of the reaction is achieved, as traces of [Ru^{III}(bpy)$_3$]$^{3+}$ would not allow the observation of the peaks in the spectrum.

However, unlike previous reports, irreversible degradation of [Ru^{III}(bpy)$_3$]$^{3+}$ was not observed by ^{1}H NMR spectroscopy. In the presence of catalyst (31μM) and NaHCO$_3$/Na$_2$SiF$_6$ buffer, the yield of O$_2$ was 61% based on the initial amount of [Ru^{III}(bpy)$_3$]$^{3+}$ present. Once more, in the presence of catalyst, no degradation of [Ru^{III}(bpy)$_3$]$^{3+}$ was observed by ^{1}H NMR spectroscopy. Figure 4.7 shows the NMR spectra for the samples after 30 minutes of reaction in the conditions previously described (NaHCO$_3$/Na$_2$SiF$_6$ buffer in water/ACN-D3

mixture containing 10 % (v/v)) of water.) in the absence and the presence of the catalyst (31uM). In both cases a clean pattern in the aromatic region clearly suggests the absence of degradation products. Decomposition of $[Ru(bpy)_3]^{3+}$ would manifest itself as the presence of a complex pattern as reported by Ghosh *et al.* [34]

Tentatively, non-catalyzed reduction of $[Ru^{III}(bpy)_3]^{3+}$ may take place with concomitant oxidation of the buffer species, thus explaining the non-stoichiometric evolution of O_2 even in the presence of catalyst. The absence of degradation products both with and without catalyst is noteworthy since many of the practical difficulties associated with the use of $[Ru^{III}(bpy)_3]^{3+}$ are related to its degradation over extended periods of time.

4.3.4 Influence of the water content on the kinetics of the WOR in a non-aqueous environment

A second series of kinetic studies were performed to elucidate the optimal water content in the water/ACN mixtures to achieve the fastest WOR kinetic rates in the presence of 27 μM IrO_x NPs and $HClO_4$ as the acidity regulator. $HClO_4$ was chosen in preference to $NaHCO_3/Na_2SiF_6$ as (*i*) its slower base rate of catalysis was favored to experimentally observe clear changes in the kinetic rate constants, (*ii*) the experimental design necessitated the preparation of $[Ru^{III}(bpy)_3]^{3+}$ in an aqueous solution, *i.e.,* at large water contents of 70 to 85 % (v/v), and $HClO_4$ provided an acidic environment where $[Ru^{III}(bpy)_3]^{3+}$ was stable for a few minutes (see figure 4.3).

The influence of the water content in the water/ACN mixture on the normalized second order rate constant k_2 (see Equation 4.5) is shown in Figure 4.8. The observed trend may be divided into three distinct regions of water mole fractions (X_{H_2O}): (*i*) a water-rich region ($0.8 \leq X_{H_2O} \leq 0.95$), (*ii*) a region consisting of water/ACN micro-heterogeneities or micro-domains ($0.4 \leq X_{H_2O} \leq 0.8$) and (*iii*) an ACN-rich region ($0.1 \leq X_{H_2O} \leq 0.4$).
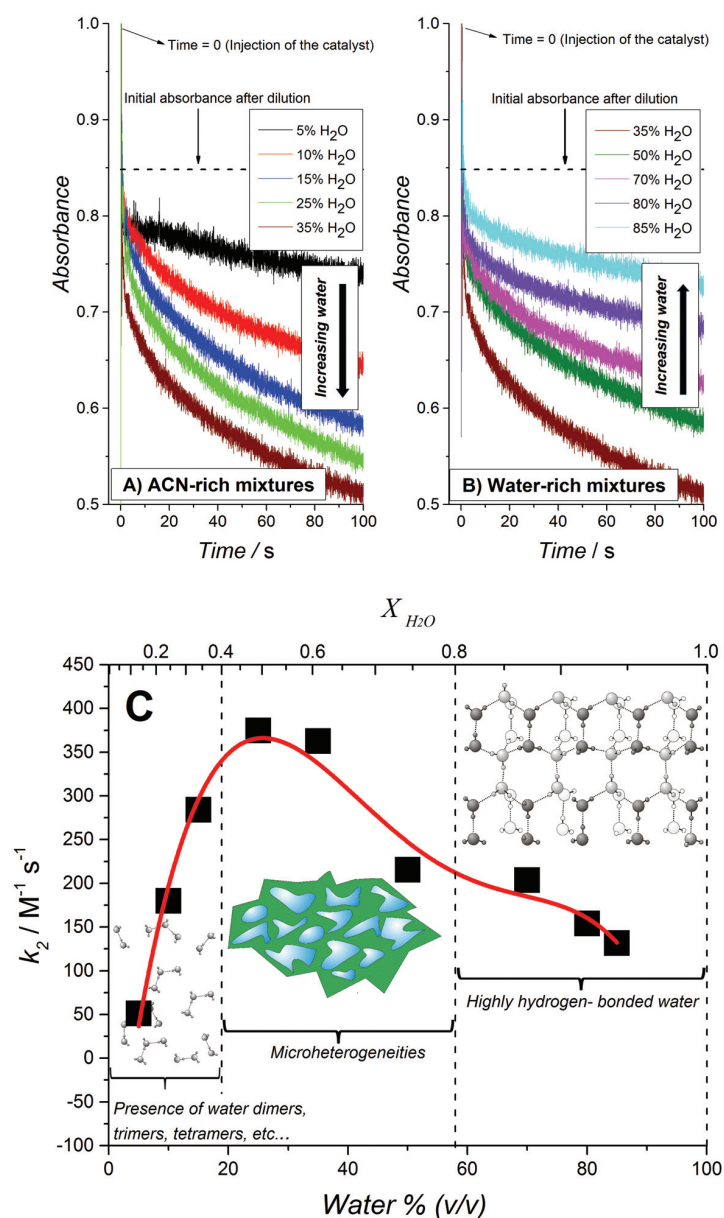
Figure 4.8 The influence of water content in the biphasic mixture. (A, B) Real time absorbance measurements for $[Ru^{III}(bpy)_3]^{3+}$ solutions after the addition of a mixture containing water, acetonitrile, $HClO_4$ IrO_x nanoparticles. The final concentration of water was varied in each experiment and the concentrations of $HClO_4$ and IrO_x were fixed at 20 mM and 27μM, respectively. (C) Normalized second order constant (k_2) for $[Ru^{III}(bpy)_3]^{3+}$ reduction *vs.* the total content of water expressed both as water percentage (v/v) and water mole fraction (X_{H_2O}).

The term micro-heterogeneity refers to the situation where molecules of the solvent, in this case water and/or ACN, are preferentially surrounded by molecules of their own kind. Thus, in this region, reported by Takamuku *et al.* to extend over the range $0.4 \leq X_{H_2O} \leq 0.8$,[26] both water and ACN clusters co-exist in the mixture. The observed trend in Figure 4.8 indicates that the rate of

the WOR is slow in the water-rich region, progressively increases until $X_{H_2O} \approx$ 0.7 and then rapidly increases to a maximum in the micro-heterogeneity region. Finally, in the ACN-rich region the rate rapidly declines in a linear fashion from the peak rate reached at $X_{H_2O} = 0.5$.

The initial progressive increase in the rate of the WOR with decreasing X_{H_2O} is attributed to a gradual decrease in the strength of the hydrogen-bonding network with increasing ACN content, as previously postulated for water molecules dissolved in ionic liquids.[8,9,14] X-ray diffraction and infra-red (IR) spectroscopy studies of water/ACN mixtures by Takamuku *et al.* revealed that the strong hydrogen-bond network begins to gradually degrade on the introduction of ACN, this process rapidly accelerates at $X_{H_2O} \approx 0.7$ (mirroring the rapid increase in rate observed experimentally in Figure 4.8) and the hydrogen-bond network essentially disappears and the water molecules are present in their "free" state, free of self-aggregation, in the range $0.2 \leq X_{H_2O} \leq 0.4$. The removal of the water-water H-bonds diminishes the "protection" of the water molecules and increases the susceptibility of the O-atom in water to interact with the catalytically active iridium species at the surface of the IrO_x NPs. The subsequent rapid linear decrease in the rate of the WOR in the ACN-rich region ($0.1 \leq X_{H_2O} \leq 0.4$) may be initially surprising as one would expect that the "free" water molecules in this regime would be the most reactive.

Takamuku *et al.* reported that the electron donicity and acceptability properties of water/ACN mixtures, measured as the ability to solvate the $VO(acac)_2$ complex[26] (D coefficient), decreases monotonically from pure water to pure ACN showing two inflection points, one of them at low water concentrations ($X_{H_2O} = 0.2$). As water has a larger acceptor number (54.8) than ACN (19.3), the D coefficient value reflects the solvation ability by water rather than ACN molecules. In other words, the ability of water to scavenge protons at low molar fractions is decreased even though the O-atom is "more free" to participate in the oxygen transfer step needed to carry out water oxidation. This results in a bell-shaped dependence of the rate of water oxidation with varying X_{H_2O}, as observed in Figure 4.8.

Control IR spectroscopy experiments were performed in an identical manner to those described by Takamuku *et al.* but incorporating the diverse additional species

present in the water/ACN mixtures during kinetic experiments for the WOR, namely, sensitizer molecules $(Ru(bpy)_3(PF_6)_2)$, acid $(HClO_4)$ and heterogeneous catalytic species $(IrO_x$ NPs), as outlined in Figure 4.8. The purpose of these control experiments is to eliminate the possibility that these augmented experimental conditions may invalidate our comparative analysis presented in the main text, between the kinetic data in Figure 4.8 and the data obtained by Takamuku *et al.*, in an unforeseen manner.

The spectroscopic study was carried out using water/ACN mixtures at various water mole fractions (X_{H_2O}), each of them prepared with water containing 20% of D_2O. The premise of the study was to monitor wavenumber shifts as a function of X_{H_2O} in water/ACN mixtures of the (i) O-D stretching mode of HDO, reflecting the extent of the formation of the water-water hydrogen bond network, and (ii) C≡N stretching mode, reflecting the extent of the formation of hydrogen bonds between ACN and water molecules.

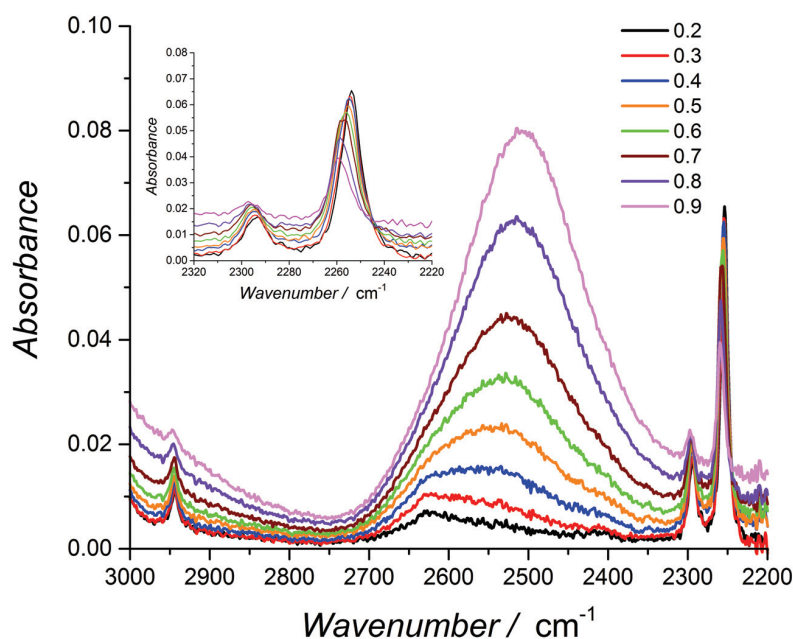**Figure 4.9** Infra-red (IR) absorption spectra of water/ACN mixtures as a function of increasing water mole fraction (X_{H_2O}) from $X_{H_2O} = 0.2$ to 0.9. The water contains 20 % D_2O. The concentrations of $Ru(bpy)_3(PF_6)_2$, $HClO_4$ and IrO_x NPs in each ACN/water mixture were fixed at 2 mM, 20 mM and 27 μM, respectively.

IR spectroscopic data was obtained over the wavenumber range 2200-3000 cm^{-1} for water/ACN mixtures containing all of the additional species noted *vide supra* and

as a function of increasing X_{H_2O}, with water containing 20 % D_2O (Figure 4.9). The chosen values of X_{H_2O} directly compare with those reported by Takamuku *et al.* to facilitate ease of comparison between the two data sets. Three bands appear in the studied region of the IR spectrum, the major one at 2500-2640 cm^{-1} is attributed to the O-D stretching mode, while the other two sharper bands at 2257 and 2295 cm^{-1} arise from the C≡N stretching mode and a combination of both CH$_3$ bending and C-C stretching in ACN, respectively.[23]
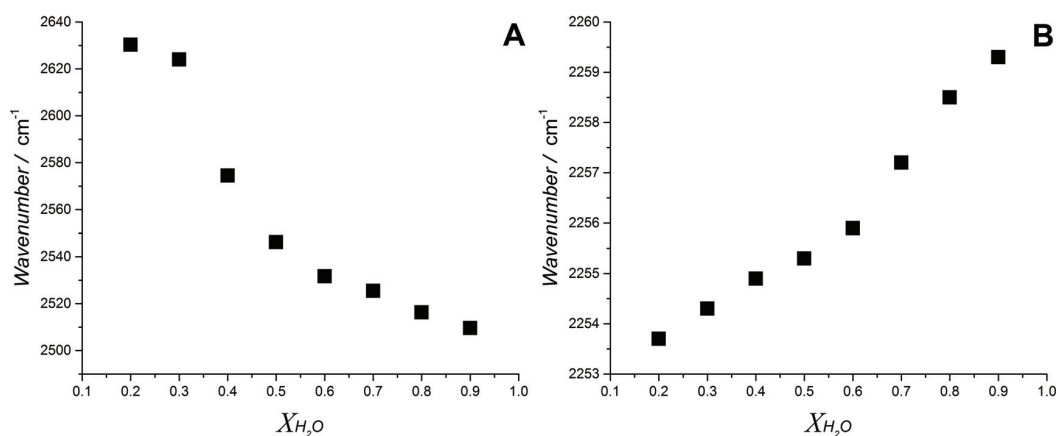

Figure 4.10 Wavenumbers for **(A)** the O-D stretching mode and **(B)** the C≡N stretching mode as a function of increasing water mole fraction (X_{H_2O}) from X_{H_2O} = 0.2 to 0.9. The water contains 20 % D_2O. The concentrations of Ru(bpy)$_3$(PF$_6$)$_2$, HClO$_4$ and IrO$_x$ NPs in each ACN/water mixture were fixed at 2 mM, 20 mM and 27 μM, respectively.

The wavenumbers of the O-D and C≡N stretching modes as a function of X_{H_2O} were plotted in Figures 4.10 (A) and (B). The following broad trends were observed as X_{H_2O} increases: (i) the wavenumber of the the O-D stretching mode decreases and (ii) the wavenumber of the C≡N stretching mode increases. The former trend is due to the progressive weakening of the O-D bond as the strength of the hydrogen-bonding network increases with increasing X_{H_2O}. In particular, the wavenumber sharply decreases with increasing X_{H_2O} from $X_{H_2O} \approx 0.3$ to 0.6, directly in line with the trend seen by Takamuku *et al.* both from their IR spectroscopic and XRD analysis. The C≡N stretching mode may be de-convoluted into two Lorentzians, one at lower wavenumbers assigned to free ACN molecules (as it only appears in pure ACN solvent) and one at slightly higher wavenumbers attributed to hydrogen-bonded ACN molecules (as it only appears in water/ACN mixtures). Whereas the wavenumbers of these Lorentzians do not vary significantly with increasing X_{H_2O}, their relative

117

intensities do change, producing the observed shift in the wavenumber of the C≡N stretching mode. Thus, as X_{H_2O} increases from $X_{H_2O} \approx 0.2$ to 0.9, the amount of hydrogen-bonded ACN molecules rapidly increases and the Lorentzian at higher wavenumbers increases in intensity. The latter is seen as an increase in wavenumber of the C≡N stretching mode, again directly in line with the trend seen by Takamuku *et al.* from their IR spectroscopic analysis.

Thus, the general conclusion from these control experiments is that we can replicate the trends observed by Takamuku *et al.* with the additional species present and that our comparative analysis in the main text is validated.

Concerning the interaction of the IrO_x NPs with water in the mixed solvent media, we propose that water interacts preferentially with the IrO_x surface. We base our hypothesis on the experimental observation that at water contents below 10% and $[IrO_x] > 60$ mM, the catalytic NPs aggregate and precipitate. This behavior is indicative of reduced NP stability at low water content. It also indicates that water, besides being the reagent for the WOR, suppresses aggregation of IrO_x NPs due to its preferential interaction with the NP surface.

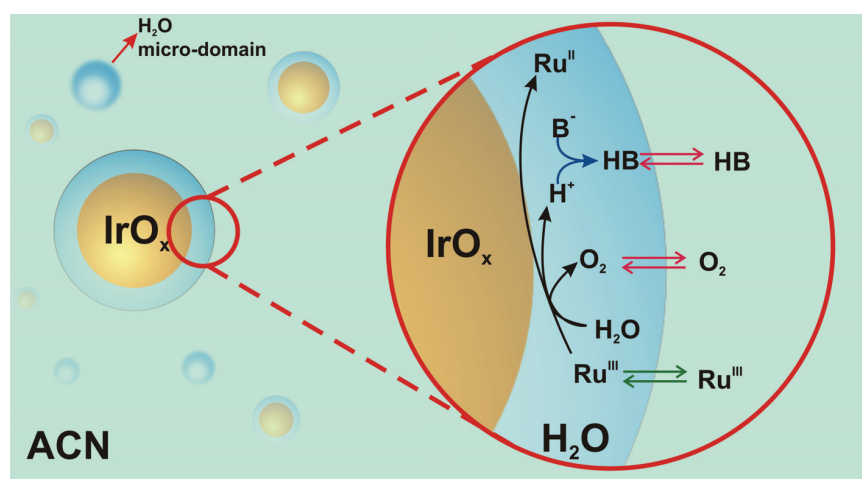**Figure 4.11** Proposed formation of reactive water overlayers on IrO_x nanoparticles. Ru^{III} = $[Ru^{III}(bpy)_3]^{3+}$, Ru^{II} = $[Ru^{II}(bpy)_3]^{2+}$ and B^- = proton acceptor species (in the absence of any additional basic specie $B = H_2O$)

As a result, reactive weakly hydrogen-bonded water micro-domains are brought in direct contact with IrO_x NPs and stabilize the catalytic NPs (Figure 4.11). Upon

addition of $[Ru^{III}(bpy)_3]^{3+}$ dissolved in ACN, it will partition across the interface formed between the water-rich domain at the NP surface and the ACN-rich bulk phase. Following its partition, the electron acceptor will diffuse into the water-rich overlayer, reach the surface of the catalytic NP and undergo electron-transfer to produce $[Ru^{II}(bpy)_3]^{2+}$ and oxidized Ir centers. Concomitant water oxidation occurs at the IrO_x NP producing O_2 and protons. O_2, being neutral and more soluble in ACN will rapidly partition to the organic-rich phase. The importance of proton acceptor species (B in Figure 4.11) is also a crucial factor in the WOR kinetics, as B will interact with protons, probably in a concerted way with the electron transfer process, to form HB. Partition of ionic species (*e.g.,* $[Ru^{III}(bpy)_3]^{3+}$) across the interface formed between the two liquid phases can in turn lead to the polarization of this liquid-liquid interface. The effect of the polarization herein proposed requires further study, and may provide other parameter to drive the reaction.

4.3.5 Continuous electrocatalytic O_2 evolution in water/ACN mixtures with $[Ru^{II}(bpy)_3]^{2+}$ as a redox shuttle.

The robust nature of the electrocatalytic WOR in non-aqueous conditions was probed by bulk electrolysis experiments whereby the WOR was catalyzed by colloidal IrO_x NPs suspended in solution, and $[Ru^{II}(bpy)_3]^{2+}$ acted as a recyclable redox shuttle transferring electrons from the surface of the electrode to the IrO_x NPs, whereupon they were used to drive the WOR.

The optimal potential at which to carry out bulk electrolysis was determined from cyclic voltammograms of 2 mM $[Ru^{II}(bpy)_3]^{2+}$ at two different water contents (10 % and 25 % (v/v)) and in the presence of IrO_x NPs. Figure 4.12 shows a representative voltammetric profile, where a quasi-reversible voltammetric wave corresponding to the $[Ru^{III}(bpy)_3]^{3+}/[Ru^{II}(bpy)_3]^{2+}$ redox couple was observed at ~0.9 V (*vs.* Fc^+/Fc). The considerable *i*R drop present due to the electrolysis cell design leads to the observation of a broad wave rather than a sharp peak for the anodic response. Thus, all bulk electrolysis experiments were conducted at a potential 400 mV more positive than the less-distorted cathodic peak of the $[Ru^{III}(bpy)_3]^{3+}/[Ru^{II}(bpy)_3]^{2+}$ redox couple.

Representative current-time and charge-time bulk electrolysis profiles are shown in Figure 4.13 A progressive decrease in the current was observed due to the change

in the pH-dependent thermodynamic driving force with the continuous release of protons during the WOR (shown for the catalyzed reaction w). In the presence of IrO_x NPs and 10 % or 25 % (v/v) water, a non-negligible current at long time scales (> 1000 s) was observed. This behavior is characteristic of a catalytic reaction, in which the redox shuttle is continuously recycled at the electrode surface (see inset Figure 4.13), leading to a sustained increase in the amount of charge passed with 25 % (v/v) water as the black trace in Figure 4; data for 10 % (v/v) water not shown. By comparison, however, a plateau of charge passed is reached once all of the $[Ru^{II}(bpy)_3]^{2+}$ is oxidized at the electrode surface in the absence of a recycling mechanism when the experiment was performed in dry ACN and in the absence of catalyst (blue dotted line, Figure 4.13).

Figure 4.12 CV of a solution containing 2 mM Ru(bpy)$_3$(PF$_6$)$_2$, 31 μM IrO$_x$ NPs and 4.3 mM NaHCO$_3$/Na$_2$SiF$_6$ buffer in a water/ACN mixture (2.5:7.5 (v/v)).

Finally, a further control experiment was performed to ensure that the extent of the direct WOR at the electrode surface during bulk electrolysis in the absence of both the $[Ru^{III}(bpy)]^{3+}/[Ru^{II}(bpy)]^{2+}$ redox shuttle and catalytic IrO_x NPs is minimal. Figure 4.14 shows comparative analysis of the currents and charge plots generated during bulk electrolysis of water/ACN mixtures (2.5/7.5 (v/v)) both the in the presence and absence of Ru(bpy)$_3$(PF$_6$)$_2$ and IrO_x NPs. The minimal contribution of direct water

120

oxidation at the electrode surface is clearly highlighted by the relatively low charge passed after 1100 s of bulk electrolysis in the absence ($\approx$ 0.5 C) compared to the presence ($\approx$ 4.3 C) of both the $[Ru^{III}]/[Ru^{II}]$ redox shuttle and catalytic IrO_x NPs. Thus, under the precise experimental conditions described in Figure the 4.14, the contribution of direct water oxidation at the electrode surface electrode is $\approx$11%.

Figure 4.13 Plots of the current (black line) and charge (blue line) during bulk electrolysis of a solution containing 2 mM $Ru(bpy)_3(PF_6)_2$, 31 μM IrO_x NPs and 4.3 mM buffer $NaHCO_3/Na_2SiF_6$, in an water/ACN mixture (2.5:7.5 (v/v)). For comparison, the plot of charge during bulk electrolysis of 2 mM $Ru(bpy)_3(PF_6)_2$ (blue dotted line) in dry acetonitrile was included. In each case the supporting electrolyte was 0.1 M $TBAPF_6$. The electrode was RVC (for details see experimental section).

Analysis of the effect of water content on the kinetics of the WOR measured by chronoamperometry is rather complex due to the large changes in viscosity as the water/ACN ratio increases (Figure 4.15). However, the values of O_2 measured under recycling conditions were found to be dependent on the water content. Table 4.7 shows the Faradaic efficiency, determined as a function of water content, as well as the O_2 yield for the chemical reduction of $[Ru^{III}(bpy)_3]^{3+}$ under the same experimental conditions. With 10 % (v/v) water present, the yields of O_2 evolved obtained by both chemical reduction and electrochemical reduction are essentially the same. Nonetheless, as the water content is increased to 25 % (v/v), the yields of O_2 evolved via chemical reduction and bulk electrolysis deviated by 10 %. This difference is attributed to faster degradation of the redox shuttle upon electrochemical cycling as the water content increases.
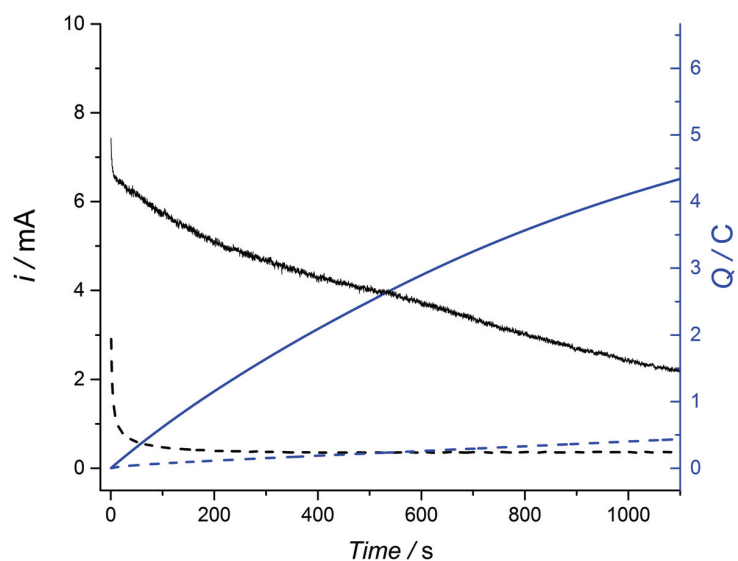
Figure 4.14 Control experiment: monitoring the extent of direct water oxidation at the electrode surface. The currents (blac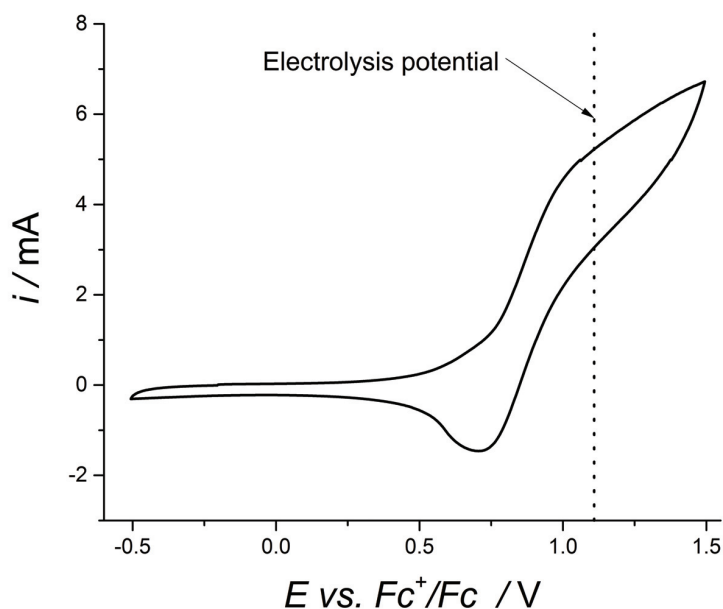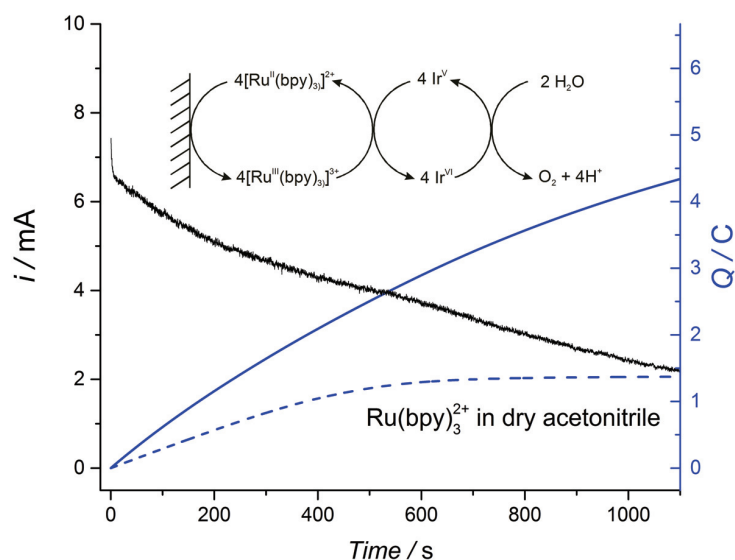k lines) and charge (blue lines) passed during bulk electrolysis of a solution containing 2 mM $Ru(bpy)_3(PF_6)_2$, 31 mM IrO_x NPs and 4.3 mM $NaHCO_3/Na_2SiF_6$ buffer in a water/ACN mixture (2.5:7.5 (v/v)) are plotted and compared with the currents (dashed black line) and charge (dashed blue line) passed during bulk electrolysis in the absence of $Ru(bpy)_3(PF_6)_2$ and IrO_x NPs, under otherwise identical experimental conditions.
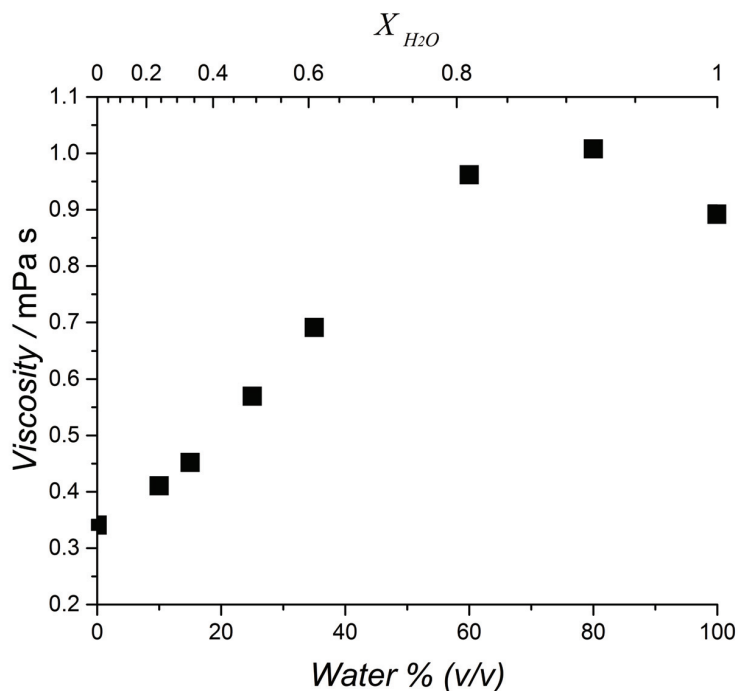
Figure 4.15. Viscosity of water/ACN mixtures at 25°C as a function of varying water content.

Table 4.7 Summary of the O_2 yields for chemical reduction and bulk electrolysis experiments.

Water content /% (v/v)	Yield chemical oxidation /%	Bulk Electrolysis	
		Charge (Q) /C	Faradic Efficiency / %
10	61	4.05	63
25	64	4.34	55

4.4 Conclusions

The present results clearly demonstrate that IrO_x-catalyzed water oxidation is dependent on the water content for water/acetonitrile mixtures. Based on kinetic measurements, the maximum activity for the catalyst in acidic media was exhibited when the biphasic media was composed of approximately equimolar proportions of water and acetonitrile. Under such experimental conditions hydrogen bonding is weakened and isolated reactive pools of water are generated. Formation of reactive water overlayers on the surface of IrO_x NPs is also proposed. All in all, the present strategy represents a better approach to characterize the catalytic activities of water oxidation catalysts in organic media that could be applied to a wide range of catalysts and organic solvents. On the other hand, the use of water/acetonitrile mixtures appears a viable alternative to enhance the stability of redox shuttles, a fundamental problem in photocatalytic water oxidation systems in general.

4.5 Bibliography

[1]   Yamazaki, H.; Shouji, A.; Kajita, M.; Yagi, M. *Coordination Chemistry Reviews* 254, (**2010**), 2483-2491.

[2]   Robinson, D. M.; Go, Y. B.; Greenblatt, M.; Dismukes, G. C. *Journal of the American Chemical Society* 132, (**2010**), 11467-11469.

[3]   Hongthani, W.; Fermín, D. J. *Diamond and Related Materials* 19, (**2010**), 680-684.

[4]   Zong, R.; Thummel, R. P. *Journal of the American Chemical Society* 127, (**2005**), 12802-12803.

[5]   Concepcion, J. J.; Jurss, J. W.; Templeton, J. L.; Meyer, T. J. *Journal of the American Chemical Society* 130, (**2008**), 16462-16463.

[6]   Chen, Z.; Concepcion, J. J.; Luo, H.; Hull, J. F.; Paul, A.; Meyer, T. J. *Journal of the American Chemical Society* 132, (**2010**), 17670-17673.

[7]   Coggins, M. K.; Zhang, M.-T.; Vannucci, A. K.; Dares, C. J.; Meyer, T. J. *Journal of the American Chemical Society* 136, (**2014**), 5531-5534.

[8]   Zhao, C.; Bond, A. M. *Journal of the American Chemical Society* 131, (**2009**), 4279-4287.

[9]   Bernardini, G.; Zhao, C.; Wedd, A. G.; Bond, A. M. *Inorganic Chemistry* 50, (**2011**), 5899-5909.

[10]   Holzwarth, A. R.; Müller, M. G.; Reus, M.; Nowaczyk, M.; Sander, J.; Rögner, M. *Proceedings of the National Academy of Sciences* 103, (**2006**), 6895-6900.

[11]   Renger, G.; Renger, T. *Photosynthesis Research* 98, (**2008**), 53-80.

[12]   Liu, Y.; Guo, S.-X.; Bond, A. M.; Zhang, J.; Du, S. *Electrochimica Acta* 101, (**2013**), 201-208.

[13]   Kalish, N. B.-M.; Shandalov, E.; Kharlanov, V.; Pines, D.; Pines, E. *The Journal of Physical Chemistry A* 115, (**2011**), 4063-4075.

[14]   Bernardini, G.; Wedd, A. G.; Zhao, C.; Bond, A. M. *Proceedings of the National Academy of Sciences* 109, (**2012**), 11552-11557.

[15]   Hara, M.; Waraksa, C. C.; Lean, J. T.; Lewis, B. A.; Mallouk, T. E. *The Journal of Physical Chemistry A* 104, (**2000**), 5275-5280.

[16]   Ji, Z.; Huang, S. D.; Guadalupe, A. R. *Inorganica Chimica Acta* 305, (**2000)**, 127-134.

[17]   Biner, M.; Buergi, H. B.; Ludi, A.; Roehr, C. *Journal of the American Chemical Society* 114, (**1992**), 5197-5203.

[18]   DeSimone, R. E.; Drago, R. S. *Journal of the American Chemical Society* 92, (**1970)**, 2343-2352.

[19]   Moreau, C.; Douhéret, G. *Thermochimica Acta* 13, (**1975)**, 385-392.

[20]   Villamanan, M. A.; Van Ness, H. C. *Journal of Chemical & Engineering Data* 30, (**1985)**, 445-446.

[21]   Von Goldammer, E.; Hertz, H. G. *The Journal of Physical Chemistry* 74, (**1970)**, 3734-3755.

[22]   Kovacs, H.; Laaksonen, A. *Journal of the American Chemical Society* 113, (**1991)**, 5596-5605.

[23]   Jamroz, D.; Stangret, J.; Lindgren, J. *Journal of the American Chemical Society* 115, (**1993)**, 6165-6168.

[24]   Bertie, J. E.; Lan, Z. *The Journal of Physical Chemistry B* 101, (**1997)**, 4111-4119.

[25]   Wakisaka, A.; Takahashi, S.; Nishi, N. *Journal of the Chemical Society, Faraday Transactions* 91, (**1995)**, 4063-4069.

[26]   Takamuku, T.; Tabata, M.; Yamaguchi, A.; Nishimoto, J.; Kumamoto, M.; Wakita, H.; Yamaguchi, T. *The Journal of Physical Chemistry B* 102, (**1998)**, 8880-8888.

[27]   O'Toole, T. R.; Younathan, J. N.; Sullivan, B. P.; Meyer, T. J. *Inorganic Chemistry* 28, (**1989)**, 3923-3926.

[28]   Harriman, A.; Pickering, I. J.; Thomas, J. M.; Christensen, P. A. *Journal of the Chemical Society, Faraday Transactions 1: Physical Chemistry in Condensed Phases* 84, (**1988)**, 2795-2806.

[29]   Hoertz, P. G.; Kim, Y.-I.; Youngblood, W. J.; Mallouk, T. E. *The Journal of Physical Chemistry B* 111, (**2007)**, 6845-6856.

[30]   Morris, N. D.; Suzuki, M.; Mallouk, T. E. *The Journal of Physical Chemistry A* 108, (**2004)**, 9115-9119.

[31]   Gambardella, A. A.; Bjorge, N. S.; Alspaugh, V. K.; Murray, R. W. *The Journal of Physical Chemistry C* 115, (**2011)**, 21659-21665.

[32]   Michaux, K. E.; Murray, R. W. *Langmuir* 29, (**2013)**, 12254-12258.

[33]   Nakagawa, T.; Beasley, C. A.; Murray, R. W. *The Journal of Physical Chemistry C* 113, (**2009)**, 12958-12961.

[34]   Ghosh, P. K.; Brunschwig, B. S.; Chou, M.; Creutz, C.; Sutin, N. *Journal of the American Chemical Society* 106, (**1984)**, 4772-4783.

Chapter 5

Enhanced Reactivity of Water in Water/Acetonitrile Mixtures Studied by Cyclic Voltammetry

_____

5.1   Introduction

In the previous chapter we found that the kinetics of the WOR, with $[Ru(bpy)_3]^{3+}$ as the electron acceptor and IrO_x nanoparticles (NPs) as the catalyst, was dependent on the water content when the reaction takes place in water/acetonitrile (water/ACN) mixtures. Those changes in reactivity were attributed to the modification in structure of water, which is dependent on the ratio between the two solvents. The ice-like structure of water is predominant at high water contents. However, as the water content decreases below $X_{H_2O} \leq 0.8$, the hydrogen bond structure degrades and water is present preferentially as clusters. In comparison to pure water, our kinetic measurements indicated that water molecules in these clusters show a markedly enhanced susceptibly to oxidation. The WOR exhibited bimolecular kinetics, first order with respect to the concentration of IrO_x NPs and the concentration of oxidant. Notably, the second order rate constant depended on the water content, showing a

maximum at approximately equimolar proportions ($\approx 25\ \%$ H_2O (v/v)), when both water and ACN clusters co-exist in the mixture. Herein, we rationalize the changes in the reactivity of water molecules in water/ACN mixtures of various compositions by demonstrating that the onset potential for the WOR at an electrode surface modified with IrO_x NP catalyst shifts as X_{H_2O} is varied. To achieve this, we utilized fluorinated tin oxide (FTO) electrodes modified sequentially layer-by-layer with the positively charged polymer poly(diallydimethylammonium chloride) (PDDA) and negatively charged citrate-stabilized IrO_x NPs. In the chapter 2, we showed the electrocatalysis of the WOR in aqueous media using these layer-by-layer modified FTO electrodes that exhibited good operational stability, remaining active over a wide pH-range. Herein, these electrodes are utilized as a platform to study the electrocatalysis of the WOR in water/ACN mixtures. The goal is to provide a clear correlation between the enhanced kinetics of the WOR in water/ACN mixtures and the underlying thermodynamics that facilitates this kinetic enhancement.

5.2   Materials and methods

5.2.1 Chemicals

All chemicals were used as received without further purification. Potassium hexachloroiridate (IV) (K_2IrCl_6, 99.99%), tri-sodium citrate dihydrate ($\geq$ 99.0%), poly(diallydimethylammonium chloride) (PDDA, 20%, Mw 200,000 – 350,000), hexaammineruthenium(III) chloride ($Ru(NH_3)_6Cl_3$, 98%), HPLC grade acetonitrile (ACN, $\geq$ 99.0%) and perchloric acid ($HClO_4$, 70%) were purchased from Aldrich. The water/ACN mixtures were prepared using HPLC grade ACN and ultrapure water (Millipore Milli-Q, specific resistivity 18.2 MΩ·cm). Pure O_2 (medical) cylinders were purchased from Carbagas.

5.2.2 Methods

Electrochemical experiments were carried out under aerobic conditions at an ambient temperature (23 ± 2 °C) using a PGSTAT 30 potentiostat (Metrohm, CH). A typical three-electrode configuration was used for all cyclic voltammetry experiments. The working electrodes were FTO slides modified (15 Ω/sq., 2.2 mm thickness, Solaronix) with 8 bilayers of IrO_x/PDDA. The IrO_x NPs were synthesized and characterized as discussed in the chapter 2. The catalytic electrodes were prepared using a layer-by-layer (LbL) methodology, sequentially depositing negatively charge citrate stabilized IrO_x NPs and the cationic PDDA polymer. This methodology is described in detail in the chapter 2. Briefly, clean FTO slides were immersed in a solution of a positively charged polymer (PDDA), rinsed and immersed in a solution of negatively charged citrate-stabilized IrO_x NPs. By repeating this procedure a multilayer of catalyst was obtained. The counter and reference electrodes in solution were a platinum wire and a Ag/AgCl electrode, respectively.

5.3   Results and discussion

The catalytic oxidation of water in water/ACN mixtures by $[Ru(bpy)_3]^{3+}$ is dependent on the acid-base properties of the media at a fixed water content (10% (v/v)) [1]. The reaction rates using 4.3 mM $NaHCO_3$/Na_2SiF_6 buffer as the acidic regulator exceeded by 2 orders of magnitude those found in 20 mM $HClO_4$. Such slower base rate of catalysis in acidified media permitted a far greater temporal resolution during the kinetic study performed in Chapter 4. In this chapter, the voltammetric study of the reactivity of water in various water/ACN mixtures was performed in $HClO_4$ *(i)* to have a direct comparison with the kinetic experiments previously discussed, *(ii)* as $HClO_4$ allows experiments to be performed without the addition of other supporting electrolytes, and *(iii)* as the IrO_x/PDDA bilayers on the FTO electrode exhibit optimal stability under these acidic conditions[2].
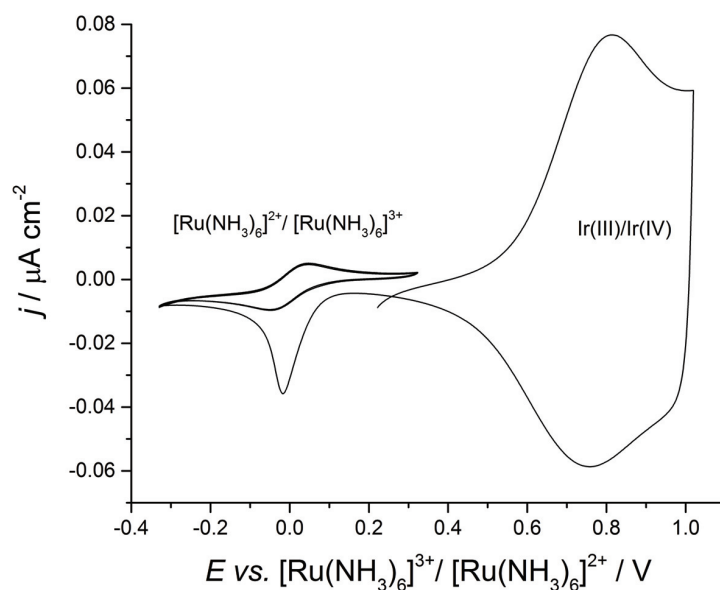
Figure 5.1 Cyclic voltammogram of an FTO electrode modified with 8 IrO_x/PDDA NP bilayers in the presence of $\approx$ 80μM $Ru(NH_3)_6Cl_3$. The supporting electrolyte was 20 mM $HClO_4$ in a water/ACN mixture (35% (v/v) H_2O).

A key consideration in the experimental design was the methodology to calibrate the reference electrode. A detailed study of the effect of varying water content on the WOR onset potential for a water/non-aqueous solvent requires the use of a universal scale to compare potentials between individual experiments. This is easily accomplished in pure aqueous solutions by the use of universally accepted references such as the saturated calomel electrode (SCE) or Ag/AgCl electrode, both of whose potentials *versus* the standard hydrogen electrode (SHE) are well-known and stable over time. Cyclic voltammetry experiments herein, however, were carried out in the presence of significant quantities of organic solvent and the use of the aforementioned references in organic solvents inevitably includes unknown liquid junction potentials. A typical approach to circumvent this difficulty is the use of an internal redox active reference molecule such as ferrocene. However, as the composition of the solvent changes, the hydration properties of both the reduced and oxidized species are also modified [3,4]. Therefore, the potential of the internal reference itself on the universal scale is also expected to change. The calculation of those potentials *via* thermodynamic cycles is also problematic due to the large body of thermodynamic quantities required.

Herein, two independent references, $Ru(NH_3)_6Cl_3$ and the IrO_x NP Ir(III)/Ir(IV) redox transition, were used to have a qualitative idea of the reactivity of water in the water/ACN mixtures. In this regard, after each experiment, the potential window was calibrated by the addition of ≈ 80 μM $Ru(NH_3)_6Cl_3$. This molecule was used as an internal reference due to the suitability of its redox potential, discussed below, and good solubility across the range of X_{H_2O} values studied.

A cyclic voltammogram of the IrO_x/PDDA modified FTO electrode in water/ACN mixtures containing 20 mM $HClO_4$ and 80 μM $Ru(NH_3)_6Cl_3$ is shown in Figure 5.1. Clearly, the redox couple associated with $Ru(NH_3)_6Cl_3$ is well-separated from the redox processes of the IrO_x NPs allowing a precise determination of the potential. CVs of the IrO_x/PDDA modified FTO electrodes as a function of X_{H_2O} in water/ACN mixtures are shown in Figures 5.2 A-B. The 5th CV cycle was chosen for comparison due to the substantial changes in the observed voltammetry, associated with the relaxation processes of the film (*e.g.,* ingress of the water/ACN mixture into the structure of the LbL film) that take place during the first few CV cycles. This is especially the case at low water contents, where the medium is substantially different to that used during layer-by-layer deposition. The CVs were taken at low potentials because the stability of the IrO_x/PDDA modified FTO electrode at higher potentials is substantially reduced in ACN containing solutions. This loss of stability, which is marginal at the working conditions employed (low potentials), most likely takes place due to the swelling of the polymer and the breakdown of the electrostatic interactions binding the layers together on the electrode surface.

Noticeably, all CVs in Figures 5.2 A-B resemble those obtained previously in acidic aqueous media exhibiting Ir(III)-Ir(III)/Ir(IV)-Ir(IV) and Ir(IV)-Ir(IV)/Ir(IV)-Ir(V) redox transitions at 0.78 V and 1.07 V, respectively [2,5,6], and the onset potential for the WOR in the range (1.17-1.32) V. A closer inspection, inset, of the CVs in Figure 5.2 A reveals that at high water contents ($X_{H_2O} \geq 0.6$), the voltammetry remains practically unaffected. However, the onset potential for the WOR is shifted towards more negative potentials (i.e., to lower overpotentials), while the potential of the Ir(III)/Ir(IV) redox transition increases significantly.
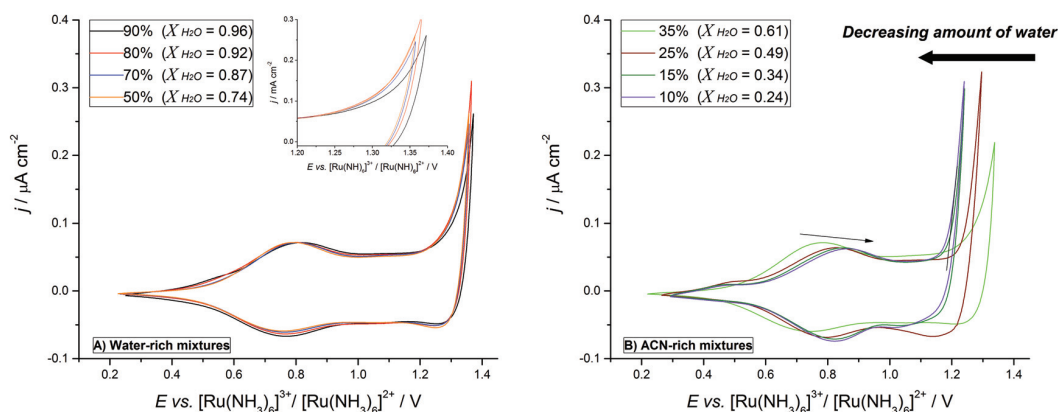
Figure 5.2 (A,B) CVs of the IrO$_x$/PDDA modified FTO electrode in water/ACN mixtures as a function of water mole fraction (X_{H_2O}).
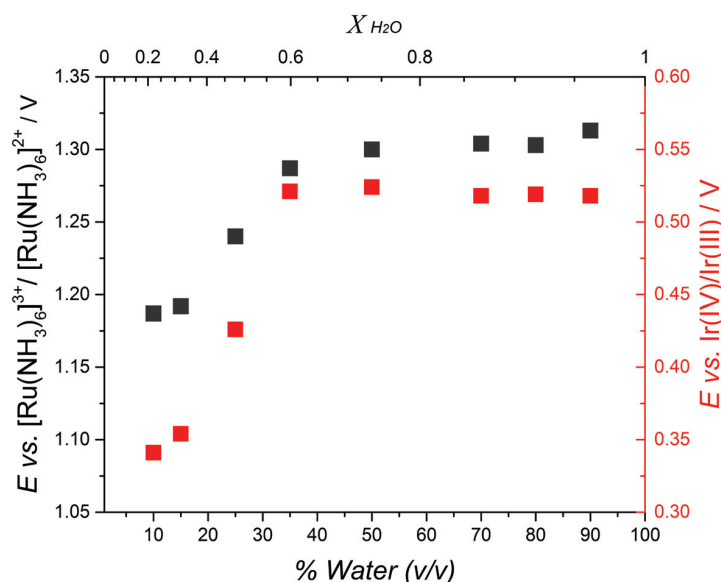
Figure 5.3 Onset potentials for the WOR in water/ACN mixtures represented on two different potential scales: black squares, *versus* [Ru(NH$_3$)$_6$]$^{3+}$/[Ru(NH$_3$)$_6$]$^{2+}$; red squares, *versus* Ir(IV)/Ir(III)

The onset potentials for the WOR as a function of X_{H_2O} or % water (v/v) are summarized in Figure 5.3 and Table 5.1, referenced both against the scale calibrated with the [Ru(NH$_3$)$_6$]$^{2+}$/[Ru(NH$_3$)$_6$]$^{3+}$ redox couple and also *versus* the Ir(III)/Ir(IV) redox transitions of the IrO$_x$ NPs. In both cases, the tendency is almost the same. A relatively constant onset potential for the WOR is observed as the water content decreases from $X_{H_2O} = 0.9$ to $X_{H_2O} = 0.6$. Subsequently, a sharp decrease in the onset potential is observed when $X_{H_2O} \leq 0.6$. Such changes cannot be attributed only to variations of the potential of the internal [Ru(NH$_3$)$_6$]$^{2+}$/ [Ru(NH$_3$)$_6$]$^{3+}$ reference

electrode on the standard hydrogen scale. Indeed, the fact that the onset potential measured with respect to the Ir(III)/Ir(IV) redox transition follows the same trend is a good indication that the changes in the onset potential are mostly related to the change in the thermodynamics or kinetics of the WOR as a function of X_{H_2O}, rather than artifacts due to the potential scale calibration.

Table 5.1 Summary of the onset potentials for WOR in the water/ACN mixtures, using two independent references. For details see main text.

Water mole fraction (X_{H_2O})	E vs. $[Ru(NH_3)_6]^{3+}/[Ru(NH_3)_6]^{2+}$ / V	E vs. Ir(IV)/Ir(III) / V
0.244	1.187	0.341
0.338	1.192	0.354
0.491	1.240	0.426
0.610	1.287	0.521
0.744	1.300	0.524
0.871	1.304	0.518
0.921	1.303	0.519
0.963	1.313	0.518

In order to determine if the changes observed in the Figure 5.3 respond to a kinetic or a thermodynamic effect, the individual contribution of each species (*i.e.,* H_2O, H^+ and O_2) to the overall potential for the WOR was calculated. The thermodynamic potential for the WOR is given by the Nernst equation as follows:

$$E = E^{\ominus}_{O_2/H_2O} + \frac{RT}{4F}\ln\left[\frac{f_{O_2}}{p^{\ominus}}\right] + \frac{RT}{F}\ln\left[a_{H^+}\right] - \frac{RT}{2F}\ln\left[a_{H_2O}\right] \qquad (5.1)$$

where $E^{\ominus}_{O_2/H_2O}$ is the standard potential for the WOR, f_{O_2} is the fugacity of the oxygen, $p^{\ominus}$ is the pressure at standard conditions. The terms a_{H_2O} and a_{H^+} stand for the activity of protons and water, respectively. For simplicity, all the changes in the

thermodynamic potential will be referred to an aqueous system containing 20 mM $HClO_4$ and saturated with O_2. Accordingly, equation (5.1) becomes:

$$\Delta E = E - E_{O_2/H_2O}^{ref} = \frac{RT}{4F} \ln\left[\frac{f_{O_2}}{p^{ref}}\right] + \frac{RT}{F} \ln\left[\frac{a_{H^+}}{a_{H^+}^{ref}}\right] - \frac{RT}{2F} \ln\left[\frac{a_{H_2O}}{a_{H_2O}^{ref}}\right] \tag{5.2}$$

where E_{O_2/H_2O}^{ref} denotes the new reference system, and the three terms on the right side of the equation correspond to the individual contributions to the variation of the potential from each species.

Since all the experiments were performed in air saturated conditions, the first term on the right side of equation (5.2) becomes zero for all mixtures.

The activity of the protons is calculated using the extended Debye-Huckel model:

$$\log \gamma_{H^+} = \frac{z^2 A \sqrt{I}}{1 + a_0 B \sqrt{I}} \tag{5.3}$$

where I is the ionic strength, and the terms A and a_0B are empirical parameters related to the densities and dielectric constants. In all cases $HClO_4$ was assumed to be fully dissociated. The constants utilized in the calculation are those reported by Gagliardi and co-workers.[7] The activity values obtained as well as the contribution of protons (dE_{H^+}) to the change in the overall potential for the WOR are summarized in Table 5.1 and Figure 5.4

Similarly, the activity of water in equation (5.2) can be rewritten as:

$$a_{H_2O} = \gamma_{H_2O} \cdot X_{H_2O} \tag{5.4}$$

where X_{H_2O} is the molar fraction of water in each mixture. Table 5.3 and Figure 5.4 summarize the activity values for water calculated using equation (5.4), and the contribution to the potential for the WOR (dE_{H_2O}) calculated from equation (5.2). The activity data used for the calculation was that reported by Zhang and coworkers[8]

Table 5.2 Summary of the proton activity and its contribution to the potential for WOR in different water/ACN mixtures.

X_{H_2O}	γ_{H^+}	a_{H^+}	$dE_{H^+} = \dfrac{RT}{F} \ln\left[\dfrac{a_{H^+}}{a_{H^+}^{ref}}\right] / mV$
1	0.872	0.0174	0
0.9535	0.865	0.0173	-0.188
0.9012	0.855	0.0171	-0.485
0.842	0.842	0.0168	-0.870
0.774	0.827	0.0165	-1.341
0.695	0.809	0.0162	-1.886
0.603	0.790	0.0158	-2.502
0.494	0.768	0.0154	-3.189
0.363	0.745	0.0149	-3.956
0.202	0.720	0.0144	-4.831
0	0.691	0.0138	-5.869

Table 5.3 Summary of the water activity and its contribution to the potential for WOR in different water/ACN mixtures.

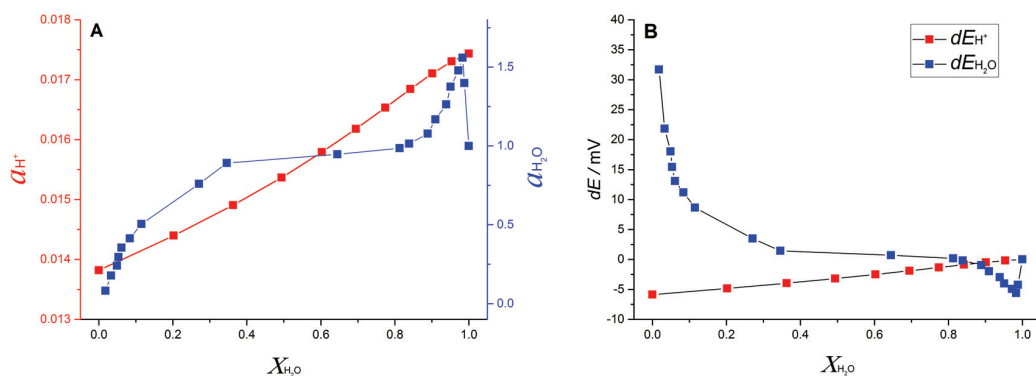| X_{H_2O}	γ_{H_2O}	a_{H_2O}	$dE_{H_2O} = \dfrac{RT}{2F}\ln\left[a_{H_2O}\right]/\mathrm{mV}$
1	0.999	0.999	0.013
0.988	1.416	1.399	-4.241
0.983	1.586	1.559	-5.609
0.972	1.521	1.478	-4.938
0.951	1.446	1.375	-4.023
0.939	1.346	1.264	-2.958
0.91	1.284	1.168	-1.966
0.889	1.212	1.077	-0.942
0.839	1.209	1.014	-0.180
0.813	1.213	0.986	0.176
0.645	1.468	0.947	0.690
0.346	2.575	0.890	1.4584
0.271	2.801	0.759	3.482
0.115	4.390	0.505	8.633
0.084	4.917	0.413	11.168
0.061	5.817	0.355	13.086
0.053	5.56	0.295	15.432
0.049	4.9	0.240	18.0195
0.033	5.383	0.178	21.825
0.018	4.514	0.081	31.704

Figure 5.4 A) Activity of H^+ and H_2O as a function of X_{H_2O} the of the water/ACN mixtures. **B)** Variation of the potential for WOR due to the changes in the activities of H^+ and H_2O.

Figure 5.4 summarizes of the contributions from the activity of protons and water to the overall potential of water oxidation. Interestingly, the decrease in the concentration of water produces a shift of the thermodynamic potential for WOR of about +25 mV. Hence, the changes in the reactivity of water towards oxidation have to be related to a kinetic effect rather than a lowering of the thermodynamic.

X-ray diffraction and infra-red (IR) spectroscopy studies of water/ACN mixtures by Takamuku *et al.* revealed that the strong hydrogen-bond network gradually degrades upon the introduction of ACN[9]. This process leads to the formation of water clusters or micro-heterogeneities at $0.4 \leq X_{H_2O} \leq 0.8$ and, finally, low bonded trimers and tetramers when the amount of water decreases below $X_{H_2O} \approx 0.4$. An increase in the frequency of the O-H vibration with decreasing X_{H_2O} was observed by Takamuku *et al.* and is used as an indication of the strength of the hydrogen bonding. Those changes in the organization of the water molecules directly influence their reactivity, as described previously [1]. For instance, the trend in the variation of the strength of the hydrogen bonding as a function of X_{H_2O} was mirrored the finding reported in the chapter 4, where the second order rate constant for water oxidation using the oxidant $[Ru^{III}(bpy)_3]^{3+}$ and catalyzed by IrO_x NPs, increased progressively with decreasing X_{H_2O} in the region $0.4 \leq X_{H_2O} \leq 0.8$. Indeed, the second order constant in this region exceeded that at high water contents, where the water is present as extended hydrogen bonded structure, by more than a factor of three. Importantly, the changes in the kinetics of the WOR we determined previously correlate well with the reduced kinetic

barriers towards water oxidation observed here below $X_{H_2O} \approx 0.6$ (see Figure 5.3). The later value for mixtures containing $X_{H_2O} \approx 0.24\text{-}0.34$, is about 200 mV lower compared to the value in neat water. This is remarkable if one considers that in order to promote such changes at a constant rate constant, the concentration of a reactant or product has to be modified by more than three orders of magnitude.
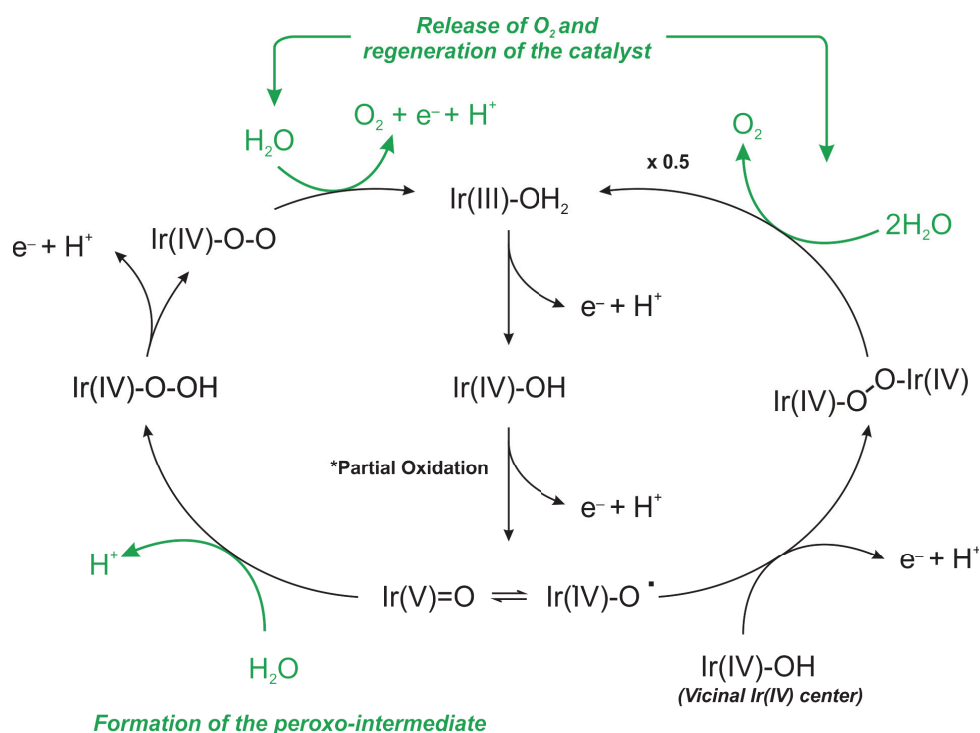
Figure 5.5 Simplified version of the mechanism for the WOR with IrOx. *Only a fraction of the Ir(III) sites undergo oxidation to Ir(IV) species in this step.

Unlike for some molecular catalysts, the mechanistic details about the processes happening at the surface of an oxide are not fully understood. Especially, there is no consensus about whether the water oxidation at the IrO_x proceeds by a monomolecular or bimolecular pathway[6]. Nevertheless, it is universally accepted that Ir(III)-OH$_2$ centers are oxidized to Ir(IV)-OH followed by a partial oxidation to Ir(V)=O (Figure 5.5). The latter species, which possess a radical character (Figure 5.5), can either react with a Ir(IV)-OH center or with a water molecule to produce O$_2$. In both cases, a low-bonded system is beneficial for the overall water oxidation process. In the former case, low-bonded water is expected to regenerate the catalyst more rapidly once the oxygen evolution takes place. On the other hand, if the reaction

takes place by a single-site mechanism, a "less protected water molecule" would lead to higher rates due to both higher rates in the formation of peroxo-intermediates and regeneration of the catalyst during the oxygen evolution step. In both cases a kinetic effect can explain the experimental results. A simplified scheme showing the two possible mechanisms for WOR as well as the steps where the low bonded water plays a fundamental role is shown in Figure 5.5. This scheme is based on the mechanism proposed by Crabtree *et al*[10,11] for the oxidation of water catalyzed by organometallic Iridium complexes and the electrochemistry of highly hydrated iridium oxide films (HIROFs) [5,6,12-14].

5.4   Conclusions

The layer-by-layer methodology introduced in the Chapter 2 and used again in this chapter was demonstrated as a highly flexible platform to investigate the electrocatalytic reactivity of various electrode designs, which can incorporate a particular catalyst for a specific process of interest. Specifically, we show that this methodology represents a convenient strategy to evaluate changes in the reactivity of water upon incorporation of a structure breaker co-solvent. This study highlights that a tipping point exists where the kinetic barriers to water oxidation begin to lower when $X_{H_2O} \leq 0.6$ in water/ACN mixtures. This finding correlates very well with our previous findings that the kinetics of the WOR in water/ACN mixtures are enhanced with decreasing X_{H_2O} in the region $0.4 \leq X_{H_2O} \leq 0.8$. Thus, while the majority of studies in the literature focus on improving the kinetic efficiency of the WOR through advanced water oxidation catalyst design, we highlight that serious improvements may be attained though the incorporation of additives to neat water. In this respect, future work will involve the introduction of molecules capable of modifying the structure of water, such as chaotropic and cosmotropic agents.

5.5 **Bibliography**

[1]   Hidalgo-Acosta, J. C.; Mendez, M. A.; Scanlon, M. D.; Vrubel, H.; Amstutz, V.; Adamiak, W.; Opallo, M.; Girault, H. H. *Chemical Science 6*, (**2015**), 1761-1769.

[2]   Hidalgo-Acosta, J. C.; Scanlon, M. D.; Mendez, M. A.; Amstutz, V.; Vrubel, H.; Opallo, M.; Girault, H. H. *Physical Chemistry Chemical Physics 18*, (**2016**), 9295-9304.

[3]   Su, B.; Hatay, I.; Li, F.; Partovi-Nia, R.; Méndez, M. A.; Samec, Z.; Ersoz, M.; Girault, H. H. *Journal of Electroanalytical Chemistry 639*, (**2010**), 102-108.

[4]   Mendez, M. A.; Partovi-Nia, R.; Hatay, I.; Su, B.; Ge, P.; Olaya, A.; Younan, N.; Hojeij, M.; Girault, H. H. *Physical Chemistry Chemical Physics 12*, (**2010**), 15163-15171.

[5]   Steegstra, P.; Ahlberg, E. *Electrochimica Acta 76*, (**2012**), 26-33.

[6]   Steegstra, P.; Busch, M.; Panas, I.; Ahlberg, E. *The Journal of Physical Chemistry C 117*, (**2013**), 20975-20981.

[7]   Carroll, S.; Baldwin, R. P. *Analytical Chemistry 82*, (**2010**), 878-885.

[8]   Shitashima, K.; Kyo, M.; Koike, Y.; Henmi, H. In *Underwater Technology, 2002. Proceedings of the 2002 International Symposium on* 2002, p 106-108.

[9]   Takamuku, T.; Tabata, M.; Yamaguchi, A.; Nishimoto, J.; Kumamoto, M.; Wakita, H.; Yamaguchi, T. *The Journal of Physical Chemistry B 102*, (**1998**), 8880-8888.

[10]   Blakemore, J. D.; Schley, N. D.; Balcells, D.; Hull, J. F.; Olack, G. W.; Incarvito, C. D.; Eisenstein, O.; Brudvig, G. W.; Crabtree, R. H. *Journal of the American Chemical Society 132*, (**2010**), 16017-16029.

[11]   Thomsen, J. M.; Huang, D. L.; Crabtree, R. H.; Brudvig, G. W. *Dalton Transactions 44*, (**2015**), 12452-12472.

[12]   Buckley, D. N.; Burke, L. D. *Journal of the Chemical Society, Faraday Transactions 1: Physical Chemistry in Condensed Phases 71*, (**1975**), 1447-1459.

[13]   Buckley, D. N.; Burke, L. D. *Journal of the Chemical Society, Faraday Transactions 1: Physical Chemistry in Condensed Phases 72*, (**1976)**, 2431-2440.

[14]   Buckley, D. N.; Burke, L. D.; Mulcahy, J. K. *Journal of the Chemical Society, Faraday Transactions 1: Physical Chemistry in Condensed Phases 72*, (**1976)**, 1896-1902.

Chapter 6

Water Splitting by Tetrathiafulvalene

_____

6.1 Introduction

The photochemical generation of hydrogen (H_2) *via* water splitting is an elegant convenient strategy to store solar energy, while keeping a low environmental impact. H_2 is one of the best energy carriers, displaying the highest energy density and producing only beneath water as combustion product, which is economically and environmentally highly attractive. [1-5]

Photocatalytic systems for water splitting can operate basically under two configurations[6]. The first one comprises a single site excitation site, which is able, through the use of suitable catalysts, to perform WOR and HER. The advantage of this system is its relative simplicity. However, in practice, it is difficult to find materials, with excited-state reduction potential more positive than the water oxidation potential, and the excited-state oxidation potential more negative than the potential for hydrogen evolution. A second alternative is the use of the so-called Z scheme, inspired in artificial photosynthesis. In the Z-scheme, two photocatalytic systems, one for WOR and another for HER, are combined by means of a suitable non-sacrificial electron donor/acceptor. Such scheme, allows for a more efficient

conversion of visible light compared to the conventional one-step water-splitting systems because the energy required to drive each photocatalyst is reduced.

Several systems have been reported promising to operate under Z-scheme, by using non-sacrificial donor/acceptors for HER and/or WOR. Mills and coworkers showed that the solid semiconductor WO_3 can evolve oxygen by using non-sacrificial electron donors such as Fe^{2+} [7]. Mallouk *et al.* reported the visible-light photolysis of HI, storing energy as H_2 and I_3^-, by using Pt intercalated in $H_2K_2NbO_{17}$, and sensitized by a Ru complex [8,9]. Noteworthy, the intercalation of the Pt particles allows HER, while suppressing the reduction of I_3^-. Progressive deactivation was proposed to happen by reduction of accumulated I_3^- by electrons from the surface of $H_2K_2NbO_{17}$. Abe *et al.* reported an optimized system for overall water splitting in a Z scheme using TiO_2. [10-12] In such a system, Pt-anatase is the H_2 evolution composite, TiO_2 acts as the water oxidation catalyst, and the two systems are connected by a I^-/IO_3^- reversible redox shuttle. Another very interesting example was reported by Matsumura *et al.*, who achieved H_2 and O_2 evolution in a two compartment cell [13]. The WOR takes place on rutile TiO_2 suspended in the anode compartment with Fe^{3+} as electron acceptor, while H_2 evolves from Pt/rutile in the cathode using bromide as electron donor. The recycling of the two redox shuttles occurs at Pt coils which is connected to the two compartments, while ionic compensation takes place by the use of a nafion membrane. Recently, in an unpublished work from our laboratory, $Cp_2^*Ru^{(II)}$, was found to act as photosensitizer and electron donor for the photo reduction of protons in acidified solutions. The non-sacrificial character of the system was corroborated by the photocatalytic currents observed during cyclic voltammetry at potentials where the oxidized form of $Cp_2^*Ru^{(II)}$, $Cp_2^*Ru^{(III)}$, is recycled back into $Cp_2^*Ru^{(III)}$.

All those works highlight the importance of catalytic processes coupled to reversible redox shuttles, in order to have a sustainable system for fuel generation. In this chapter, we propose the use of TTF as a non-sacrificial electron donor/acceptor for the HER and WOR under acidic conditions. The excited state of the protonated form of TTF adsorbed on Pt, was found to reduce protons to H_2, while the partially oxidized form of TTF, $TTF^{\bullet+}$, can be utilized as catalyst-free electron acceptor during the phototooxidation of water, yielding TTF and O_2 [14]. The results provides herein can

be applied for the further development of a metals-free systems for overall water splitting.

6.2 Materials and methods

6.2.1 Chemicals

All chemicals were used as received without further purification. Triflic acid (TA, ReagentPlus ≥99%) and Pt powder were purchased from Sigma-Aldrich (Particle size 0.15-0.45 μm). Acetonitrile (ACN, extra dry over molecular sieves, 99.9%), tetrathiafulvalene (TTF, 99+%) were ordered from Acros.

6.2.2 Photocatalytic HER

The experiments were performed in septum-sealed cells containing 3 mL of an acidified TTF solution and Pt powder in dry ACN. The cells were illuminated with either 365 or 455 nm Light Emitting Diodes (LED, purchased from Thorlabs, M365L2 and M455L3) and stirred at 1450 rpm. All measurements were performed using aqueous solutions and dry ACN solvent thoroughly de-gassed with nitrogen, under anaerobic conditions in a glovebox purged with nitrogen (O_2 < 0.1 ppm, H_2O < 0.1 ppm) and at an ambient temperature of 23 ± 2 ºC. The details of the experimental conditions and initial composition of the cells used to characterize the photocatalytic system are summarized in Table 1. Typically, the concentration of triflic acid was 0.1 M, with only one experiment performed with a 1 M concentration to study the effect of the pH.

6.2.3 Photocatalytic WOR

The experimental conditions were similar to those for photocatalytic HER, using a glovebox and degasified solutions. In a typical experiment, 300 μL of water were added to a 3 mL solution containing 3 mM TTF, 0.1 M triflic acid and 1 mg Pt

powder. The suspensions were illuminated with a 455 nm LED and stirred at 1450 rpm during 5 h.

Table 1. List of experiments performed to find the optimal conditions for the photocatalytic evolution of H_2 by TTF and to study the kinetics of the reaction. [TA] = 0.1 M.

Exp.	$[TTF]_0$ /(mM)	Pt/ mg	Led Power /(mW•cm^{-2})	Reaction time/h
Blanks				
1	0	1	90.8	24
2	0	0	90.8	24
Effect of the Catalyst loading				
3	3	0.1	90.8	5
4	3	0.5	90.8	5
5	3	1	90.8	5
6	3	3	90.8	5
Effect of $[TTF]_0$				
7	0.1	1	90.8	5
8	1	1	90.8	5
9	3	1	90.8	5
10	5	1	90.8	5
Effect of LED power				
11	3	1	2.6	5
12	3	1	7.3	5
13	3	1	11.7	5
14	3	1	32.8	5
15	3	1	90.8	5
Long-term reaction				
16	3	0	7.3	168
17	3	1	0	168
18	3	1	7.3	168

6.2.4 UV/vis spectroscopy

The progress of the reaction was followed by UV/vis absorption spectroscopy, using a 10 mm optical path length quartz cell and a UV/vis Spectrometer (Agilent Technologies). The solutions were diluted 30 or 60 times prior analysis.

6.2.5 Gas chromatography

After reaction, the headspace of the septum-sealed glass vials (2 mL) was sampled by using a lock-in syringe with a push−pull valve (SGE Analytical Sciences) and subsequently analyzed by injecting into a PerkinElmer gas chromatograph (Thermo Scientific Trace 1300, equipped with a 20 mL loop, HAYESEP DB and an 100/120 mesh) with a thermal conductivity detector (TCD) and argon as carrier gas.

6.2.6 Mass spectrometry

The stability of TTFH$^+$ species during the reaction was evaluated by electrospray ionization mass spectrometry (ESI-MS) using LTQ Velos instrument (Thermo Scientific) equipped with conventional heated ESI source at 2.7 kV potential. The reaction mixture was diluted 10 times with ACN prior to analysis and delivered to the ESI source with flow rate of 5 µL/min. MS analysis was performed in positive polarity with automatic gain control set up to 3e4, enhanced scanning mode activated and in *m/z* range of 150 − 1500.

6.3   Results and discussion

6.3.1 Effect of the catalyst load on HER

Figure 6.1 shows the analysis of the photoreduction of protons by TTFH$^+$ (3 mM TTF and 0.1 M triflic acid) as a function of catalyst load. In order to use the method of initial rates to analyze the kinetic data, the reaction was stopped after 5h, when no significant changes in concentration had occurred in comparison with the global rate

of reaction. The signals centered at 248 and 460 nm (Figure 6.1a) correspond to the UV/vis absorption of TTFH$^+$. Noteworthy, the evolution of H$_2$ was much more efficient when illuminating in the visible (455 nm) than in the ultraviolet (265 nm).

The signals centered at 335, 436 and 578 nm (Figure 6.1) correspond to the formation of TTF$^{•+}$. Interestingly, illumination of TTFH$^+$ in absence of catalyst leads to a 36 % diminution of the absorption of TTFH$^+$, but no evident formation of TTF$^{•+}$ or evolution of H$_2$ (6. 1b) was observed. Such behavior will be explained further on in the text.

Unexpectedly, the addition of 0.1 mg of Pt powder to the photosystem leads to 41% increase of the absorption of TTFH$^+$ (248 nm), which may be linked to light backscattering by small Pt particles left in the solution. Further additions of catalyst lead to decrease of the absorption of TTFH$^+$ but never to a value as low as that exhibited by the system without Pt (Figure 6.1b). Further additions of Pt (beyond 1 mg) have no effect on the concentration of TTFH$^+$ (Figure 6.1b). It must be pointed out that as the reaction progresses, a band at 230 nm develops, most likely due to the presence TTF-oligomer species. Hence, any analysis based on the disappearance of TTFH$^+$ might be misleading and therefore will be omitted.

The evolution of TTF$^{•+}$ increases with the load of catalyst. The largest change in TTF$^{•+}$ concentration occurs upon first addition of Pt (0.1 mg), which corresponds to the peak of formation of the intermediate, subsequent additions account for an increase of only 14% of the maximum TTF$^{•+}$ concentration observed. The amount of added catalyst also has an effect in the rate of H$_2$ evolution, which initially increases to finally reach a plateau at Pt amounts higher than 1mg. Based in the higher rates of production of TTF compared to H$_2$ (Figure 6.1 b), it is possible to conclude that the evolution of H$_2$ is the limiting step in the overall process. On the other hand, the fact that in the three kinetic plots, there is a catalyst concentration optimal beyond which the rate of reaction remains unchanged, can be attributed to: *(i)* passivation of the surface of the catalyst by adsorption of decomposition products, or *(ii)* shielding effect due to backscattering of light by the catalyst particles. In our case passivation is unlikely since MS experiments yielded no evidence of decomposition products.

From 6.1b is clear that the optimal load of Pt powder for the evolution of H_2 is 1 mg, quantity used in all subsequent experiments.
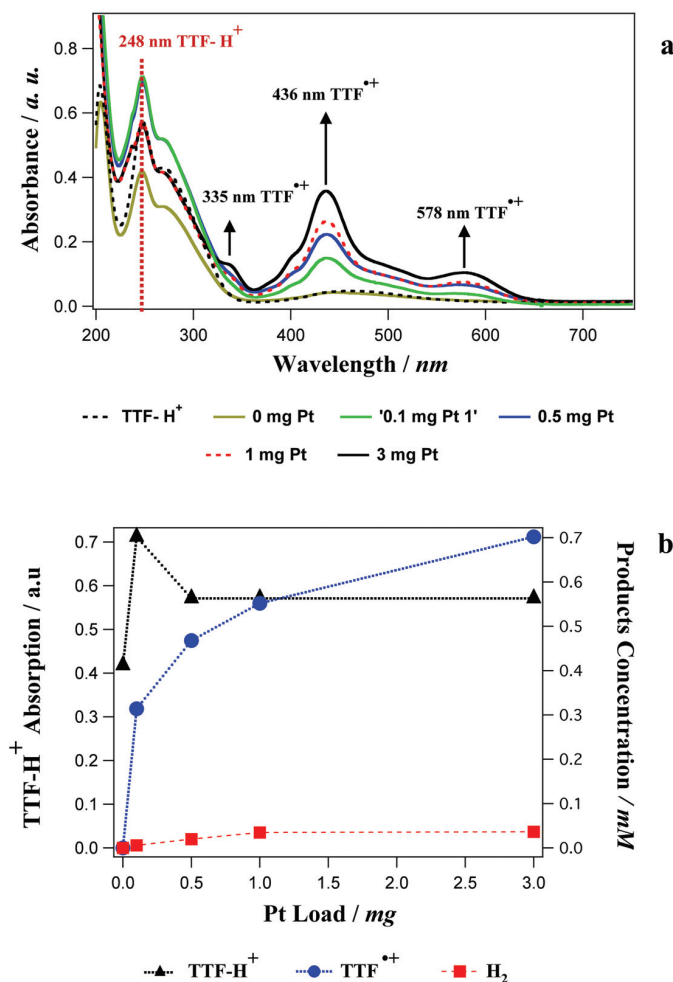

Figure 6.1 (a) UV/vis absorption spectra of mixtures of reaction in presence of different loads of Pt powder, experiments 3 to 6 in Table 1 (diluted 30 times). (b) Kinetic analysis of the depletion of $TTFH^+$ (248 nm) and formation of $TTF^{\bullet+}$ and H_2 as a function of Pt load.

6.3.2 Effect of the initial concentration of TTF

In order to estimate the optimal concentration of TTF for the photocatalytic reaction, the evolution of H_2 and $TTF^{\bullet+}$ was studied as a function of the initial concentration of TTF (Figure 6.2). The results show that both, the amount of H_2 and $TTF^{\bullet+}$, increase with the initial concentration of TTF, reaching an optimal concentration at 3mM $[TTF]_0$, from where no significant changes in the concentration

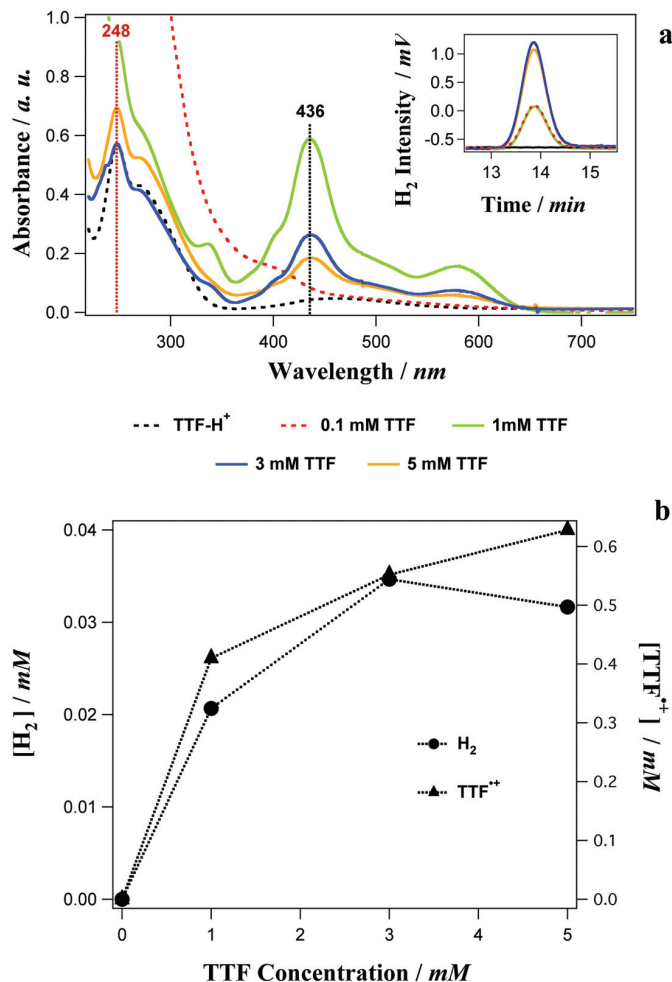of products are observed. This behavior might due to saturation of the surface of the catalyst by adsorbed substrate.

Figure 6.2 (a) Effect of TTF initial concentration, experiments 7 to 10 in Table 1 (diluted down to 100 μM), UV/vis absorption spectra. The inset shows the H_2 peak for those samples in gas chromatography (b) Kinetic analysis of formation of $TTF^{\bullet+}$ and H_2 as a function of the initial concentration of TTF.

The only exception was 0.1 mM TTF, whose spectrum shows total decomposition of TTF (Figure 6.2 a). This cou\\ld be due to the ratio between the concentration of TTF and protons ($[TTF]_0/[H^+]_0$), which in this case is $1\bullet10^{-3}$, one order of magnitude larger than for the other concentrations of TTF ($1\bullet10^{-2}$), where no decomposition was observed. The same kind of decomposition was observed when performing the photocatalytic reaction with a 3 mM solution of TTF and a concentration of protons equal to 1 M (Figure 6.3), in whose case $[TTF]_0/[H^+] = 3x10^{-3}$. Considering that

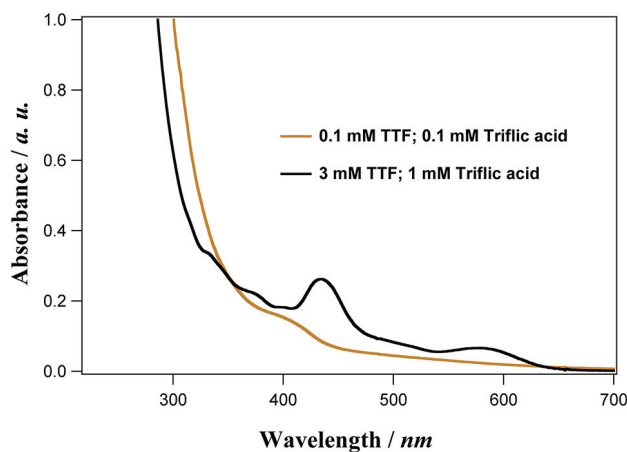decomposition of TTF could account for part of the H_2 obtained, this value was not considered in the analysis.

Figure 6.3 UV/vis absorption spectra of 0.1 mM TTF, 0.1 M TA and 3 mM TTF, 1 M TA mixtures of reaction after 5 h of illumination (445 nm, 90.8 mW•cm^{-2}) and dilution to 100 μM.

6.3.3 Effect of LED power

The effect of the LED Power on the evolution of H_2 and TTF$^{•+}$ is depicted in Figure 6.4. The optimal power of light was found to be 7.3 mW•cm^{-2}, after which the production of TTF$^{•+}$ reaches a plateau, and H_2 evolution decreases. This behavior indicates tht high intensities of light accelerate recombination events.
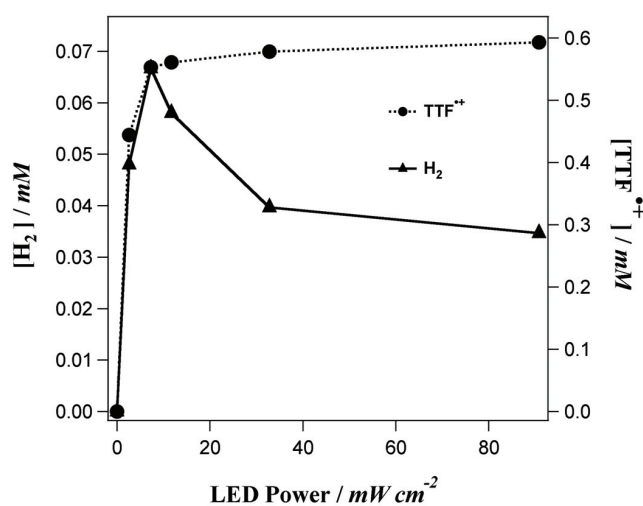

Figure 6.4 Evolution of H_2 and TTF$^{•+}$ as a function of LED power, experiments 11 to 15 in Table 6.1.

6.3.4 Study of the photoreaction as a function of time

Figure 6.5 a, b and c show the evolution of the UV/vis absorption spectra of a 3 mM solution of TTF and 0.1 M triflic acid in: *(a)* absence of catalyst and upon illumination (455 nm; 7.3 mW•cm^{-2}), *(b)* presence of catalyst in the dark and *(c)* presence of catalyst upon illumination.

The illumination of the TTFH$^+$ solution in absence of catalyst (Figure 5a) leads to the formation of TTF$^{•+}$ but no evolution of H$_2$ was observed. In whose case, the formation of the radical cation is due to the reaction between TTFH$^+$ and neutral TTF (Eq. 1), as suggested by Giffard *et al.* [15,16] The rate of reaction was estimated to be 6.9•10^{-4} mM^{-4}•h^{-1}.

$$TTFH^+ + TTF \rightleftharpoons TTFH^• + TTF^{•+} \qquad\qquad (6.1)$$

The dark reaction in presence of Pt also leads to the formation of TTF$^{•+}$ without evolution of H$_2$. The rate of reaction was found to be two orders of magnitude higher (0.038 h^{-1}) than the reaction in absence of catalyst and with and order of reaction equal to 1, which correlates very well with the kinetic analysis made for the reaction as a function of Pt load, and indicates that Pt catalyzes the reaction between TTFH$^+$ and neutral TTF (Equation 6.1).

As previously discussed, the catalyzed photoreaction (Figures 6.5c and 6.6) leads to the formation of TTF$^{•+}$ and H$_2$, with an efficiency (after 160 h) of 83 and 70 %, respectively, with respect to [TTF]$_0$.

Figure 6.6 shows that TTF$^{•+}$ concentration increases with time until reaching a plateau when 83 % of the expected concentration of TTF$^{•+}$ has been formed. On the other hand, the evolution of H$_2$ follows a sigmoid kinetics. Thus, there is an initiation period that comprises the adsorption of TTFH$^+$ on the surface of the catalyst (see also Figure 6.1), forming the intermediate that ultimately absorbs light to perform the reduction of protons.
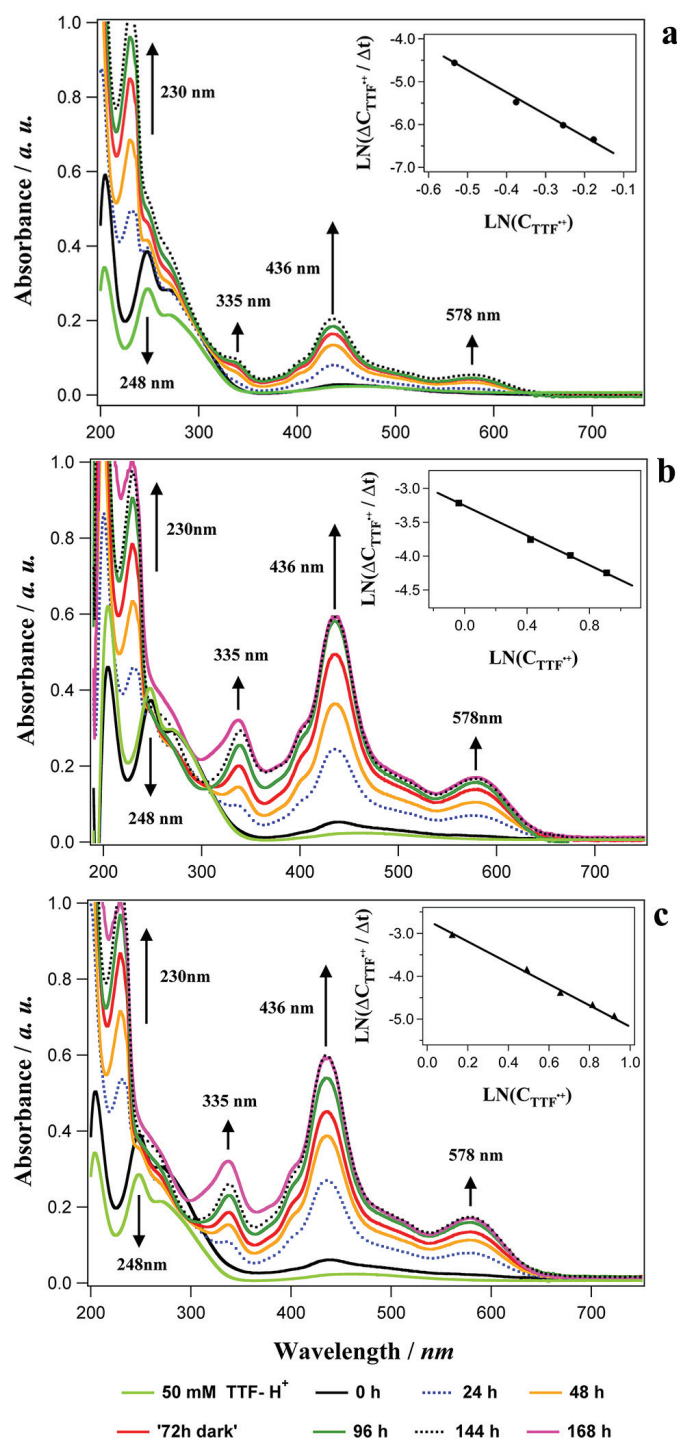
Figure 6.5 Evolution of UV/vis absorption spectra of a 3 mM solution of TTF and 0.1 M triflic acid over 168 h. (a) under illumination (455 nm; 7.3 mW•cm⁻²) and in absence of catalyst, (b) in the dark and in presence of catalyst and (c) under illumination and in presence of catalyst. The inserted figures are the kinetic analysis of the formation of TTF•⁺.
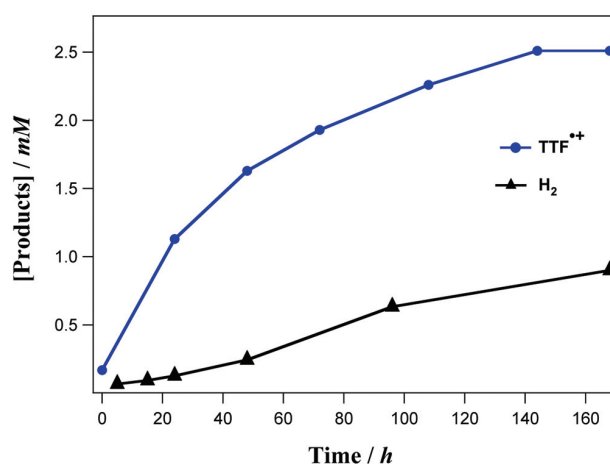
Figure 6.6 Evolution of H_2 and $TTF^{\bullet+}$ under illumination (455 nm; 7.3 mW•cm^{-2}) of TTFH$^+$ over 168 h. [TTF$_0$] = 3mM, [triflic acid] = 0.1 M, Pt powder load = 1 mg.

The order and the rate of reaction of the photo oxidation of TTFH$^+$ to TTF$^{\bullet+}$ were estimated to be 2 and 0.055 mM^{-1}•h^{-1}, respectively, which is slightly slower than the oxidation in the dark. Assuming that due to light backscattering and/or mass-transport limitations, not all the intermediate was efficiently excited, formation of TTF$^{\bullet+}$ in the dark (Equation 1) could be the competitive reaction accounting for the higher production of TTF$^{\bullet+}$ (83 %) in comparison with the evolution of H_2 (70 %).

Unfortunately, the kinetics of disappearance of the intermediate at 248 nm, cannot be followed for longer than 5 h because it is overlapped by the rising of an absorption signal centered at 230 nm (Figure 6.5). The rate of appearance of such signal is the same for the three sets of reaction illustrated in Figure 6.5 regardless the absence of Pt or light, which means that it is neither related to the absorption of TTFH$^+$ on the surface of the catalyst nor to the excitation of TTFH$^+$. This signal could be related to the additional products formed in the reaction in Equation 1.

Some possible chemical reactions leading to H_2 evolution by TTFH$^+$ are shown in Equations 6.2 to 6.9. A first and common step is the formation of the adsorbed intermediate, Pt-[TTFH]$^+$, as shown in Equation 6.2. Then, in light-activated steps, these species can produce H_2, either directly (Equation 6.3), or through the formation of hydrogen radical species (Equations 6.4 and 6.5). Alternatively, the as-formed hydrogen radical (Equation 6.6) can be attacked by [TTFH]$^+$ from solution in a light-activated step (Equation 6.7). A third possibility involves the formation of the TTF$^{\bullet}$

species as shown in Equation 6.8, which can evolve H_2 in the presence of light. The latter mechanism would account for the light independent formation of $TTF^{•+}$.

Protonation:

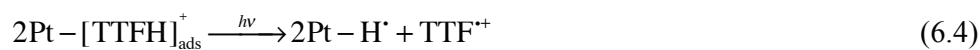$$Pt + TTFH^+ \longrightarrow Pt - [TTFH]_{ads}^+ \tag{6.2}$$

Bimolecular pathways

$$2Pt - [TTFH]_{ads}^+ \xrightarrow{h\nu} 2Pt + 2TTF^{•+} + H_2 \tag{6.3}$$

alternatively,

$$2Pt - [TTFH]_{ads}^+ \xrightarrow{h\nu} 2Pt - H^• + TTF^{•+} \tag{6.4}$$

$$2Pt - H^• \xrightarrow{h\nu} 2Pt + H_2 \tag{6.5}$$

$TTFH^+$ attack:

$$Pt - [TTFH]_{ads}^+ \xrightarrow{h\nu} Pt - H^• + TTF^{•+} \tag{6.6}$$

$$Pt - H^• + TTFH^+ \xrightarrow{h\nu} Pt + TTF^{•+} + H_2 \tag{6.7}$$

Radical pathway

$$Pt - TTF \longrightarrow Pt - TTF^• + TTF^{•+} \tag{6.8}$$

$$2Pt - TTF^• \xrightarrow{h\nu} 2Pt + TTF^{•+} + H_2 \tag{6.9}$$
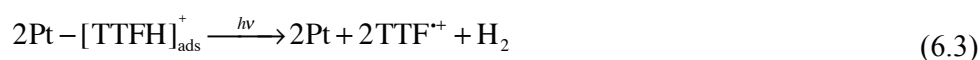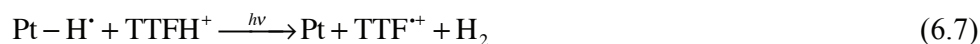
Further experiments on transient adsorption will allow us to determine the redox potential of the excited state of the intermediate.

6.3.5 Effect of the addition of water

Addition of 10 % water into the mixture of reaction (3 mL; 3 mM TTF, 0.1 M TA, 1 mg Pt) leads to evolution of O_2 and total inhibition of the HER. After 5 h of illumination (455 nm; 7.3 mW•cm^{-2}), the OER was performed with an efficiency of

12 % with respect to $[TTF]_0$. In this case the molecule that performs the water oxidation reaction is $TTF^{\bullet+}$, which is formed upon illumination.

The catalytic oxidation of water on the Pt surface under acidic conditions has been widely studied. The first step of the reaction is the adsorption of water on the surface of the catalyst, followed by the irreversible removal of one electron and one proton to form a platinum hydroxide. This accounts for the inhibition of the HER when adding water to the mixture of reaction, since it seems that water (or $TTF^{\bullet+}$-H_2O, yet to be elucidated with further experiments) adsorbs on the surface of Pt faster than $TTFH^+$.

Additionally, the increase in the concentration of water might cause significant changes in the thermodynamic potentials of HER as discussed in Chapter 1. Such increase may also account for the inhibition of the reaction upon addition of water.

Experiments are to be done in order to determine the global efficiency of the WOR and the optimal conditions. MS analysis and studies on the excitation of $TTF^{\bullet+}$ are being performed in order to determine the role of light-driven intermediates in the WOR and to determine the redox potential of such intermediates under acidic conditions.

6.3.6 Mass spectrometry analysis

Performed ESI-MS analysis confirmed the stability of $TTFH^+$ species over time. As demonstrated in Figure 6.7, the MS spectra of reaction solution did not display any significant changes between 0 h, 24 h and 96 h of reaction. It is worth mentioning that that during ESI, $TTFH^+$ species were subjected to in-source oxidation and therefore, were observed in the MS spectra as TTF^+ species with *m/z* 204.
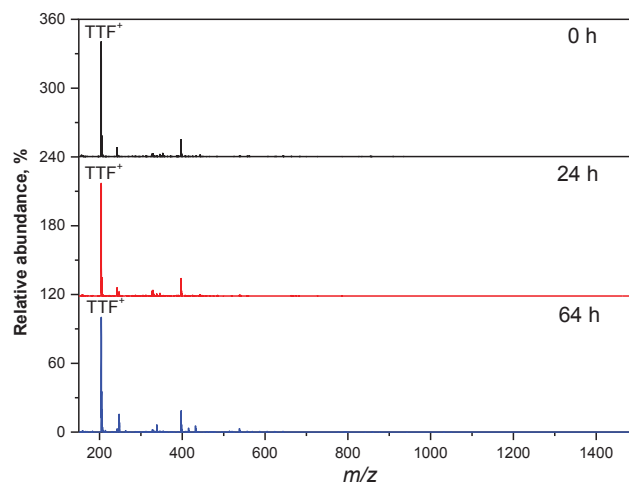
Figure 6.7 Reaction mixture stability test by ESI-MS. MS spectra were collected at 0 (black line), 24 (red line) and 64 h (blue line) of reaction. Peaks of TTF$^+$ were observed at m/z 204. Reaction mixture was diluted 10 times with ACN prior to the analysis.

6.4   Conclusions

The results presented herein clearly show that TTF can   acts a metal-free reversible donor for ligh-driven HER. The efficiency for H$_2$ evolution calculated with respect to the initial concentration of TTF is about 70 %. Based on the kinetics measurements, the reaction seems to proceed *via* adsorption of TTFH$^+$ on the Pt surface, followed by a slow photochemical evolution H$_2$. Also, the addition of water supress the HER and promotes WOR, in apparently unsuitable conditions. Those findings can be used as the starting point for the development of systems for water splitting based in metal-free molecules. Importantly, the flexibility of TTF molecules, in term of ease modification of the redox potentials by incorporation of substituents, might be crucial in avoiding the suppression of HER in water/acetonitrile mixtures. Thus, making possible the use of a unique media for performing both WOR and HER.

6.5   Bibliography

[1]   Barber, J. *Chemical Society Reviews* 38, (**2009**), 185-196.

[2]   Andreiadis, E. S.; Chavarot-Kerlidou, M.; Fontecave, M.; Artero, V. *Photochemistry and Photobiology* 87, (**2011**), 946-964.

[3]   Kärkäs, M. D.; Verho, O.; Johnston, E. V.; Åkermark, B. *Chemical Reviews* 114, (**2014**), 11863-12001.

[4]   Rüttinger, W.; Dismukes, G. C. *Chemical Reviews* 97, (**1997**), 1-24.

[5]   Sartorel, A.; Carraro, M.; Toma, F. M.; Prato, M.; Bonchio, M. *Energy & Environmental Science* 5, (**2012**), 5592-5603.

[6]   Maeda, K. *ACS Catalysis* 3, (**2013**), 1486-1503.

[7]   Darwent, J. R.; Mills, A. *Journal of the Chemical Society, Faraday Transactions 2: Molecular and Chemical Physics* 78, (**1982**), 359-367.

[8]   Kim, Y. I.; Salim, S.; Huq, M. J.; Mallouk, T. E. *Journal of the American Chemical Society* 113, (**1991**), 9561-9563.

[9]   Kim, Y. I.; Atherton, S. J.; Brigham, E. S.; Mallouk, T. E. *The Journal of Physical Chemistry* 97, (**1993**), 11802-11810.

[10]   Abe, R.; Sayama, K.; Domen, K.; Arakawa, H. *Chemical Physics Letters* 344, (**2001**), 339-344.

[11]   Abe, R.; Sayama, K.; Arakawa, H. *Chemical Physics Letters* 371, (**2003**), 360-364.

[12]   Abe, R.; Sayama, K.; Sugihara, H. *The Journal of Physical Chemistry B* 109, (**2005**), 16052-16061.

[13]   Fujihara, K.; Ohno, T.; Matsumura, M. *Journal of the Chemical Society, Faraday Transactions* 94, (**1998**), 3705-3709.

[14]   Adeel, S. M.; Li, Q.; Nafady, A.; Zhao, C.; Siriwardana, A. I.; Bond, A. M.; Martin, L. L. *RSC Advances* 4, (**2014**), 49789-49795.

[15]   Giffard, M.; Alonso, P.; Garín, J.; Gorgues, A.; Nguyen, T. P.; Richomme, P.; Robert, A.; Roncali, J.; Uriel, S. *Advanced Materials* 6, (**1994**), 298-300.

[16]   Giffard, M.; Gorgues, A.; Riou, A.; Roncali, J.; Alonso, P.; Uriel, S.; Garín, J.; Nguyen, T. P. *Synthetic Metals* 70, (**1995**), 1133-1134.

Chapter 7

Concluding Remarks

_____

The results of this work are separated in two main sections. In the first part, Chapter 2-3, two different strategies for immobilization of IrO_x NPs are presented. Both strategies based on the concept of layer-by-layer deposition (LbL). The second part, Chapters 3-5, is devoted to the study of the water oxidation (WOR) and hydrogen evolution (HER), occurring in an unusual liquid-liquid system, water/acetonitrile (water/CAN) mixtures.

Chapter 2-3: Immobilization of IrO_x NPs

Chapter 2 describes a methodology for preparing IrO_x NP films on fluorinated tin oxide (FTO), by deposition of alternate layers of oppositely charged poly(diallyldimethylammonium chloride) (PDDA) polymer and citrate stabilized IrO_x NPs.

Based on the high-resolution scanning electron microscopy (HR-SEM) images, the films consisted of non-aggregated particles embedded in a tissue-like polymeric matrix. Importantly, the use of stabilized particles seems to be crucial in obtaining good electrochemical response, which resembles the highly reversible waves observed in hydrous iridium oxide films (HIROFs), and remains across the whole pH scale.

In accordance with the bulk electrolysis experiments, the catalyst exhibits a good stability in acidic and neutral pH with faradic efficiencies approaching 100%. However, in alkaline media the electrode progressively degrades. This loss of stability is seemingly due to leaching of the PDDA polymer, which under alkaline conditions reacts forming neutral species, thus causing a progressive breakdown of the assembly. Accordingly, in order to improve the stability of the films, future work will involve replacing PDDA with other cationic polymer candidates typically used in LbL methodologies, such as poly(aniline) (PANI), poly(ethylene imine) (PEI), poly-L-lysine, *etc*.

One important drawback of the electrodes obtained in the present work was the low coverage and the consequently low currents under bulk electrolysis. The maximum current density obtained by the FTO electrode modified with 14 IrO_x/PDDA bilayers at η = +400 mV under acidic conditions was 1.5 mA cm^{-2}. However, much higher current densities (*i.e.,* 20-70 times) at similar potentials are required in order to implement our LbL modifed FTO electrodes in solar or electrolyzer technology.

In this regard, two perspectives are considered:

(i) Increase coverage by changing parameters during the synthesis (*e.g.,* concentration of the dipping solution, type of polymer, *etc.*)

(ii) Use of high surface electrodes: High surface area electrodes consisting of thin layers of nanostructured ITO (Sn(IV)-doped indium tin oxide, nanoITO) on reticulated vitreous carbon (RVC) have been reported to be useful in the immobilization of molecular catalyst with anchoring groups. Using this approach the number of active sites can be largely increased without compromising the electrochemical properties of the catalyst. In our case, the extrapolation would be direct, given the similar properties of the ITO and FTO.

In Chapter 3, the layer-by-layer inkjet printing methodology was introduced. This technology drastically reduces the production time and costs thanks to its easy automatization and the low material waste (droplets are only printed on demand) and the possibility to scale up the process from the prototype to the industrial level. Also, through the well-controlled amount of deposited material by inkjet printing, rinsing steps in-between deposited layers can be avoided. With this methodology, pH-sensing electrodes exhibiting fast response time, excellent reproducibility and near-Nernstian sensitivity (58 mV/pH) were obtained. However, the implementation of these electrodes as catalysts for WOR is not possible yet, due to their low stability under sustained bulk electrolysis. The optimization of the conditions (*e.g.,* the amount of the deposited material) in order to obtained films with similar characteristics to those in Chapter 2 is still ongoing work.

Chapter 4-6: WOR and HER in Organic Media

The results shown in Chapter 4 demonstrated that the kinetics of water oxidation is dependent on the water content for water/acetonitrile mixtures. The low-bonded water clusters at intermediate acetonitrile contents ($X_{H_2O} \approx 0.5$) were found to be more reactive, with second order rate constants exceeding about 4 times those at high water contents ($X_{H_2O} \geq 0.95$). This result is of profound importance because shows for the first time a clear correlation between the structure and reactivity of water in water/acetonitrile mixtures.

Overall, the use of water/ACN mixtures appeared to be a better approach to characterize the catalytic activity of water oxidation catalysts enhancing the stability of redox shuttles. This was evident by the complete absence of degradation products after reaction, as studied by NMR spectroscopy.

The enhanced reactivity of water in water/ACN mixtures was further studied in Chapter 5 by cyclic voltammetry at the PDDA-IrO$_x$ electrodes described in Chapter 2. The voltammetric profiles obtained using those electrodes resemble those in aqueous media and remain approximately unchanged at high water contents. However, as the

water content decreases below a water mole fraction (X_{H_2O}) of 0.6, a tipping-point is reached and the onset potential for water oxidation gradually decreases. This finding correlates very well with the kinetic analysis that showed that the WOR in water/ACN mixtures is enhanced when X_{H_2O} is $0.4 \leq X_{H_2O} \leq 0.8$.

In order to determine whether the enhancement in the kinetics of WOR is due to a thermodynamic or purely kinetic effect, the thermodynamic potentials for WOR in the different mixtures were determined. Overall, upon increasing the mole fraction of ACN the Nernst equation predicts an increase in the thermodynamic potential of about +25 mV. Hence, the decreasing in the onset potential for ACN-rich solutions must respond to a favorable kinetic effect in WOR, rather than a lowering in the thermodynamic barriers.

As a general conclusion of Chapters 4 and 5, we highlighted that significant improvements may be attained by the modification of the environment where WOR takes place. An interesting perspective is then the use of agents capable of modifying the structure of water, such as chaotropic and cosmotropic agents, and to study their influence in the kinetics of WOR. Furthermore, the evaluation *via* electrochemistry on IrO$_x$/FTO surfaces could be a valuable tool to study the Hofmeister series from the point-of-view of reactivity.

Additionally, in Chapter 4 the biphasic nature of the water oxidation process in water/ACN mixtures was inferred. It was proposed that water interacts preferentially with the IrO$_x$ NPs. Then, upon incorporation of the oxidant, it partitions across the interface formed between the water-rich domain at the NP surface and the ACN-rich bulk phase, to finally react at the surface of the catalyst. Thus, a good perspective would be to study the effect of interface-polarizing agents, on the kinetics of WOR.

As discussed at the beginning of this thesis, one of the main problems associated to the study of WOR in liquid-liquid system is the poor stability of most the organic solvents under the aggressive conditions imposed by the oxidant. Consequently, the next logical step is the use of ionic liquids. In particular, the use of the liquid-liquid systems, comprising a LbL assembly as aqueous phase could be a good starting point.

Drawing conlusion from Chapter 6, we found that protonated form of tetrathiafulvalene (TTF), [TTF-H]+, is able to perform WOR and HER, acting as both, sensitizer and electron donor/acceptor. Based on the kinetics measurements, the

reaction seems to proceed *via* adsorption of [TTF-H]$^+$ on the Pt surface, followed by a slow photochemical evolution of H$_2$. Further exploration of the system may encompass the use of different catalysts, which can provide a more favourable energetic panorama for H$_2$ evolution. Another important aspect of the system in Chapter 6, is that the addition of water supresses HER, while promoting WOR. The suppression has been rationalized by an increase in the thermodynamic barriers. Indeed, the potential of WOR is expected to increase with the water content. Thus, a good alternative is the use of TTF derivatives with suitable potentials for HER in water/ACN mixtures. Under those conditions a suitable system for overall water splitting mediated by a metal-free molecule can be envisioned.

JONNATHAN C. HIDALGO-ACOSTA

CAMPUS ADDRESS
EPFL Valais Wallis
Rue de l'Industrie 17
CH-1951 Sion
+41 21 69 58249
jonnathan.hidalgo@epfl.ch

Date of Birth: May 4th 1985
Citizenship: Colombian

EDUCATION

2012-2016   **École Polytechnique Fédérale de Lausanne (EPFL).**
Lausanne, Switzerland.
Ph. D in Chemistry and Chemical Engineering
Thesis: Electrochemical Studies of Water Splitting in Organic Media
Thesis Advisor: Prof. Hubert Girault

2010-2011   **University of Alicante**
Alicante, Spain.
Master in Materials Science
Thesis: Adsorption and First Stages of Polymerization of Aniline on Platinum Single Crystals Electrodes
Thesis Advisor: Prof. Juan M. Feliu

2003-2008   **Universidad Nacional de Colombia**
Bogotá, Colombia.
Bachelor degree in Chemistry
Thesis: Current Oscillations During Chromium Electrodissolution
Thesis Advisor: Prof. Marco F. Suárez

RESEARCH EXPERIENCE

2012- Present   **Doctoral Assistant**, Swiss Federal Institute of Technology Lausanne
Lausanne, Switzerland.

2010- 2011   **Researcher in Training**. Institute of Electrochemistry, University of Alicante.
Alicante, Spain.

HONORS AND AWARDS

- Santiago Grisolia Scholarship, Generalitat Valenciana. Alicante, Spain, 2010.

- Second place in the national exam for graduates in Chemistry, (ECAES). Bogotá, Colombia, 2010.

- Five times best GPA in the bachelor program of Chemistry, Universidad Nacional de Colombia. Bogotá, Colombia, (2003-2008).

PUBLICATIONS

[1]   A.J. Olaya, J.C. Hidalgo-Acosta, N. Gasilova, H.H. Girault,*"Water Splitting by Tetrathiafulvalene"* (2016) In preparation.

[2]   M. Jović, J.C. Hidalgo-Acosta, A. Lesch, V. Costa-Basetto, E. Smirnov, F. Cortés-Salazar, H.H. Girault,*" Large-scale Layer-by-Layer Inkjet Printing of Flexible Iridium-Oxide based pH Sensors"* (2016) In preparation.

[3]   J.C. Hidalgo-Acosta, M.D. Scanlon, M.A. Méndez, P. Peljo, M. Opallo, H.H. Girault,*"Enhanced Reactivity of Water Clusters towards Oxidation in Water/Acetonitrile Mixtures"* ChemElectroChem (2016) In Press.

[4]   J.C. Hidalgo-Acosta, M.D. Scanlon, M.A. Mendez, V. Amstutz, H. Vrubel, M. Opallo, H.H. Girault,*"Boosting Water Oxidation Layer-by-Layer"* PCCP 18 (2016) 9295-9304.

[5]   W. Adamiak, J. Jedraszko, O. Krysiak, W. Nogala, J.C. Hidalgo-Acosta, H.H. Girault, M. Opallo,*"Hydrogen and Hydrogen Peroxide Formation in Trifluorotoluene–Water Biphasic Systems"* J. Phys. Chem. C 118 (2014) 23154-23161.

[6]   J.C. Hidalgo-Acosta, M.A. Mendez, M.D. Scanlon, H. Vrubel, V. Amstutz, W. Adamiak, M. Opallo, H.H. Girault,*"Catalysis of water oxidation in acetonitrile by iridium oxide nanoparticles"* Chem. Sci. 6 (2015) 1761-1769.

[7]   J. C. Hidalgo-Acosta, V. Climent, J.M. Feliu,*"Adsorption and first stages of polymerization of aniline on platinum single crystal electrodes"* Synth. Met. 196 (2014) 61-67.

[8]   J.C. Hidalgo-Acosta, V. Climent, M.F. Suárez-Herrera, J.M. Feliu,*"Enhanced electrochemical reversibility of ultrathin aniline oligomer films grown on Pt(111)"* Electrochem. Commun. 13 (2011) 1304-1308.

[9]   A.M. Navarro-Suárez, J.C. Hidalgo-Acosta, L. Fadini, J.M. Feliu, M.F. Suárez-Herrera,*"Electrochemical Oxidation of Hydrogen on Basal Plane Platinum Electrodes in Imidazolium Ionic Liquids"* J. Phys. Chem. C 115 (2011) 11147-11155.

PROFESSIONAL MEETINGS

- M. Jović J.C. Hidalgo-Acosta, A. Lesch, V. Costa-Basetto, E. Smirnov, F. Cortés-Salazar, H.H. Girault, *Flexible pH Sensor Based on Layer-by-Layer Assembled Iridium Oxide Nanoparticles* (Poster).Nano-Tera Annual Plenary Meeting. Lausanne, Switzerland. April, 2016.

- J.C. Hidalgo-Acosta, M.A. Méndez, M.D. Scanlon, H. Vrubel, V. Amstutz, W. Adamiak, M. Opallo and H. H. Girault, *Catalysis of Water Oxidation in Acetonitrile by Iridium Oxide Nanoparticles* (Poster). ISE 65th ANNUAL MEETING of the International Society of Electrochemistry. Lausanne, Switzerland. August, 2014.

- J.C. Hidalgo-Acosta, M.D. Scanlon, V. Amstutz and H.H. Girault, *Towards the Design of a System for Oxygen Evolution at Liquid-Liquid Interfaces* (Poster). ECHEMS Meeting: Electrochemistry in Particles, Droplets, and Bubbles, Spain. February, 2013.

- J.C. Hidalgo-Acosta, M.D. Scanlon, V. Amstutz and H.H. Girault, *Towards the Design of a System for Oxygen Evolution at Liquid-Liquid Interfaces* (Poster). Zing Conferences. Lanzarote, Spain. February, 2013.

- <u>J.C. Hidalgo-Acosta,</u> V. Climent, M.F. Suárez-Herrera, J.M. Feliu, *Adsorption and Firsts Stages of Polymerization of Aniline on Platinum Single Crystal Electrodes* (Poster). ELCAT. Electrocatalysis: Present and Future. November, 2011. Alicante, Spain. November, 2011.

- Workshop on Surface Electrochemistry (Attendant). Organized by: Surface Electrochemistry Group, Institute of Electrochemistry of the University of Alicante. Alicante, Spain. November, 2010.